UNIVERSITÀ DEGLI STUDI DELL'INSUBRIA

Dipartimento di Scienza e Alta Tecnologia

Anno Accademico 2011-2012

Laurea Specialistica in Fisica

THE HIGH RESOLUTION SILICON TELESCOPE OF THE INSULAB GROUP

Laureanda: Silvia Bonfanti
Matricola 704642

Tutor: Dr.ssa Michela Prest
Università degli Studi dell'Insubria
Co-tutor: Dr. Erik Vallazza
INFN - Sezione di Trieste
Co-tutor: Dr.ssa Daniela Lietti
Università degli Studi dell'Insubria

“To see a world in a grain of sand”
William Blake

Contents

Riassunto della tesi

In diversi campi della fisica, che spaziano dalla fisica delle alte energie fino alla fisica delle astroparticelle, la ricostruzione della traiettoria delle particelle è fondamentale per comprendere ed analizzare i processi fisici.
I rivelatori di traccia vengono realizzati utilizzando una serie di rivelatori sensibili alla posizione che sfruttano il segnale elettrico indotto nel rivelatore dalle particelle quando interagiscono con il materiale. Tali rivelatori di posizione sono sottili e assorbono solamente una piccola frazione dell'energia della particella, in modo da perturbare limitatamente la traiettoria e permettere la misura delle coordinate nei suoi diversi punti. Utilizzando le singole coordinate misurate è possibile ricostruire la traccia della particella ed anche, nel contesto dei moderni collisori di particelle, i vertici di produzione e decadimento e quindi la vita media delle particelle stesse, nonché il loro momento se si utilizza un campo magnetico.
Come descritto nel capitolo 1 di questa tesi, la ricerca di una risoluzione spaziale sempre più spinta nella ricostruzione delle tracce ha portato a rivoluzioni nei metodi sperimentali: partendo dalle emulsioni fotografiche e dalle camere a bolle degli anni '40 e '50, si è arrivati negli anni '60 all'invenzione della camera proporzionale a multifili (Premio Nobel a Charpak) e alla rivelazione elettronica delle tracce con un'accuratezza dell'ordine del mm. Si è passati poi nel 1975 all'invenzione della camera a deriva, che ha permesso di raggiungere una risoluzione spaziale di $\sim$50 μm e alla camera a proiezione temporale, che ha portato a una ricostruzione tridimensionale della traccia, sfruttando i tempi di arrivo e le posizioni misurate dai fili.
La richiesta di risolvere i vertici delle nuove particelle della fine degli anni '70, caratterizzate da vite medie di 10^{-13} s, porta alla grande svolta nei rivelatori di posizione: nel 1980 Kemmer introduce la tecnologia planare per la produzione di rivelatori al silicio che permette una segmentazione del sensore in *strip* e quindi un tracciamento e una precisa ricostruzione dei vertici. I rivelatori a strip di silicio sono tra i più utilizzati per il tracciamento negli esperimenti di fisica delle alte energie, grazie:

- alla possibilità di determinare la posizione delle particelle con un'accuratezza dell'ordine dei micron;

- agli spessori limitati e quindi al contenimento della quantità di materiale presente sul percorso della particella;
- a risposte temporali veloci dell'ordine delle decine di ns.

La maggior parte dei rivelatori al silicio è realizzata su un substrato di silicio di tipo-n (con un surplus di elettroni nel reticolo cristallino) ad alta resistività, su cui vengono impiantate delle sottili strisce di tipo p^+ (alto drogaggio di tipo-p: deficit di elettroni), mentre sulla superficie opposta alle strip viene impiantato un elettrodo n^+ (alto drogaggio di tipo n). In tal modo si ottiene un particolare tipo di giunzione che viene completamente svuotata dalle cariche libere del substrato applicando una polarizzazione inversa. La particella che incide sul rivelatore produce coppie elettrone-lacuna che derivano verso gli elettrodi.
In generale, i rivelatori a strip di silicio possono essere realizzati secondo due differenti geometrie: *single side* o *double side*, in modo da ottenere rispettivamente una misura della posizione unidimensionale o bidimensionale. Nei rivelatori double side le strip vengono impiantate su entrambi i lati del substrato, utilizzando una differente orientazione (90°) e permettendo così di ottenere la coordinata (x,y) del punto d'impatto. Il lato su cui vengono impiantate le strip p^+ è detto lato giunzione, mentre quello su cui vengono impiantate le strip n^+ è detto lato ohmico. In questo tipo di rivelatori la risoluzione spaziale, cioè la distanza rms tra la coordinata misurata e la posizione d'impatto vera, dipende sia da processi fisici come la diffusione dei portatori di carica, che da parametri esterni come il passo delle strip e il rapporto segnale rumore. La fisica dei rivelatori a strip e i fattori che ne determinano la risoluzione spaziale sono descritti nel capitolo 2.
Questo lavoro di tesi si è incentrato sullo studio delle performance del sistema di tracciamento (*telescopio*) ad alta risoluzione del gruppo INSULAB e sull'implementazione del nuovo sistema di acquisizione dati (DAQ) nato per ottemperare all'elevato rate dei fasci estratti della North Area al CERN. Il telescopio INSULAB è stato realizzato per testare rivelatori che vanno dai calorimetri fino a sistemi più complessi come nel caso della fisica dei cristalli incurvati di cui l'esperimento COHERENT si occupa e che viene brevemente trattata alla fine del capitolo 2. Tali cristalli sono in grado di deflettere le particelle cariche relativistiche, producendo lo stesso effetto di un grande campo magnetico, grazie all'interazione coerente delle particelle stesse con la struttura cristallina ordinata. L'utilizzo di un telescopio ad alta precisione spaziale, soprattutto nella direzione che misura l'angolo di deflessione, è fondamentale per visualizzare i diversi effetti legati ai cristalli incurvati.
Il telescopio è formato da quattro moduli di rivelatori a microstrip di silicio double side con uno spessore di 300 μm, un'area di 1.92×1.92 cm^2 e 384 strip; il passo di lettura è di 50 μm e quello fisico è di 50 μm dal lato-n e di 25 μm dal lato-p che è così caratterizzato da una strip intermedia (o *floating*) cioè una strip fisicamente

presente ma non connessa all'elettronica di lettura.
I moduli del telescopio, realizzati dall'INFN di Trieste, sono letti da ASIC (Application Specific Integrated Circuit) VA2 della Gamma Medica. Ogni ASIC è formato da 128 canali ciascuno costituito da un pre-amplificatore, uno shaper e un circuito sample&hold che permette di campionare il picco del segnale di uscita dallo shaper. L'uscita analogica è multiplexata: nella fase di lettura, i 128 canali vengono indirizzati uno alla volta sulla linea di uscita per essere digitalizzati.
Il telescopio è stato inizialmente testato con l'utilizzo di una sorgente di ^{90}Sr e l'elettronica di lettura "standard" basata sugli ADC (Analog to Digital Converter) V550 della CAEN. Tali ADC possono operare in zero suppression (per esempio sui fasci estratti del CERN), salvando cioè solamente le informazioni dei canali al di sopra di una certa soglia e consentendo di ottenere un rate di acquisizione massimo di 3 kHz. Il principale svantaggio è rappresentato dal fatto che i dati vengono letti dal sistema VME e scritti sul PC ad ogni evento e ciò non è ideale quando si lavora con i fasci impulsati del CERN dove tipicamente si ha una spill (il pacchetto di particelle) di 8 sec ogni 45 sec.
Il test della nuova elettronica di lettura del telescopio INSULAB si è svolto nel giugno 2012 presso la linea H4 dell'SPS del CERN. Il nuovo sistema si basa sulla memorizzazione degli eventi in apposite schede VRB (VME Readout Board) che rappresentano l'interfaccia tra il rivelatore e il sistema di acquisizione (VME controllato dal PC tramite una scheda SBS Bit3 otticamente connessa). In particolare la scheda VRB è programmabile attraverso un'Altera EP2C50 FPGA con 50k celle e 581 kbit di RAM interna, può operare in zero suppression immagazzinando un massimo di 65536 eventi di 16x2 strip per ogni modulo e possiede 4 Mword di 32 bit di RAM esterna.
L'acquisizione è stata programmata in modo tale da trasferire i dati durante il periodo interspill; la digitalizzazione dei segnali è stata realizzata *in situ* grazie ad ADC realizzati *ad hoc* e posizionati vicino al telescopio. Il rate di acquisizione così ottenuto è di 6 kHz.
Nel capitolo 3 vengono presentati i risultati dei test effettuati a Como e al CERN; l'analisi dati è stata realizzata prestando attenzione alle seguenti figure di merito: rumore e calcolo dei pedestalli, identificazione del *cluster* (ovvero il gruppo di strip in cui la particella ha rilasciato il segnale), utilizzo del metodo del baricentro per trovare la posizione d'impatto della particella sui moduli, individuazione del rapporto segnale rumore e scan sul segnale di *hold* per studiare il corretto campionamento del segnale di output di ciascun lato di ogni modulo.
L'ultimo capitolo si è concentrato sullo studio dettagliato della risoluzione spaziale e sull'influenza della distribuzione della carica prodotta dalla particella tra le strip che compongono il cluster. Tale distribuzione è descritta da una variabile detta η, che permette una interpolazione non lineare tra le due strip adiacenti del cluster che hanno il massimo segnale.

In tal modo è stato possibile eliminare la dipendenza della posizione di arrivo della particella dal punto d'impatto all'interno della strip, ottenendo anche un miglioramento nella risoluzione spaziale, che è stata calcolata essere di $\sim$4 μm per il lato giunzione.
Il telescopio e il suo nuovo sistema di acquisizione ad alta velocità sono stati successivamente installati sulla linea di fascio H8 del CERN a luglio 2012, come parte del setup sperimentale per lo studio dei cristalli incurvati nel contesto dell'esperimento COHERENT; la nuova catena di elettronica ha permesso di testare il doppio dei cristalli nello stesso periodo di tempo.
Gli obiettivi a medio termine della fase successiva di sviluppo del telescopio sono l'introduzione del gigabit link (per la trasmissione su cavo o fibra ottica con un rate fino a 1.25 Gbit/s) e l'utilizzo di ASIC autotriggeranti con lettura parallela dei tre ASIC per aumentare ulteriormente il rate di acquisizione dati. Tali ASIC autotriggeranti (VA1TA) sono già in fase di test con rivelatori a single side come descritto nell'appendice A di questa tesi.

Introduction

In many different physics fields, ranging from high energy physics to astroparticle physics, the reconstruction of the trajectory of the particles is fundamental to understand and analyze the physical processes.

The very first tracking detectors for ionizing particles were photographic plates and soon afterwards nuclear emulsions, both superseded a few years later by bubble chambers and electronic detectors.
By the early 1970s, drift chambers had been developed and were used as electronic tracking devices, both in fixed target and in colliding beam experiments. Their 100 μm precision was considered adequate for charged particle tracking and momentum measurements, as for instance for the K_s^0 and Λ_0 detection.

The discovery of the J/Ψ particle in November 1974 and of the τ lepton in 1975 changed this situation dramatically. Measurements of particles lifetimes of the order of 10^{-13} s demanded tracking devices with a much higher precision, able to resolve secondary and tertiary vertices within large particle densities.
Hints of the decays of short-lived particles in cosmic rays were observed in the emulsions, but the decays could not be fully reconstructed. The identification of these particles and the measurement of their lifetimes required high precision vertex detectors that were embedded in large spectrometers operating at accelerators and capable to measure the momentum and to perform a full particle identification.

The breakthrough in the position sensitive detectors panorama dates 1980 when J. Kemmer introduced the planar technology for the production of silicon detectors. This technology allows a segmentation of the sensor in *strips* and therefore a precise tracking and vertex reconstruction.
In high energy physics, the use of silicon as an active target and high resolution tracking device was pioneered by the NA-11 group at CERN. In colliding beam experiments this technique was used especially to tag the presence of b quarks within particle jets. It was first introduced in the DELPHI experiment at LEP but soon followed by all the collider experiments. The long expected top quark discovery was possible mainly with the help of the CDF silicon vertex tracker, providing the b quark information. The new LHC experiments are built using a

huge amount of silicon strips and pixels for the vertex and tracks reconstruction.

The silicon strip detectors are widely used for the tracking, thanks to:

- the possibility to determine the position of the particles with an accuracy of the order of microns;
- their limited thickness, which allows to keep under control the quantity of material present on the path of the particle;
- a fast response of the order of tens of ns.

In recent years, custom designed integrated circuits have been developed to comply with the high density of the readout channels. A typical ASIC (Application Specific Integrated Circuit) contains 64 or 128 channels, consisting of a low noise charge sensitive amplifier, a discriminator, a sample&hold circuit and a multiplexed digitizer. In some applications, like in this thesis work, only one every nth strip (n=2-6) is connected to the readout electronics and the capacitive charge division between the floating and connected strips is used to improve the position reconstruction.

This thesis has focused on the study of the performance of the high resolution tracking system (*telescope*) of the INSULAB group and on the implementation of a new data acquisition (DAQ) to comply with the high rate of the CERN North Area extracted beams. This system has allowed to increase the DAQ rate by a factor two with respect to the "standard" electronics.
The telescope has been initially tested with a ^{90}Sr source and the standard readout electronics at the Como laboratory; the tests of the new readout electronics have been performed in June 2012 at the CERN SPS H4 line.

The INSULAB telescope is designed to test detectors ranging from calorimeters to more complex systems like in the case of the bent crystals studied by the COHERENT experiment. These crystals are able to deflect the relativistic charged particles, producing the same effect of a huge magnetic field, thanks to the coherent interaction of the particles with the ordered crystalline structure. A telescope with a high spatial resolution, especially in the direction that measures the deflection, is a must to detect the different effects of the bent crystals. In 2006 the INSULAB microstrip silicon telescope has allowed the H8RD22 collaboration to obtain the first very high precision measurement of the channelling and volume reflection effects.

The telescope consists of four 300 μm thick double side silicon strip detector modules with an area of 1.92×1.92 cm^2 and 384 strips. The readout pitch is 50 μm on both sides of the module but the junction side has an implant pitch of 25 μm (and thus a floating strip) to improve the resolution. The telescope modules have been designed and assembled by INFN Trieste and are readout by the VA2 ASICs (Gamma Medica).

From the point of view of the thesis organization, a brief historical and theoretical introduction to the main aspects of the tracking detectors is presented in chapter 1: the first part is dedicated to the fundamental quantities that can be obtained from the precise measurement of a track, like the production and decay vertex, the momentum resolution, the impact parameter resolution and the decay length; the second part presents the main particle tracking detecting techniques and their operating principles.
Chapter 2 contains a brief review of the basic properties of semiconductor materials and of the working principles of silicon position sensitive devices. Among the huge variety of silicon sensors, silicon microstrip detectors are treated in detail since they represent the main item of this thesis. The last part of chapter 2 describes the improvements that the use of the INSULAB silicon telescope has allowed in the field of bent crystal physics.
Chapter 3 and chapter 4 are the heart of this thesis work. The telescope and its components are presented in detail together with the commissioning phase at the Como laboratory with the standard electronics. The second part of chapter 3 describes the telescope setup on the H4 beamline at the CERN SPS for the commissioning of the new readout system. The results are analyzed in terms of the overall noise, the identification of the *cluster* (the group of strips in which the particle has released its energy) and the signal to noise ratio.
Chapter 4 deals with a detailed study of the spatial resolution and the distribution of the charge produced by the particle among the strips, which can be reconstructed with the η variable to perform a non-linear interpolation between the two adjacent strips which have collected the maximum signal of the cluster.

The telescope and its new fast readout system have been installed on the H8 beamline as a part of the experimental setup for the study of the bent crystals in the COHERENT experiment. The telescope will now be equipped with a gigabit link to improve the connections between the readout and frontend blocks. New modules are being assembled with self-triggering ASICs. The first tests of this new version are described in the appendix.

Chapter 1

The role of tracking in particle physics measurements

Nuclear physics, elementary particle physics and astro-particle physics experiments investigate the properties of subatomic particles and the way in which they interact; the final goal is to find a complete description of the elementary constituents of matter and of the forces acting between them.

In this context, detectors are needed to identify particles produced in high energy collisions and to measure the various particle parameters such as the momentum and the energy. Detectors are assembled in a variety of types and sizes, but today most are huge and multi-layered.

Despite their differences, they all rely on the same basic principles. They do not make the tracks of particles directly visible. Instead, they produce tiny electrical signals that can be recorded and computed. Much as an animal leaves tracks in the snow, or a jet plane forms trails of condensation across the sky, electrically charged particles leave trails as they gradually lose energy. The art of particle detection is to measure this deposited energy so that it can be recorded [1].

In most experiments it is necessary to measure coordinates along the trajectory of charged particles. If a magnetic field is employed, the curvature of a trajectory determines the sign of the charge and the momentum of the particle. To identify the particle through the measurement of its mass, a simultaneous measurement of momentum and velocity, or of momentum and energy, is necessary; figure 1.1 illustrates the use of the relativistic rise in collision loss for this purpose. A complete kinematic reconstruction of an "event" requires the determination of the energy-momentum four-vectors of the produced neutral particles as well as of charged particles. When the multiplicity of secondary particles is large, the detector must be capable of separating nearby particles in space and if the interaction rate is high, it needs also a good time resolution. This is the reason why a typical apparatus in high energy physics experiments involves many types of detectors,

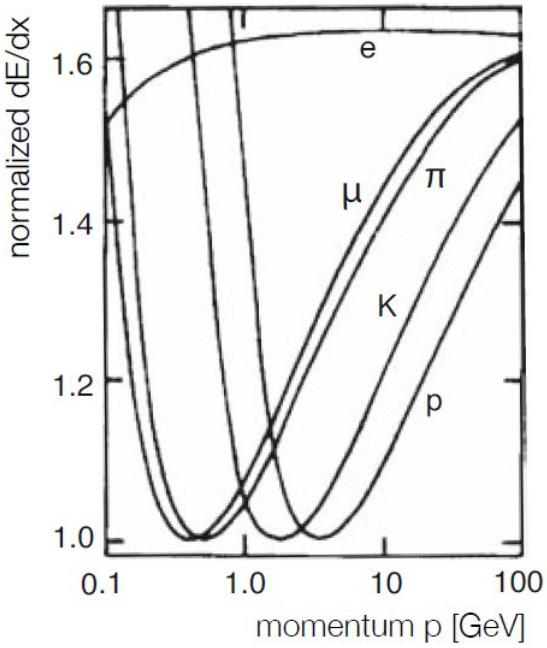

Figure 1.1: Normalized rate of energy loss as a function of momentum in a mixture of argon and methane for electrons, muons, pions, kaons and protons [2].

each performing one or more of the tasks described above [2].

This chapter deals with the description of tracking detectors for charged particles. Neutral particles undergo interaction with the detector material and the position of interaction can be measured. However the interaction of photons usually leads to the absorbption of the photon itself and hence a tracking cannot be performed. Other neutral particles, such as neutrons or neutrinos, produce in the interaction with matter charged particles and a tracking of these particles is again performed by charged particle detectors. To measure the position of charged particles several technologies have been developed, from the simple photographic emulsions of the 1930s to the bubble chambers of the 1960s, to arrive to the gaseous detectors (section 1.2.2) and to the semiconductor ones (section 1.2.3), used in modern colliding beam experiments allowing a precise tracking and even vertexing.

1.1 Why tracking

In many experiments the reconstruction and precise determination of the particles trajectory is essential to understand and analyze the physics processes. The origin of the particle, the direction of the flight and even more sophisticated parameters

such as the particle momentum or the sign of the particle charge can be deduced from the trajectory, if the detector is placed inside a magnetic field. Such tracking detectors are usually built using position sensitive detector elements exploiting the signals particles induce in the detectors when interacting with the detector material. In tracking detectors, the individual elements are thin and absorb only a fraction of the particle energy in order to allow several position measurements on the same particle. The individual measurements are then used to reconstruct the particle trajectory. Thus, tracking provides precise measurements of particle production and decay positions, particle momenta and trajectories.

In the following, the fundamental quantities obtained from a precise measurement of a track like the vertices of production and decay, the momentum resolution, the impact parameter resolution and the decay length, are described.

1.1.1 Momentum measurement

One of the primary observables in high energy particle collisions is the transverse momentum of the outgoing particles, p_T, the component of the momentum[1] orthogonal to the beam direction. The most common way to determine this quantity is to deflect the particle trajectory with a magnetic field and to measure the bending sagitta of the trajectory itself with position sensitive detectors. Such a device is called a magnetic particle spectrometer [3].

Charged particles follow a curved trajectory in a magnetic field $\overrightarrow{B}$, satisfying the equation of motion given by the Lorentz force. Neglecting bremsstrahlung and material effects, the force $\overrightarrow{F}$ is derived from Maxwell's equations to be:

$$\overrightarrow{F} \sim q\overrightarrow{v} \times \overrightarrow{B} \tag{1.1}$$

where $\overrightarrow{v}$ is the particle speed, q is the (signed) charge and $\overrightarrow{B}$ the field strength. If the field is uniform and the presence of matter in the particle path is not considered, the particle will follow a helical trajectory. The real trajectory will differ from an exact helix[2] because of spatial inhomogeneities in the magnetic field and radiation energy losses. If matter is present, there will be additional changes in the trajectory due to ionisation energy loss and multiple scattering, as described in the next section.

The homogeneous solenoid magnetic field B bends the particle track. The track radius R in the plane perpendicular to the magnetic field is proportional to

[1] The transverse momentum is defined as p_T=$p$sinθ where θ is the scattering angle in the center of mass system.

[2] A helix is a 5D object, defined by two positions, two angles and a curvature. A track can be represented as a point in a 5D linear space. Moreover, taking into account the uncertainties on the parameters, a track is fully described by 5 parameters and a 5$\times$5 symmetric error matrix [4].

the transversal momentum p_T and the charge q of the particle:

$$p_T = qBR \tag{1.2}$$

In the following, it is assumed that the particle charge is equal to the charge of an electron, the momentum is evaluated in GeV/c, the magnetic field in teslas and the distance in metres. Under these assumptions equation 1.2 becomes

$$p_T = 0.3BR \tag{1.3}$$

As shown in figure 1.2, the relation between the track radius R and the sagitta s, that is the deviation of the trajectory from a straight line, is

$$s = R\left(1 - \cos\frac{\alpha}{2}\right) \approx R\frac{\alpha^2}{8} \tag{1.4}$$

Using $L/2R$=sin(α/2), where L is the lever arm, and the small angle approximation, one obtains:

$$s = \frac{0.3L^2B}{8p_T} \tag{1.5}$$

Equation 1.5 implies that:

$$\left.\frac{\sigma_{p_T}}{p_T}\right|^{SR} = \frac{\sigma_s}{s} \tag{1.6}$$

where the relative resolution on the sagitta depends only on the precision of the individual points measurement [3].

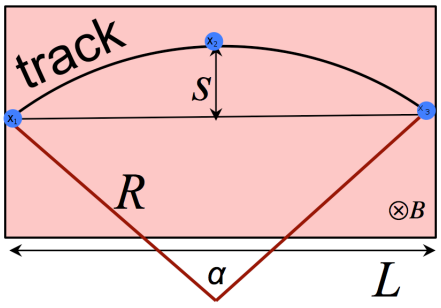

Figure 1.2: Momentum measurement using the sagitta method.

Three equidistant points on the track determine the sagitta as:

$$s = x_2 - \frac{x_1 + x_3}{2} \tag{1.7}$$

[3] SR indicates the sagitta resolution.

where x_i is the coordinate of each point in the direction perpendicular to the magnetic field and the momentum direction. If the spatial resolution σ_x of all these points is the same, the transversal momentum resolution becomes:

$$\left.\frac{\sigma_{p_T}}{p_T}\right|^{SR} = \frac{8p_T\sqrt{3/2}\sigma_x}{0.3L^2B} = 32.6\,\frac{p_T\sigma_x}{L^2B} \tag{1.8}$$

Hence the resolution depends only on the magnetic field B, the lever arm L and σ_x and not on the radius R. Using the typical numbers for a particle experiment [5] (B=1.5 T, L=0.8 m, σ_x=150 μm) one obtains:

$$\left.\frac{\sigma_{p_T}}{p_T}\right|^{SR} = 5.1\cdot 10^{-3}p_T \tag{1.9}$$

Thus for a particle with a transverse momentum p_T=1 GeV/c, σ_{p_T} $\approx$0.5%. Equation 1.8 can be generalized for the case of n position measurements, each with a different σ_x, as shown in [6]. In the case of n >10 equidistant measurements with the same spatial resolution, the momentum resolution is:

$$\left.\frac{\sigma_{p_T}}{p_T}\right|^{SR} = \frac{\sigma_s}{s} = \sqrt{\frac{720}{n+4}}\,\frac{\sigma_x p_T}{(0.3BL^2)} \tag{1.10}$$

Equation 1.10 shows that the intrinsic position resolution has to be good to resolve s and that the B field contributes linearly to it, while a larger lever arm improves the momentum resolution quadratically. The momentum resolution gets worse increasing p_T because tracks curve less.

This trend is opposite to the one of calorimeters in which the resolution improves increasing the energy, as shown in figure 1.3 where the energy resolution for electrons is plotted for the CMS (Compact Muon Solenoid) tracker and calorimeter and for their combined use.

Complications in measuring the momentum

The momentum resolution of equation 1.10 is defined for a massless detector.

In fact the free particle trajectory is perturbed by the presence of the detector material, causing mainly multiple Coulomb scattering (MCS). This adds an additional error to the p_T measurement:

$$\left.\frac{\sigma_{p_T}}{p_T}\right|^{MCS} = \frac{28\ \mathrm{MeV/c}}{0.3\ B\ L}\sqrt{\frac{L}{X_0}}\,\frac{p_T}{\beta p} \tag{1.11}$$

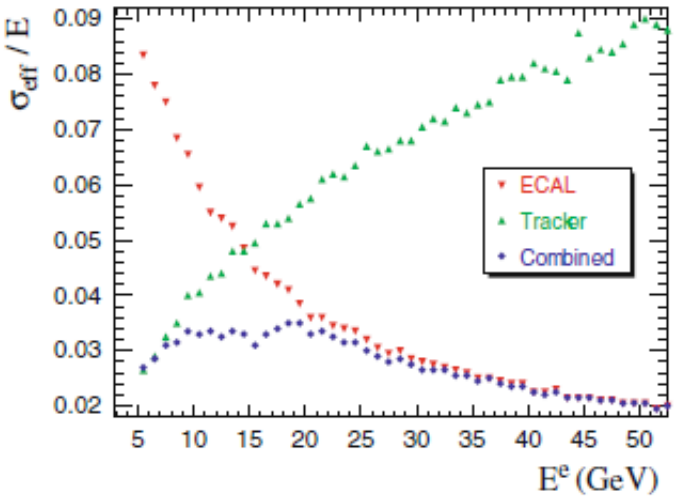

Figure 1.3: Energy resolution with the CMS tracker, the electromagnetic calorimeter (ECAL) and their combined value [7].

The resolution due to multiple scattering gets worse increasing Z (and thus reducing the radiation length[4] X_0) and improves increasing B and L. For a given detector $\left.\frac{\sigma_{p_T}}{p_T}\right|^{MCS}$ is basically constant as a function of p_T so its importance is larger at low momentum.
The material is the cause of several other effects:

- energy loss from ionisation that reduces the track radius and bremsstrahlung for electrons that adds noise to the electromagnetic calorimeters;
- nuclear interactions that reduce the tracking efficiency.

The importance of all these effects decreases with p_T.

1.1.2 Production and decay position

One of the main goals of a tracking system is the primary vertex location which is fundamental for many physics studies such as b-tagging and lifetime measurements of heavy quarks and leptons [9]. The primary vertex is the position where

[4]The radiation length X_0 is both the mean distance over which a high energy electron loses all but 1/e of its energy via bremsstrahlung, and 7/9 of the mean free path for pair production by a high energy photon [8].

It is also the appropriate scale length for describing high energy electromagnetic cascades. It is given by the approximated formula: $X_0 = \frac{716.4\ A}{Z(Z+1)\ln(287/\sqrt{Z})}$ in g/cm^{-2}, where A and Z are the average atomic mass and proton number.

two particles in the colliding beams interact. Nowadays, with solid state detectors, the position of this vertex can be determined to better than 10 μm in all the three coordinates depending on the tracks momenta and multiciplity [10].

Secondary vertices also need to be tagged mainly to identify heavy flavor quarks, like the bottom and charm, and the τ lepton to measure lifetimes for instance and to reduce background. Given these particle lifetimes are in the picosecond range, the track reconstruction must be precise enough to extrapolate into the interaction region, resolving primary, secondary and tertiary vertices.

An example of track and vertex reconstruction can be seen in figure 1.4, where the decay of a strange beauty particle (B_s) in the LHCb (Large Hadron Collider beauty) experiment is displayed[5]. The primary, secondary and tertiary vertices are also shown.

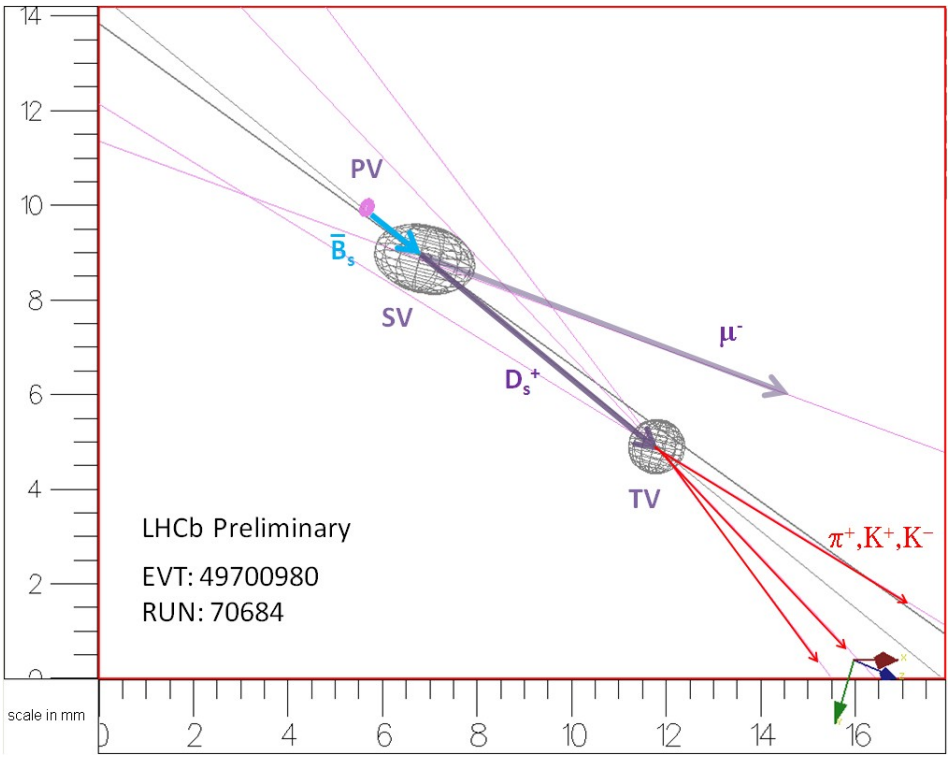

Figure 1.4: A close up of an event in LHCb with all the characteristics of the decay of a strange beauty particle (B_s), which contains a beauty quark and a strange quark. PV, SV and TV are respectively the primary, the secondary and the tertiary vertex.

The parameter used to characterize the secondary vertex reconstruction capability is the impact parameter resolution σ_{d_0}. The impact parameter d_0 is defined

[5]/http://www.cern.ch/rd50S.

as the shortest distance between a reconstructed track and the primary vertex. It is a crucial quality parameter of the full detector performance. If the measured impact parameter is significantly larger[6] than the experimental resolution, a secondary decay vertex is probably present. The d_0 value depends on the detector geometry and strongly on multiple scattering, hence the material budget on the path. For a simple two layer system, σ_{d_0} can be expressed as [11]:

$$\sigma^2{}_{d_0} = \sigma^2{}_{MCS} + \sigma^2{}_{geom} \tag{1.12}$$

with

$$\sigma^2{}_{geom} = \left(\frac{\sigma_1 r_2}{r_2 - r_1}\right)^2 + \left(\frac{\sigma_2 r_1}{r_2 - r_1}\right)^2 \text{ and } \sigma^2{}_{MCS} = \sum_{j=1}^{n_{scatt}} (R_j \Delta\Theta_j)^2 \tag{1.13}$$

with r_1 and r_2 the distances from the production point, σ_1 and σ_2 the intrinsic resolutions of the two layers and

$$\Delta\Theta_j \simeq (0.0136/p_T)\sqrt{\Delta X/X_0}[1 + 0.038\ln(\Delta X/X_0)] \tag{1.14}$$

the average multiple scattering angle of a particle with a momentum p_T crossing a thickness ΔX (expressed in terms of the radiation length X_0) located at a radius R_j; n_{scatt} is the number of layers in front of the last detection element. The impact parameter resolution is often parametrized as σ_{d_0}=σ^2_{asympt}+$(\sigma_{MCS}/p_T)^2$ with p_T in GeV/c. Typical numbers for a particle experiment are σ(r-ϕ)=18 μm for the r-ϕ plane and σ(z)=20 μm for the r-z one [12].

All the considerations made above translate in the following design requirements:

- to minimize the mass of the beam pipe and vertex detector, including cables and support structures to reduce the Coulomb scattering. This is especially true in front of the very first measurement layer: keeping $\frac{\Delta X_j}{X_0}$ and Θ_j small results in a small σ_{MCS};
- to minimize the extrapolation error, maximizing the impact parameter resolution by placing the first detection layer as close as possible to the primary interaction point that is r_1 has to be small;
- to maximize the radius for the outer measurement layer (r_2 large);
- to have a good intrinsic detector resolution;

[6]The track does not pass through the primary vertex.

- to take alignment into account from the very beginning, overlapping sensors to allow the extrapolation of the exact position with tracks crossing the overlapped modules;
- to produce performing algorithms for the alignment, the pattern recognition and the vertex identification.

Tracks with large impact parameters can be used to tag the decays of short-lived particles, such as B or D hadrons or τ leptons [13]. These particles bear essential information for many interesting physics topics, e.g. the presence of b quarks is a signature for the Higgs boson decay and top quark decay, and events with b quarks are relevant to the understanding of the CP violation phenomenon [14]. The ability to efficiently single out b quark events will considerably help in solving these fundamental particle physics problems. The impact parameter resolution typically varies from 10 μm to 100 μm for 100 GeV/c and 1 GeV/c track transverse momenta.

1.1.3 Direct lifetime measurements

The standard method to determine directly the particle decay time t is to measure the particle momentum p and the decay length L, and this requires an accurate determination of the production and decay vertices. The proper flight time can be obtained as [15]:

$$t \;=\; \frac{L}{\beta\,\gamma\,c} \;=\; L\cdot\frac{m}{p} \tag{1.15}$$

where m is the mass of the decaying particle, β=v/c (v is the particle speed and c the speed of light) and γ = $1/\sqrt{1-\beta^2}$. If the decay products are not fully detected, the momentum is often estimated from an unconstrained kinematic fit or from the measured effective mass and momentum sum of the measured decay tracks.

A more model independent estimate is based on the measurement of the decay length in the plane transverse to the beam

$$t \;=\; L_T\cdot\frac{m}{p_T} \tag{1.16}$$

where p_T and L_T are the tranverse momentum and transverse decay length, respectively. The problem is that the transverse momentum components are generally much smaller than the longitudinal components, and thus for short lifetimes, the error on the length L_T may become significant. The measurement of the transverse decay length in a colliding beam experiment is illustrated in figure 1.5. The beam-beam interaction region has an elliptical shape, its size varies from machine to machine with a typical dimension of 300 μm$\times$40 μm. The production point

can be estimated from the knowledge of the beam position and size averaged over many events or from the tracks of the individual event. In most cases the beam spot is larger than the position error of the individual tracks. The decay point is determined using the secondary tracks [16].

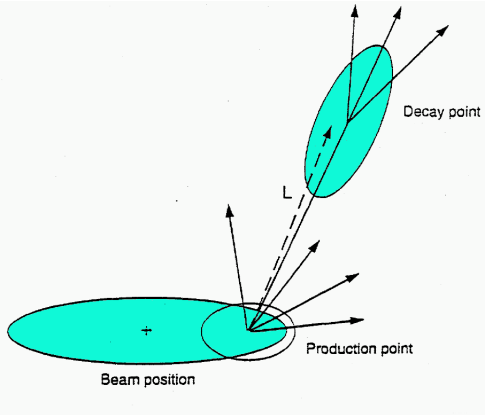

Figure 1.5: The decay length definition for a particle produced in a colliding beam experiment.

1.2 Detector techniques

Since the very beginning of particle physics, when Thomson realized that the cathode rays he was studying were not "rays" but streams of subatomic charged particles, the physicists' understanding of the subatomic physics and the mechanisms that govern it has depended strongly on their ability to detect the tracks of charged particles. Thomson was able to suppose the existence of electrons, measure their charge to mass ratio and their velocity as they were emitted by a hot filament because he could see their trajectory as they passed through crossed electric and magnetic fields [17]. After Thomson's experiments in 1897, many techniques have been developed to detect charged particle tracks: nuclear emulsions, cloud chambers, bubble chambers, spark chambers, streamer chambers, various gas and solid-state detectors. All these techniques rely on high energy charged particles ionizing atoms as they cross matter. The ions left along the paths of the high energy particles leave an observable trace such as a bubble, a spark, condensation or a charge avalanche. Figure 1.6 presents the first positron detected by Anderson in 1932 with a cloud chamber.

Many of these particle detecting techniques have been abandoned because of their inherent limitations, in favor of gas or solid state detectors. Experiments at the newest colliders like the RHIC (Relativistic Heavy Ion Collider) or the LHC

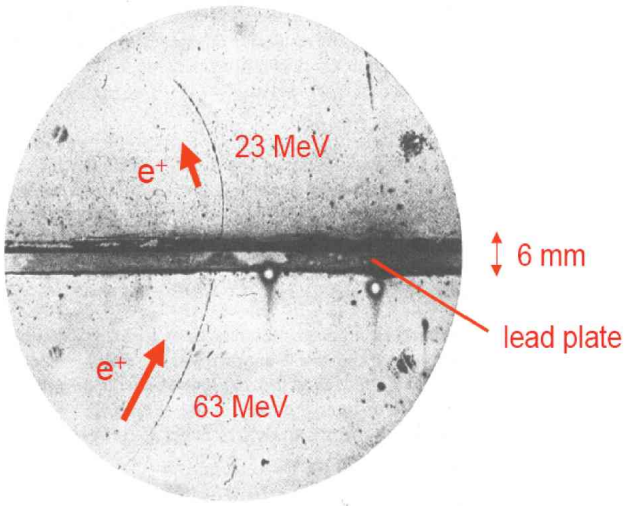

Figure 1.6: A Wilson cloud chamber photograph showing the passage of a positron. The length of the track for a relatively low energy particle allows to distinguish between a positron and a proton [18].

(Large Hadron Collider) rely almost exclusively on these two techniques suitable for triggering, high-event rates and the digitization of huge amounts of data [19]. Bubble chambers however are of particular historic importance and produced a wealth of information from their birth in 1952 to well into the 1970s. Their importance for high energy physics was acknowledged with two Nobel prizes: the first in 1960 was awarded to Donald Glaser and the second, in 1968, was won by Luis Alvarez that improved the design of the previously invented bubble chamber to allow the detection of extremely short-lived particles, the resonance particles. Alvarez also improved the computational techniques used to analyze large amounts of bubble chamber data.

1.2.1 Bubble chambers: three decades of physics

Bubble chambers are sensitive to ionizing tracks thanks to the rapid expansion of a super-heated liquid volume; the trajectories of ionizing particles appear as trails of bubbles. The bubbles were recorded in two or more projections on a photographic film. The advantages bubble chambers offered kept them in a widespread use for three decades, from the 1950s to well into the 1970s. They had a good spatial resolution (10-150 μm), a large sensitive volume, 4π geometrical acceptance, and allowed for the use of a variety of materials as targets.

One of the most important physics discovery performed with this type of detector is the weak neutral current; the Gargamelle bubble chamber (figure 1.7),

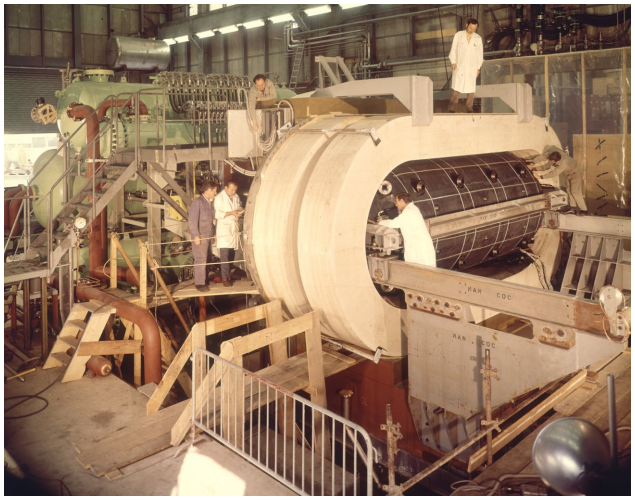

Figure 1.7: Gargamelle at CERN; with a diameter of nearly 2 m and 4.8 m in length, it contained nearly 12 m^3 of freon.

operating from 1970 to 1978 at CERN (European Organization for Nuclear Research) with a ν_μ beam produced by the CERN PS (Proton Synchrotron), recorded the first experimental evidence of this phenomenon shown in figure 1.8(a). At that time in fact Glashow, Weinberg and Salam found that their unified electroweak theory required three carrier particles for the weak force: two charged particles (positive and negative) and a neutral one [20]. This latter, the Z^0, was completely new, and evidence of its existence[7] would have been crucial in confirming the correctness of the electroweak hypothesis. Gargamelle had to detect the following interactions to verify the weak neutral current theory:

$$\nu_\mu + e^- \rightarrow \nu_\mu + e^- \text{ and } \bar{\nu}_\mu + e^- \rightarrow \bar{\nu}_\mu + e^- \tag{1.17}$$

The requirement for the final state to contain an electron (figure 1.8(b)), when the initial state contains a muon neutrino or antineutrino, guarantees the process being caused by a neutral current [21].

It became obvious in the late 1970s that, despite their powerful imaging capability, bubble chambers were inadequate to allow the identification of energetic particles, because they could not operate at rates above a few tens of Hertz. This was the limitation of the spark chambers too [22], devices invented in the 1960s that allowed selective recording of events, but with an inferior quality with respect to bubble chambers. This fact, combined with the poor impact parameter resolution, limited the possibility to recognize very short-lived particles and to contribute to the rising heavy flavor physics. Thus the experiments began to require

[7]The first observation of a Z particle was performed by the UA1 experiment at CERN in 1983.

more complex triggers and new large volume high precision detectors demanded electronic data to come in use.

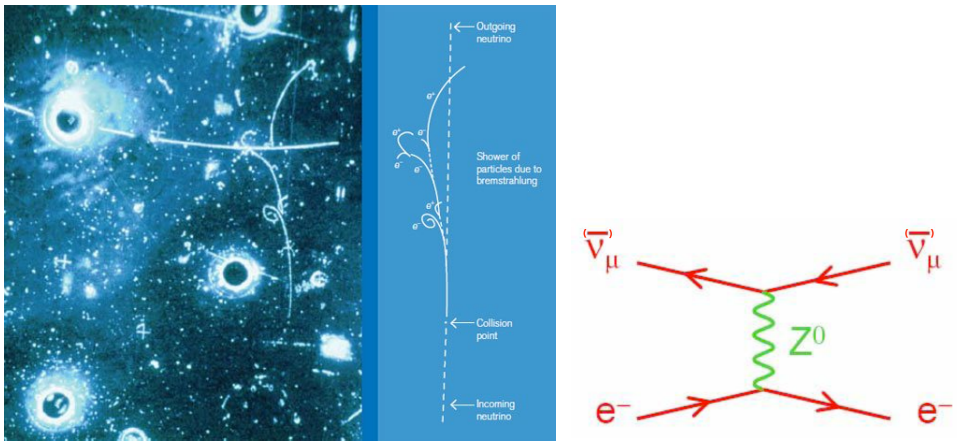

(a) (b)

Figure 1.8: a) First observation of a neutral current event, due to a Z particle, performed with the Gargamelle bubble chamber at CERN. The beam of ν_μ entered from the bottom of the image. b) Feynman diagram for the $\overset{(-)}{\nu}_\mu + e^- \rightarrow \overset{(-)}{\nu}_\mu + e^-$ interaction.

1.2.2 Today tracking gaseous detectors

In the 1970s one of the protagonists who contributed significantly to the improvement of detection techniques in particle physics was Georges Charpak. His work led to particle detectors that combine speed with precision. In 1968, Charpak's group found new ways to exploit ionization for particle detection.

The team developed two types of tracking detectors, the MWPC (Multi-Wire Proportional Chamber) [23] and the drift chamber [24]. They both could work much faster and more precisely than bubble chambers, and so deal more effectively with the huge numbers of interactions in modern particle accelerators.

1.2.2.1 The proportional wire chamber revolution

A multiwire proportional chamber consists of planes of independent anode wires, with a pitch of 1-2 mm, located between two planes of cathodes held at a distance of 4-5 times the wire spacing (figure 1.9(a)). A negative voltage is applied to the cathodes and the anode wires are held at ground. Each wire then acts as a proportional counter for the primary ionization. When the charged particle crosses

the MWPC, a wire gives the signal and the track can be reconstructed. The wire diameter should be of the order of 20-50 μm. The spatial resolution is given by $d/\sqrt{12}$ = 300 μm for d = 1 mm, where d is the wire pitch. Charpak was awarded the 1992 Nobel prize in physics. The first large size MWPCs were successfully used in the early 1970s by Jack Steinberger and collaborators in an experiment on CP violation [25]. With a modified design, a set of 20 large size MWPCs constituted the core of the SFM (Split Field Magnet) detector, shown in figure 1.9(b), installed at one of the intersects of the CERN proton-proton ISR (Intersecting Storage Ring). Tracks emerging from the beam crossing region were deflected by the magnetic field and recorded in a succession of wire planes; the curvature provided the momentum. The detector started its operation in 1972 and took data at an unprecedented rate of several kHz until the ISR decommissioning in 1983.

A multiwire chamber out-performs a bubble chamber in terms of the rate at which it can detect particles, but the tracking of particles across a large volume (for instance a cubic metre) requires a large number of wires each coupled to the electronics to amplify the signal.

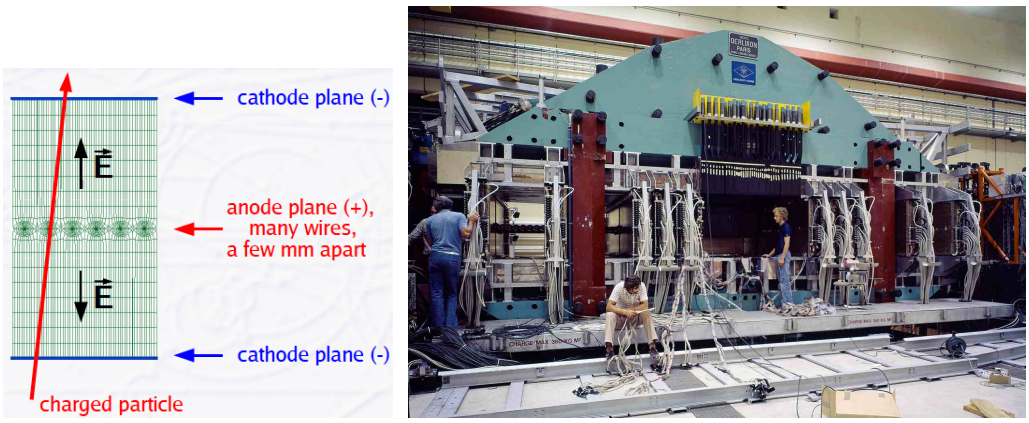

(a) (b)

Figure 1.9: a) Schematics of a MWPC; thin anode wires between two cathodes act as independent proportional counters. b) The SFM spectrometer featured the first large-scale application of MWPCs (about 70000 wires).

1.2.2.2 The drift chamber

The drift chamber is able to perform a precise measurement with fewer wires. In fact it allows to measure time, which can be done very precisely with modern electronics, to compute a distance [26]. The chamber consists of parallel wires strung across a volume of gas; some of the wires provide electric fields that divide a large volume into smaller units or "cells". Each cell acts like an individual

detector, in which the electric field directs the ionization electrons from a charged particle track towards a central "sense" wire. If the electrons travel at a constant velocity, then the time it takes for them to reach this wire gives a good measurement of the distance of the track from the sense wire. This technique allowed to locate particle tracks with an accuracy of around 50 μm.

Electrons released in a gas will slow down as they lose energy in collisions with the gas molecules. On the other hand a region of high electric field will accelerate them so that they gain energy. The drift chamber works by balancing the two effects in a carefully designed electric field, so that the energy ionization electrons gain from the field matches the energy they lose in collisions. The overall result is that the electrons travel at a constant known speed. The high energy charged particles being detected travel through the chamber much faster than the electrons drift to the sense wires, so scintillation counters may be used to start the measuring gate, as shown in figure 1.10(a). When the drifting electrons reach a sense wire, the signal from the wire stops the counter, and the time can be computed. This time combined with the speed of the drifting electrons results in the distance from the sense wire, and hence a point on the ionizing particle track. Figure 1.10(b) shows the WA1 experiment, installed at the CERN neutrino beam in 1978. The setup had alternate layers of magnetized iron, scintillation counters and hexagonal 4 m drift chambers [27]. A great advantage of the drift chamber is that the sense wires can be spaced at intervals of several centimetres or more, because it is the drift time that provides the information on the position. This reduces the number of wires and ancillary electronics. The next step to reduce the number of wires even further is the time projection chamber.

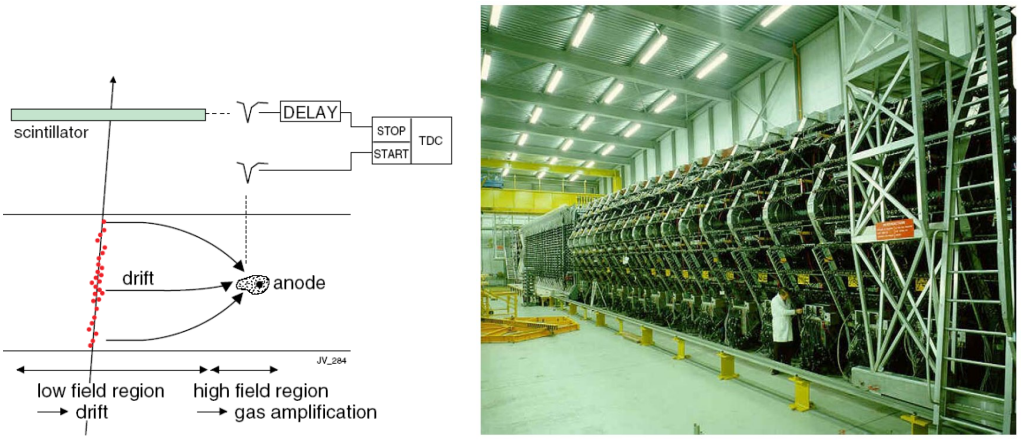

(a) (b)

Figure 1.10: a) The drift chamber working principle. b) The WA1 neutrino experiment, using large area drift chambers.

1.2.2.3 The Time Projection Chamber

The TPC (Time Projection Chamber), invented by David Nygren from the Lawrence Berkeley Laboratory [28], makes a complete detector out of a single large drift cell. Nygren's idea was to have a 2 m diameter and 2 m long cylinder filled with gas with a single electrode at a high negative voltage across the middle. Electrons released along the tracks of ionizing particles drift towards the ends of the cylinder, which are positive relative to the centre. The time of arrival of the electrons at the end plates gives a measurement of how far along the cylinder the electrons originated. Moreover, as the electrons arrive at an end plate they create an image of a two-dimensional slice through the tracks. The measurements of the positions together with the arrival times provide enough information for a computer to reconstruct a three-dimensional image of the tracks. The number of electrons arriving at an end plate depends on how much ionization has occurred along a track, and this in turn depends on the nature of the ionizing particle that produced the track. Unlike other historic three dimensional detectors, such as the bubble or streamer chambers, the TPC is readout completely electronically; a typical value for the spatial resolution is $\sim$500 μm. Nygren's device, built for an experiment on the PEP (Positron Electron Project) collider at SLAC (Stanford Linear Accelerator Center), in California, started operating in 1983. It was a key part of a huge detector that surrounded the PEP colliding beams [29]. Time projection chambers have since been used in a number of experiments at different laboratories: at CERN, for example, where both the ALEPH (Apparatus for LEP PHysics) and the DELPHI (DEtector with Lepton, Photon and Hadron Identification) experiments at LEP (Large Electron Positron) incorporated large segmented TPCs to track charged particles, at STAR at RHIC at BNL (Brookhaven National Laboratory) where the TPC was studying thousands of tracks produced in high energy collisions between nuclei of gold [30].
The world largest time projection chamber (figure 1.11(a)) is the one of the ALICE (A Large Ion Collider Experiment) experiment [31] at LHC with its nearly 100 cubic metres. Thousands of wires are connected to readout the data produced as particles are created in lead-lead collisions at the centre of the detector. Figure 1.11(b) presents one of the first events[8] from Pb-Pb collisions at a centre-of-mass energy of 2.76 TeV per nucleon pair showing tracks from the ALICE TPC.

[8] https://wiki.kip.uni-heidelberg.de/ti/HLT/index.php

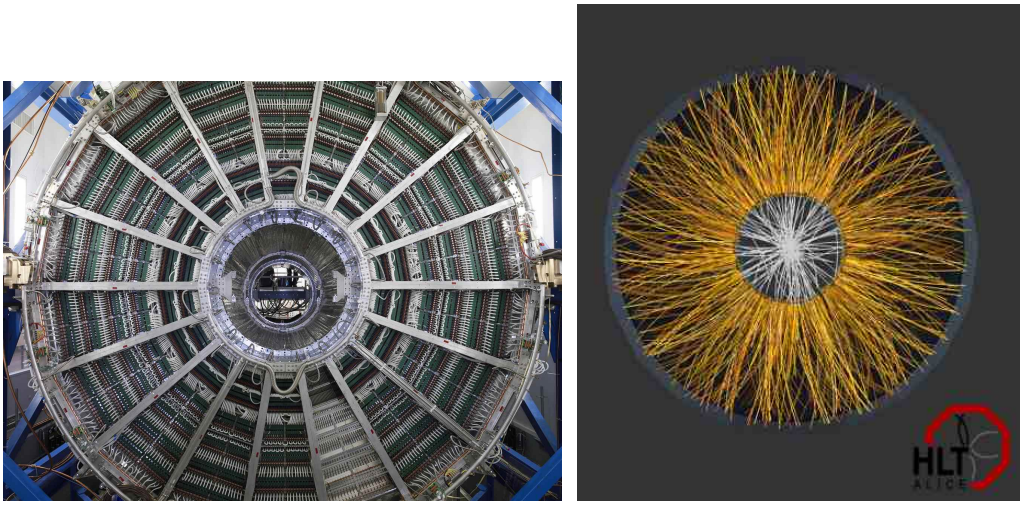

(a) (b)

Figure 1.11: a) The ALICE world largest time projection chamber. b) Event display of one of the first captured heavy ion collisions at ALICE reconstructed by the high level trigger (HLT) [31].

1.2.3 The dawn of solid state tracking detectors: vertex reconstruction

The new particles detected in the 1970s lived much longer than the resonances observed in the preceding decade, but not as long as the strange particles, which could be distinguished through measurable tracks (or gaps in the case of neutral particles) in bubble chambers. When short lifetime particles are produced in collisions between a particle beam and a fixed target, they do not have time to travel very far. A particle with a lifetime of 10^{-13} s travels no more than 300 μm from the production point in the forward direction. This makes the recognition of the decay vertex very complex. In colliding beam experiments [32], the question is still more severe: such short-lived particles do not even have time to exit from the beam pipe. The solution in both cases is to guarantee that the part of the detector closest to the collision point has as high a resolution as possible. Such a pattern recognition would have been impossible with the relatively poor extrapolation resolution provided by the "standard" tracking detectors like drift chambers or TPCs.

In 1980, Kemmer introduced the planar technique for the production of silicon detectors which allowed a strip-like segmentation of the sensor and hence precise tracking and even vertexing [33]. Nowadays, solid state detectors like silicon microstrip detectors, silicon pixel detectors and silicon drift detectors offer

very good spatial resolutions of the order of 10-100 μm; at present almost every experiment has a silicon "vertex" detector, which can measure the position and angles of charged particle tracks with enough precision to be able to separate tracks originating from decay vertices from those produced at the interaction vertex.

Figure 1.12, which shows the amount of silicon as a function of the experiment (and thus of time), is a clear indication of the importance they have in high energy physics, but also in many other fields like astrophysics or medicine. With

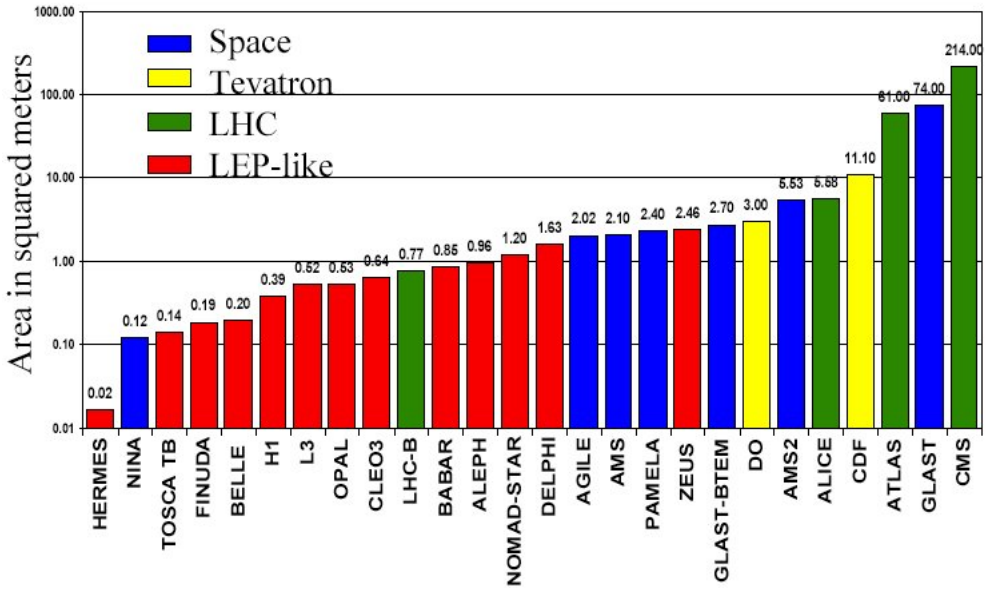

Figure 1.12: Silicon amount in several experiments. Space experiments are presented in blue, the Tevatron experiments in yellow, the LHC ones in green and the LEP-like ones in red [4].

the miniaturization of the electronics, the requirement of having a compact, not too much material budget increasing system was satisfied, and large-scale systems were used in the heart of all detectors, starting from LEP, allowing vertexing in barrel-like detectors. These silicon sensors are particularly important for the tagging of short-lived particles. At the Tevatron at Fermilab, the ability to detect bottom particles in this way was critical in the discovery of the long-sought top quark, which almost exclusively decays to a W boson and a bottom quark as depicted in figure 1.13.

At the time of LEP, silicon detectors performed the vertexing and further out gaseous detectors (e.g. drift chambers or time-projection chambers) with larger lever arms performed the tracking. At LHC, silicon pixel detectors are responsible for the vertexing, and large volume silicon strip detectors (up to 14 layers) are the

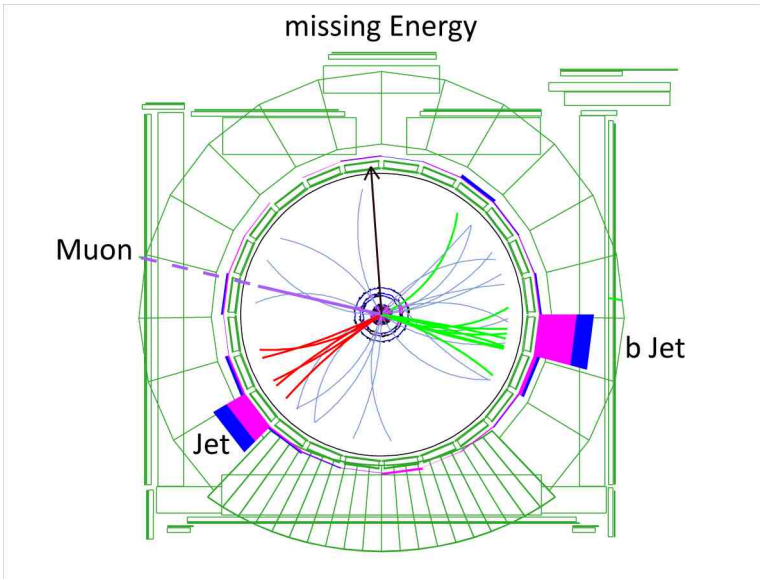

Figure 1.13: A collision event display of the CDF collaboration, showing a single top quark candidate event [5].

main tracking devices. In the following sections the DELPHI tracking system, with the advantages introduced by its microvertex detector, is presented as it was the largest silicon detector of the 1990s, and the CMS tracker is described, as it exploits the largest amount of silicon, corresponding to 214 m^2 and 76 million channels.

1.2.3.1 The DELPHI vertex detector at LEP: testing the Standard Model

LEP was commissioned in 1989 and it is a perfect example of the concept of general purpose magnetic detectors with good tracking and particle identification properties. With the increase of the centre of mass energy in the collision, short-lived particles have a perceptible range before decaying, and an essential aspect of the event reconstruction is the proper identification of secondary vertices. This has been accomplished exploiting the precision and multi-track resolution power of solid state devices, combined with the pattern recognition capability of large volume gaseous tracking detectors.

Figure 1.14 shows the DELPHI detector with all its tracking components, the solenoid, the calorimeters and the particle identification detectors; more details can be found in [34]. The MVD (Micro Vertex Detector) was located in the heart of the DELPHI detector; its goal was to reconstruct secondary and tertiary vertices and find the tracks for the outer drift chambers. The MVD underwent several substantial upgrades, from single side to double side sensors and the implementation

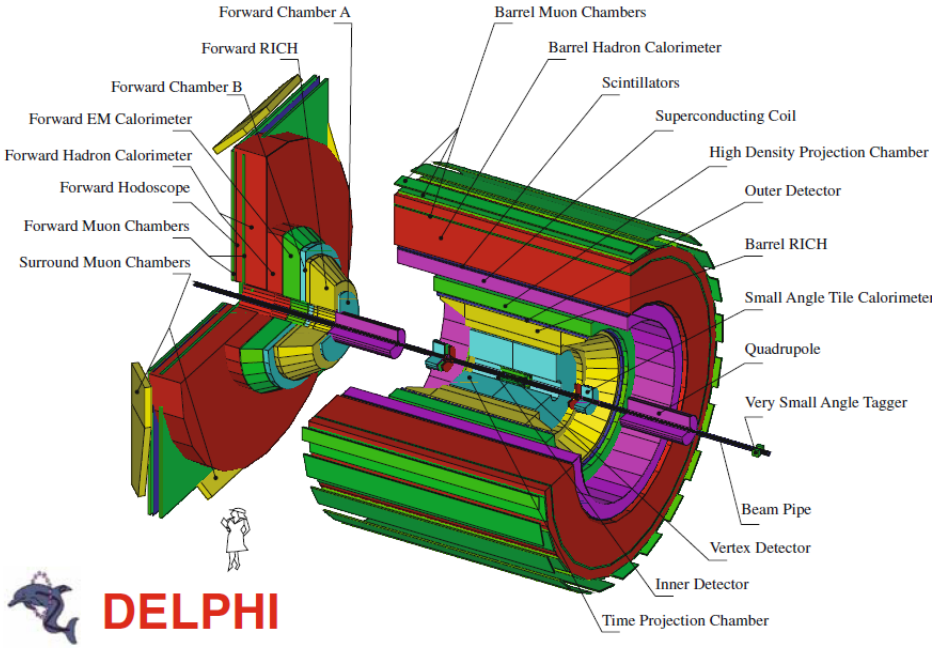

Figure 1.14: The DELPHI experiment [34].

of a forward structure, allowing tracking down to a polar angle of 10.5°. Starting in 1989, as the first silicon detector in the LEP experiment with two layers measuring the ϕ coordinate, it was upgraded to three layers in 1990, while in 1994, double side sensors were introduced to add the z-coordinate. The final setup, installed in 1997 [35], is shown in figure 1.15. DELPHI pioneered the use of hybrid pixel detectors. The DELPHI microvertex detector had a huge impact on the development of elementary particle physics. Fundamental improvements were achieved:

- in the lifetime measurements of heavy quarks and the τ lepton;
- in the tagging capability of heavy quarks.

The Higgs boson search during the LEP2 run was supported by the vertex b-tagging capability, since a Higgs in the accessible mass range would have been coupled predominantly to $b\bar{b}$. The absence of an excess of $b\bar{b}$ events established the lower limit on the Higgs mass [37]. With the very accurate tracking of the vertex detector the distance between the collision point and the decay point of the very short-lived particles can be measured. Figure 1.16(a) presents an example of a $b\bar{b}$ event recorded by the DELPHI vertex detector. It is quite evident that the distinction between the particles from the B decay is not straightforward. The situation becomes even more ambiguous because of tracking imperfections and the effects of multiple scattering. A good point resolution is necessary, since the

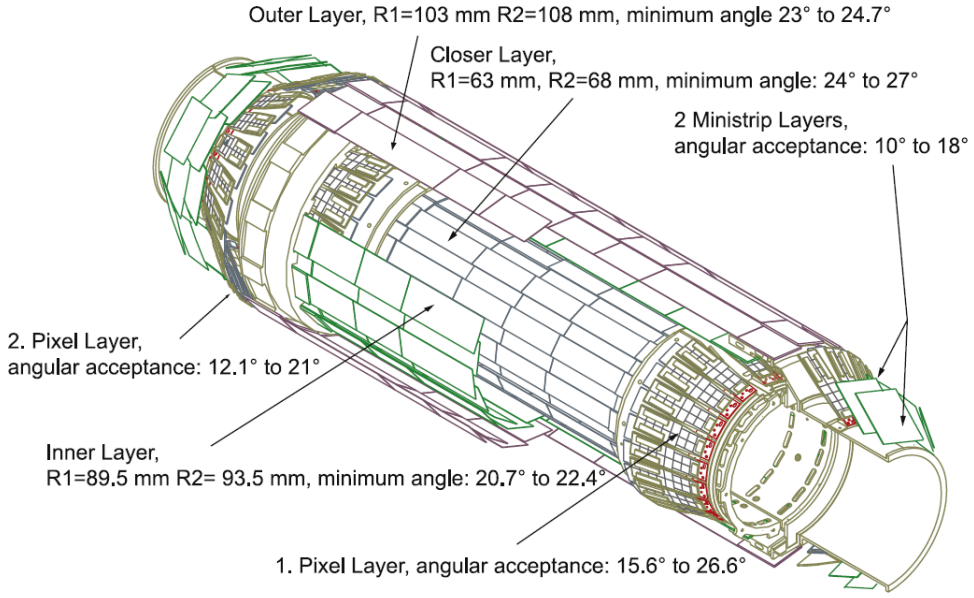

Figure 1.15: The DELPHI MVD [36].

first measured coordinates are several centimetres away from the primary vertex, while the primary to secondary vertices are in the millimetre range and the second to tertiary distances even less than a millimetre. However, the number of tracks not originating from the primary vertex is significant and even without a full reconstruction, the impact parameter d_0 allows for a good understanding of the process. Figure 1.16(b) shows a DELPHI $b\bar{b}$ event in the vertex detector with an exploded view of the primary interaction point.

1.2.3.2 The CMS vertex detector at LHC: searching the Higgs boson

The Compact Muon Solenoid experiment is a general purpose detector at LHC to explore physics at an unprecedented energy scale, the TeV one. CMS has to perform precision measurements of the parameters of the SM (Standard Model), but overall it is expected that the produced data will explain the electroweak symmetry breaking mechanism and provide evidence of physics beyond the SM. The processes related to the electroweak symmetry breaking have cross sections of the order of 1-10 fb. Assuming a canonical running time per year of T=10^7 s, a luminosity of L=10^{34}cm^{-2}s^{-1}=10^{-5}fb^{-1}s^{-1} is needed in order to accumulate $N = (L \cdot T)\sigma \sim$100 events per year for a process with a cross section σ = 1 fb. Luminosities in this range can only be achieved by large bunch intensities ($\sim 10^{11}$ protons/bunch), a large number of bunches or equivalently a small bunch spacing (25 ns) and a small beam size in the interaction region ($\sim$15-20 μm) [38].

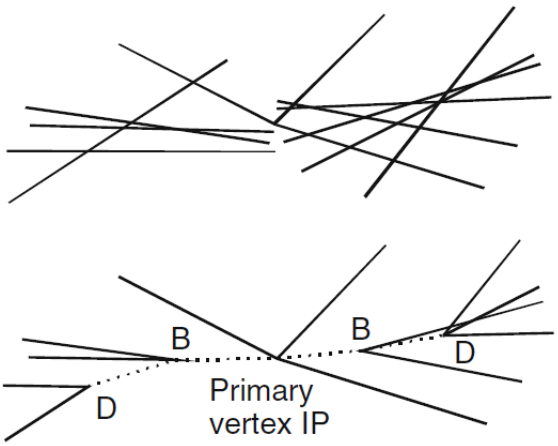

(a)

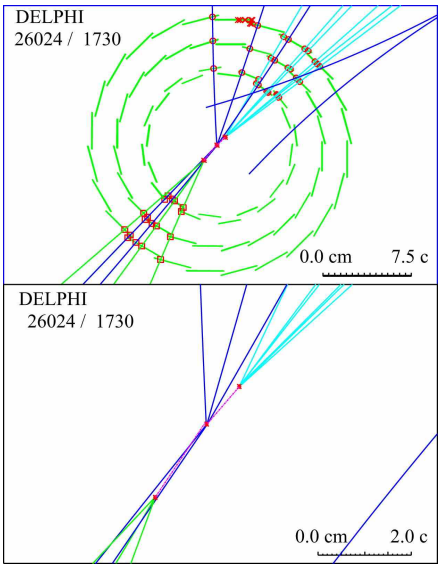

(b)

Figure 1.16: A $b\bar{b}$ event in the DELPHI vertex detector. a) The tracks (top) and the physics reconstruction (bottom); b) the different track points of the three detector planes together with the reconstructed tracks (top) and an enlarged view of the primary and secondary b-vertex (bottom).

The CMS detection system consists of a particle tracker, hadronic and electromagnetic calorimetry and muon chambers. The details of the detector can be found in figure 1.17 and a full description is given in [7]. The tracker and

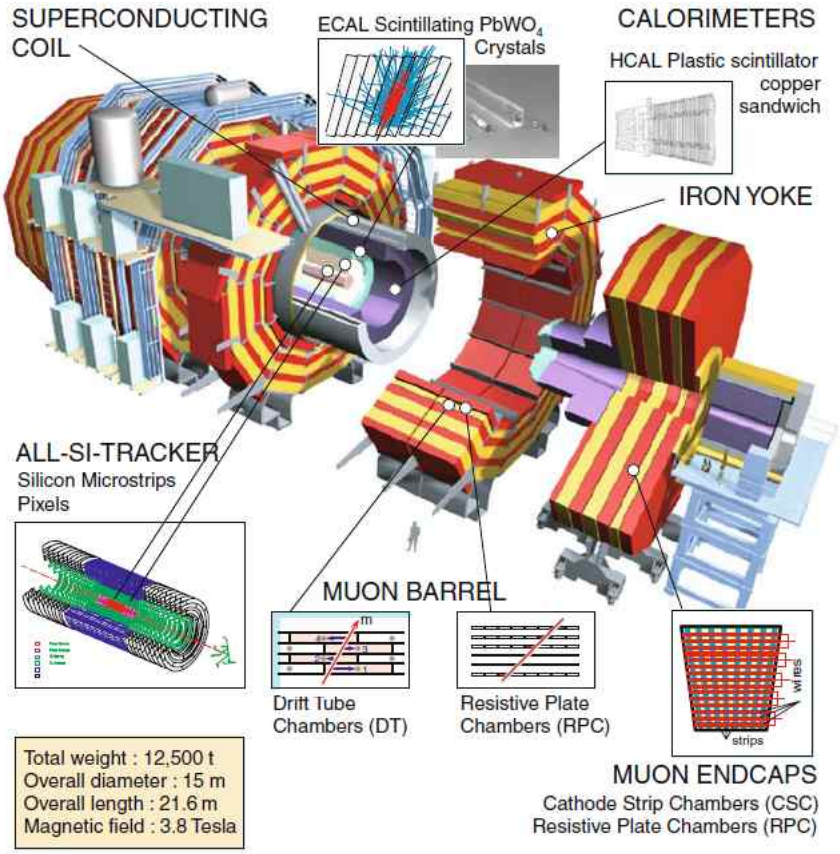

Figure 1.17: The CMS detector and its components.

calorimeters are compact enough to fit inside the world largest and strongest superconducting solenoid, which generates a uniform 4 T magnetic field over a volume of approximately 367 m^3. The detector is 16 m tall, 21.5 m long and weights 12500 ton.

In particular, the requirements of the detector included:

1. a good muon detection;
2. a high charged particle momentum resolution in the pixel tracker;
3. an excellent electromagnetic energy resolution;
4. a good missing transverse energy and dijet mass resolution.

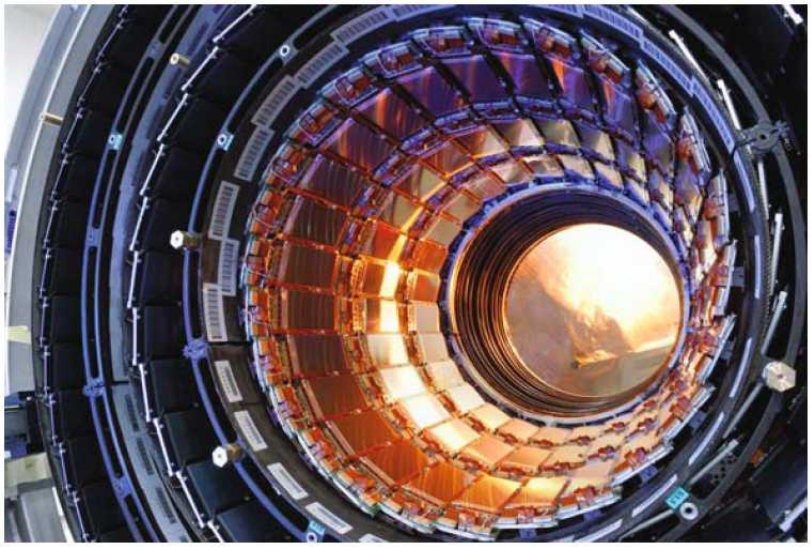

Figure 1.18: Three layers of the CMS tracker inner barrel detector.

The tracker is unique in that it is completely based on the silicon technology. In particular the CMS tracking system is designed to provide a precise and efficient measurement of the trajectories of charged particles emerging from the LHC collisions, as well as a precise reconstruction of secondary vertices. Therefore efficient and robust pattern recognition, fine granularity to resolve nearby tracks and fast response time to resolve bunch crossings are needed [39]. The tracker, surrounds the interaction point and has a length of 5.4 m and a diameter of 2.5 m.

The CMS tracker is composed of a pixel detector with three barrel layers (figure 1.18) and a silicon strip tracker with 10 barrel layers extending outwards to a radius of 1.1 m. Each system is completed by endcaps, which consist of two pixel disks and three small plus nine large disks of strips. As mentioned before, pixels are responsible for the vertexing and track seeding, while the outer strip tracker is responsible for the tracking with a large lever arm; no additional inner tracking device like a drift chamber or transition radiation tracker is installed. About 1440 pixel and 15148 strip detector modules build up the tracker; 66 million pixel cells and 10 million strips are available [40].

Some examples of events[9] recorded by CMS in 2010 are displayed in figure 1.19. In particular, figure 1.19(a) shows a candidate for the production of a top quark pair in CMS, where both top quarks decay into a W and a b quark, and both the W particles decay into a muon and neutrino. This results in two muons (red tracks), two jets tagged as b-quark jets and missing energy (from the escaping neutrinos). Figure 1.19(b) presents the production of a W boson, which decays

[9] http://press.web.cern.ch/press/PressReleases/Releases2010/PR15.10E.html

into an electron (blue track) and an invisible neutrino (arrow).

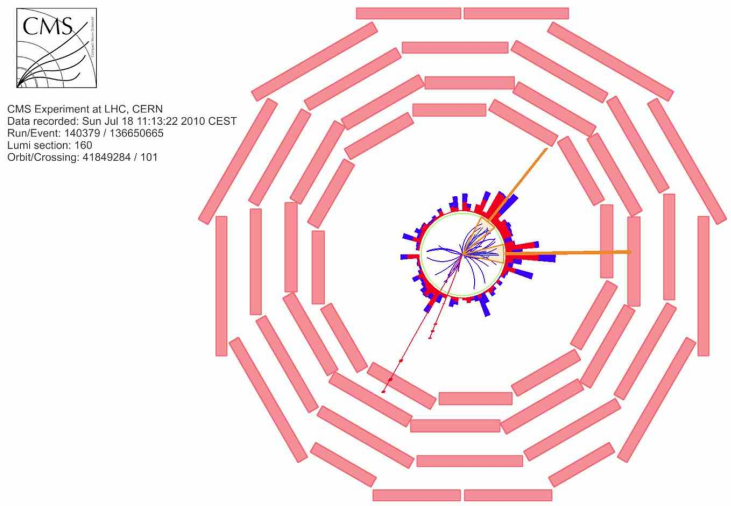

(a)

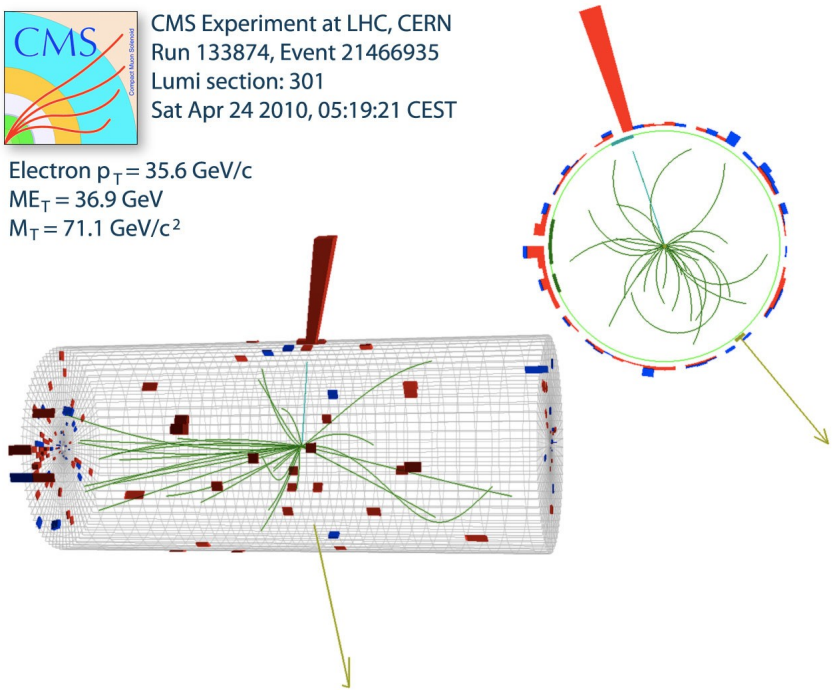

(b)

Figure 1.19: CMS events: a) a candidate for the production of a top quark pair; b) the production of a W boson.

As seen so far, especially with the DELPHI and CMS detectors, silicon track-

ing devices are essential in understanding fundamental and elementary particle processes. In the next chapter a detailed description of their basic operating principles and main features is presented.

Chapter 2

The working principles of silicon microstrip detectors

Semiconductor detectors were used in nuclear physics for energy measurements since 1951 [41] and appeared on stage in high energy physics experiments in the early eighties as silicon diodes to measure the particle fluxes. When a large number of charged particles cross a silicon diode in fact the charges produced by the energy deposit create a current that can be measured.

In 1980 Kemmer [33] introduced the planar technology for the production of silicon radiation detectors. Such a technique allowed the segmentation of one side of the junction and the use of the signals recorded on these segments to determine the particle hit position. The improvement from macro-segments (strips) to microstrips was straightforward and these detectors became soon a common tool in high energy physics. The first silicon vertex detector was built in 1983 for the NA11 experiment at CERN, designed to measure charm lifetimes [42]. The experiment used single side detectors with a 20 μm strip pitch but a readout one of 60 μm given the huge (if compared to the detector) dimensions of the electronics. Figure 2.1 shows one of these silicon microstrip detectors: the sensor had an active area of 24×36 mm^2.

The success of silicon in fixed target experiments was followed by their use in 4π detectors. The main problem in these devices was to find space for the readout electronics which in addition should not introduce too much material into the acceptance. Without the rapid development of integrated circuits, silicon detectors could not have been used in this geometry. At the beginning most experiments used single side detectors; the first double side 4π silicon detector was the one developed by ALEPH at LEP [43]. Since then, silicon has become a must for vertex detectors, as shown by all the LHC experiments; the CMS experiment exploits the largest amount of silicon, corresponding to 214 m^2 and 76 million readout channels (figure 2.2 [44]).

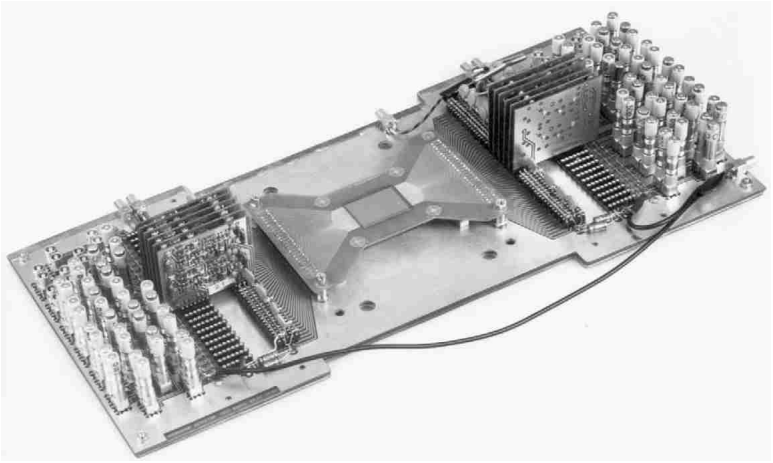

Figure 2.1: The NA11 silicon microstrip detector and its electronics [4].

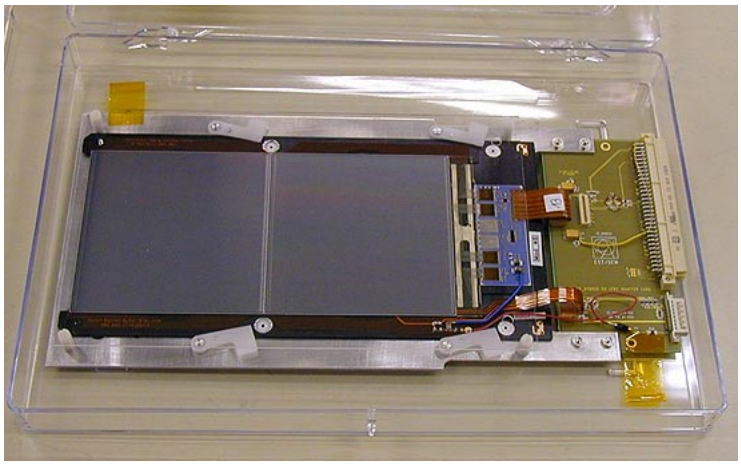

Figure 2.2: The CMS silicon microstrip detector; two silicon sensors of about 10×10 cm^2, the support frame and the frontend electronics are visible [44].

This chapter presents a brief review of the basic properties of semiconductor materials to concentrate then on the working principles of silicon position sensitive devices. Among the huge variety of silicon sensors, silicon microstrip detectors will be treated in detail since they represent the main topic of this thesis. The last part of the chapter presents an example of an application of the microstrip detectors in the field of bent crystal physics.

2.1 The basic semiconductor properties

This section presents briefly the basic properties of semiconductor materials and their electrical characteristics starting from intrinsic semiconductors. A detailed description can be found in [45].

2.1.1 The energy band structure

Semiconductors are crystalline materials whose outer shell atomic levels present an energy band structure (figure 2.3) consisting of a *valence band*, a *"forbidden" energy gap* and a *conduction band*; in the figure the band structures for conductors and insulators are also illustrated.

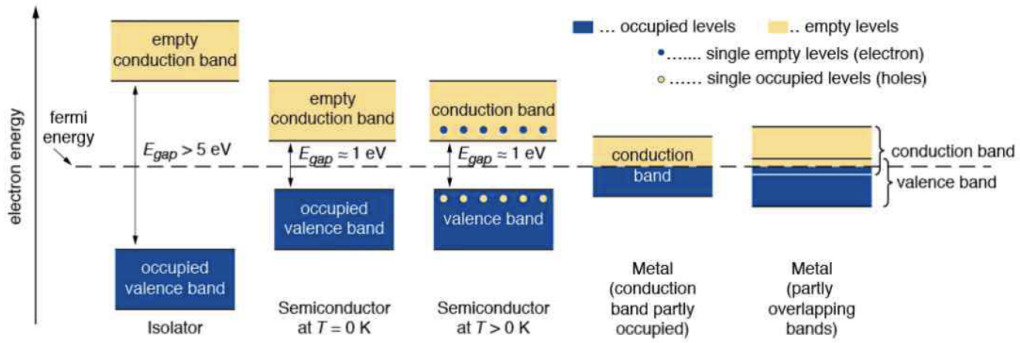

Figure 2.3: The energy band structure of insulators, semiconductors and conductors.

The *energy bands* are regions composed by many discrete closely spaced levels that can be considered as a continuum; on the contrary, the *"forbidden" energy gap* is a region in which there are no available energy levels. Electrons are free to move in the so-called conduction band while they are bound to the lattice atoms in the valence band.

The three types of material are characterized by the energy gap whose value depends on the temperature:

- in a conductor it is absent, therefore it is easy for thermally excited electrons to jump into the conduction band where they are free to move. A current will thus flow when an electric field is applied;
- in an insulator it is large. At room temperature the electrons stay all in the valence band; the thermal energy is not enough to excite them across this gap. No current will flow when an external electric field is applied;
- in a semiconductor it has an intermediate value (1.1 eV in silicon and 0.7 eV in germanium), therefore just few electrons can be thermally excited into the conduction band.

2.1.2 The charge carriers in semiconductors

Silicon has four valence electrons, therefore four covalent bonds are formed for each atom. At room temperature some bonds may be broken by the thermal energy: the valence electron is thus excited into the conduction band leaving a *hole* in its original position. This hole is filled by an adjacent electron, leaving in turn a vacancy and so on. The different temperature conditions are illustrated in figure 2.4. Since the holes are positive with respect to the sea of negative charge

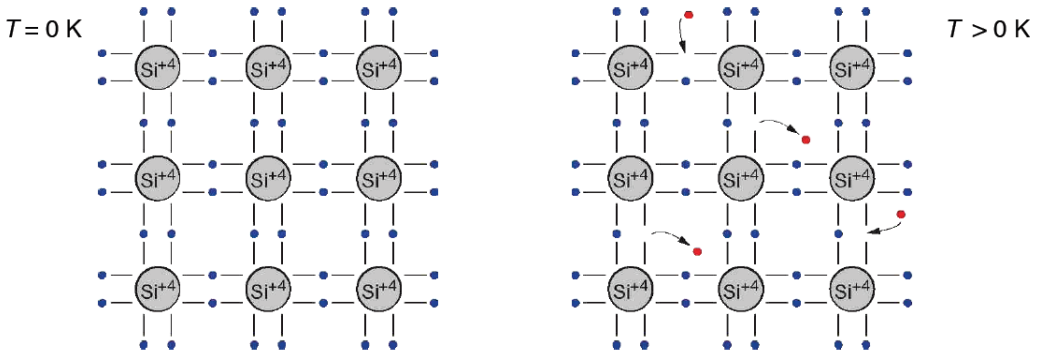

Figure 2.4: The silicon structure: at 0 K all the electrons are bound (left); at higher temperature some bonds may be broken by the thermal excitation leaving a hole in the valence band (right). The valence electrons are represented in blue, while the conduction ones in red.

(represented by the electrons in the valence band), they can be considered as positive charge carriers whose movement generates an electric current. The electric current in a semiconductor is thus determined by:

- the movement of the electrons in the conduction band;
- the movement of the holes in the valence band.

2.1.3 The intrinsic charge carrier concentration

At the thermal equilibrium the occupation probability of a state with an energy E at the temperature T is given by the Fermi-Dirac statistics [46]:

$$F(E) = \frac{1}{1+e^{\frac{E-E_F}{kT}}} \tag{2.1}$$

where E_F is the Fermi level that is the energy level with an occupation probability of 50% and k is the Boltzmann constant. In the conduction band the density of the states occupied by the electrons is given by:

$$n = \int_{E_c}^{\infty} N(E)F(E)\,\mathrm{d}E \tag{2.2}$$

where E_c is the minimum energy of the conduction band and $N(E)$ is the density of the states. Applying the Boltzmann statistics this integral can be approximated as:

$$n = N_C e^{-\frac{E_C-E_F}{kT}} \tag{2.3}$$

in which N_C represents the density of states in the conduction band. In a similar way, the hole concentration can be obtained:

$$p = N_V\, e^{-\frac{E_F-E_V}{kT}} \tag{2.4}$$

where N_V is the density of states in the valence band and E_V is the maximum energy of the valence band. N_C and N_V vary as $T^{3/2}$ [46].

In an intrinsic semiconductor, the thermal energy may excite the valence electrons into the conduction band leaving the same number of holes in the valence band, therefore $n = p = n_i$ where n_i is the intrinsic carrier density. There is a dynamic equilibrium between the electron-hole pairs thermal generation and the recombination of electrons in the conduction band with the holes in the valence band. The neutrality condition leads to:

$$E_F = E_i = \frac{E_C+E_V}{2} + \frac{kT}{2}\ln\left(\frac{N_V}{N_C}\right) \tag{2.5}$$

This means that the Fermi level of a pure semiconductor is located in the middle of the band gap, as presented in figure 2.5. The intrinsic carrier density can be obtained using equation 2.3 and 2.4:

$$pn = n_i^2 = N_C N_V e^{-\frac{E_g}{kT}} \tag{2.6}$$

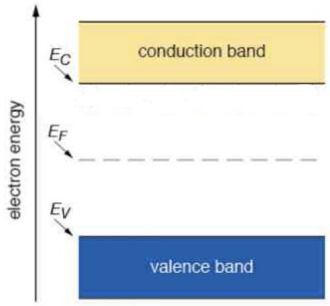

Figure 2.5: The Fermi level of a pure semiconductor.

Atomic number Z	14
Atomic weight A	28.0855
Atomic density [cm^{-3}]	4.99·10^{22}
Density ρ [g/cm^{-3}]	2.328
Density of states in the conduction band N_C [cm^{-3}]	3.22·10^{19}
Density of states in the valence band N_V [cm^{-3}]	1.83·10^{19}
Diamond type lattice constant [nm]	0.5431
Dielectric constant (relative) ϵ_r	11.7
Energy gap E_g (300 K) [eV]	1.124
Energy gap E_g (0 K) [eV]	1.170
Electron mobility μ_e (300 K) [cm^2 V^{-1}s^{-1}]	1350
Hole mobility μ_h (300 K) [cm^2 V^{-1}s^{-1}]	450
Fano factor F	0.115
Intrinsic carrier density n_i [cm^{-3}]	1.45·10^{-10}
Maximum electric field E_{max} [V/μm]	30

Table 2.1: Some physical properties of silicon [4].

in which E_g = E_C-E_V is the energy gap. Thus:

$$n_i = \sqrt{N_C N_V} e^{-\frac{E_g}{2kT}} \tag{2.7}$$

Therefore n_i varies rapidly with the temperature.

Table 2.1 presents some physical properties of silicon. Note that $n_i \sim 10^{10}$ cm^{-3} at T = 300 K and the atomic density is of the order of 10^{22} atoms/cm^3; this means that only 1 in 10^{12} silicon atoms is ionized, with a concentration which is very small.

If an external electric field is applied, holes and electrons start to drift with a

velocity v_h and v_e:

$$\begin{aligned} v_e &= \mu_e \mathcal{E} \\ v_h &= \mu_h \mathcal{E} \end{aligned} \tag{2.8}$$

where $\mathcal{E}$ is the electric field intensity and μ_e and μ_h are the mobilities of electrons and holes respectively[1] (table 2.1).

2.2 The doped semiconductors

Intrinsic semiconductors have been treated so far; this section deals with the *doped* or extrinsic semiconductors where large concentrations of free electrons (n-type, figure 2.6) or holes (p-type, figure 2.7) are achieved by moving the Fermi level close to the conduction or valence band. The procedure consists in the introduction of a small amount of dopants having one more, or one less, valence electron in the outer shell.

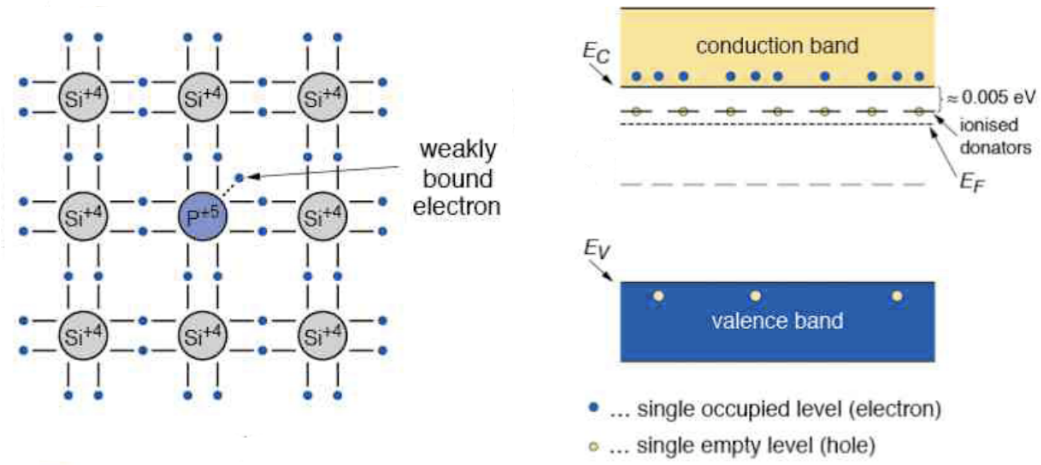

Figure 2.6: The donor impurities create a n-type material; the Fermi level is close to the conduction band.

Given that silicon is an element of group IV (with four valence electrons) the n- and p-type materials are obtained by adding respectively *donor* elements from group V (i.e. phosphorus) or *acceptor* elements from group III (i.e. boron).

In the first case four electrons of the dopants form a covalent bond with the silicon atoms while the fifth is weakly bound; at room temperature the *extra* electron is easily excited in the conduction band, increasing the conductivity of the

[1] For a given material the mobilities depend on the temperature T.

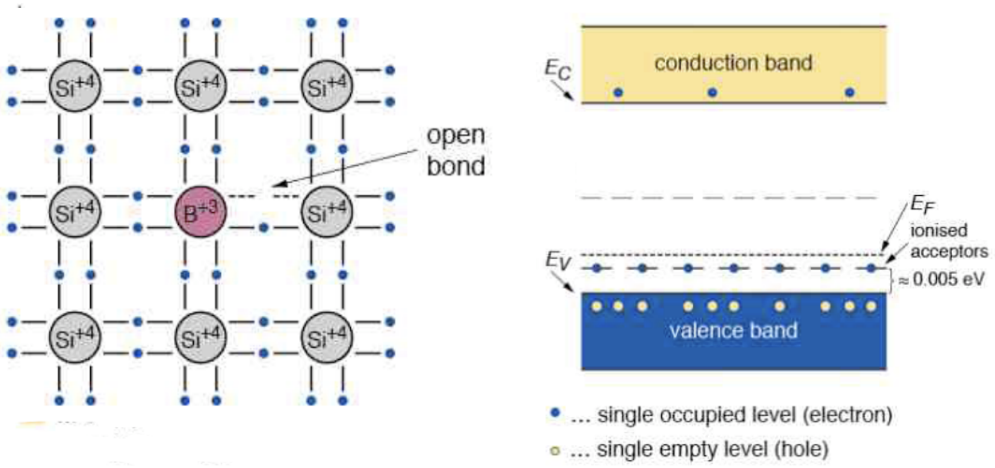

Figure 2.7: The acceptor impurities create a p-type material; the Fermi level is close to the valence band.

semiconductor. In a n-type material the current is mainly due to the movement of electrons (majority charge carriers) while the holes give a small contribution (minority carriers). The Fermi level is close to the conduction band.

Silicon can be doped with trivalent impurities which have one valence electron less; in this case three covalent bonds are formed while the fourth remains incomplete. This vacancy (hole) is filled by an adjacent electron and so on; the holes become the majority charge carriers and the electrons the minority ones. The Fermi level shifts close to the valence band.

At the thermal equilibrium the *law of mass action* holds also for a doped material:

$$pn = n_i^2 = AT^3 e^{-\frac{E_g}{kT}} \tag{2.9}$$

where n_i is the intrinsic concentration given in equation 2.7. Considering the neutrality of the crystal, the positive and negative charge densities must be equal:

$$N_D + p = N_A + n \tag{2.10}$$

where N_D and N_A are the donor and acceptor concentrations. In a n-type material, where N_A=0 and $n \gg p$, the electron density is approximately the same of the dopant concentration:

$$n \simeq N_D \tag{2.11}$$

The minority carrier concentration is therefore:

$$p \simeq \frac{n_i^2}{N_D} \tag{2.12}$$

An analog result can be found for p-type materials.

2.3 The pn junction

The only way to use a semiconductor as a particle detector is to deplete it of free carriers building the so-called *pn junction* and applying a reverse bias. In the following these two basic concepts are explained.

When a p-type semiconductor and a n-type one get in touch, the large carrier concentration gradients at the junction cause an initial carrier diffusion: holes from the p-side diffuse into the n-side and electrons from the n-side go into the p-side, as presented in figure 2.8. Negative acceptor ions and positive donor ions remain uncompensated in the p-side and in the n-side respectively forming the so-called *depleted region*.

The electric field created by the space charge region opposes the diffusion process of both electrons and holes, while thermally generated electron-hole pairs in the depleted region drift towards the neutral ones. The total electrostatic potential difference between the p-side and the n-side neutral regions at the thermal equilibrium is called *built-in potential* V_{bi} [45]:

$$V_{bi} = \frac{kT}{q} \ln \frac{N_A N_D}{n_i^2} \tag{2.13}$$

and it is of the order of a few hundred milliVolts. Ionizing radiation crossing the depleted region will generate electron-hole pairs which drift under the effect of the electric field. If electrical contacts are placed on both ends of the junction, a current signal proportional to the ionization will then be detected.

The width of the depleted region is generally small and depends on the concentrations of the donor and acceptor impurities. It can be determined using the Poisson equation [45]:

$$W = x_n + x_p = \sqrt{\frac{2\epsilon_{Si} V_{bi}}{q} \cdot \frac{(N_A + N_D)}{N_A N_D}} \tag{2.14}$$

where x_n and x_p are the widths of the depletion zone on the n-side and p-side respectively and ϵ_{Si} is the absolute dielectric constant of silicon[2]. For a p^+n junction ($N_A \gg N_D$) this leads to a depletion region almost entirely on the n-side of the junction, which represents the active particle detection volume, and very shallow on the p-side. In this case the width of the depletion region becomes:

$$W \approx x_n \approx \sqrt{\frac{2\epsilon_{Si} V_{bi}}{q N_D}} \tag{2.15}$$

For typical values of N_A=10^{15} cm^{-3}, N_D=5·10^{12} cm^{-3} and V_{bi}=0.5 V, the width of the depleted layer for the p^+n junction is of the order of 11 μm.

[2]The absolute dielectric constant for silicon is defined as $\epsilon_{Si} = \epsilon_r \cdot \epsilon_0$, where ϵ_r is the relative dielectric constant (reported in table 2.1) and ϵ_0 is the vacuum permittivity (8.85·10^{-12} F/m).

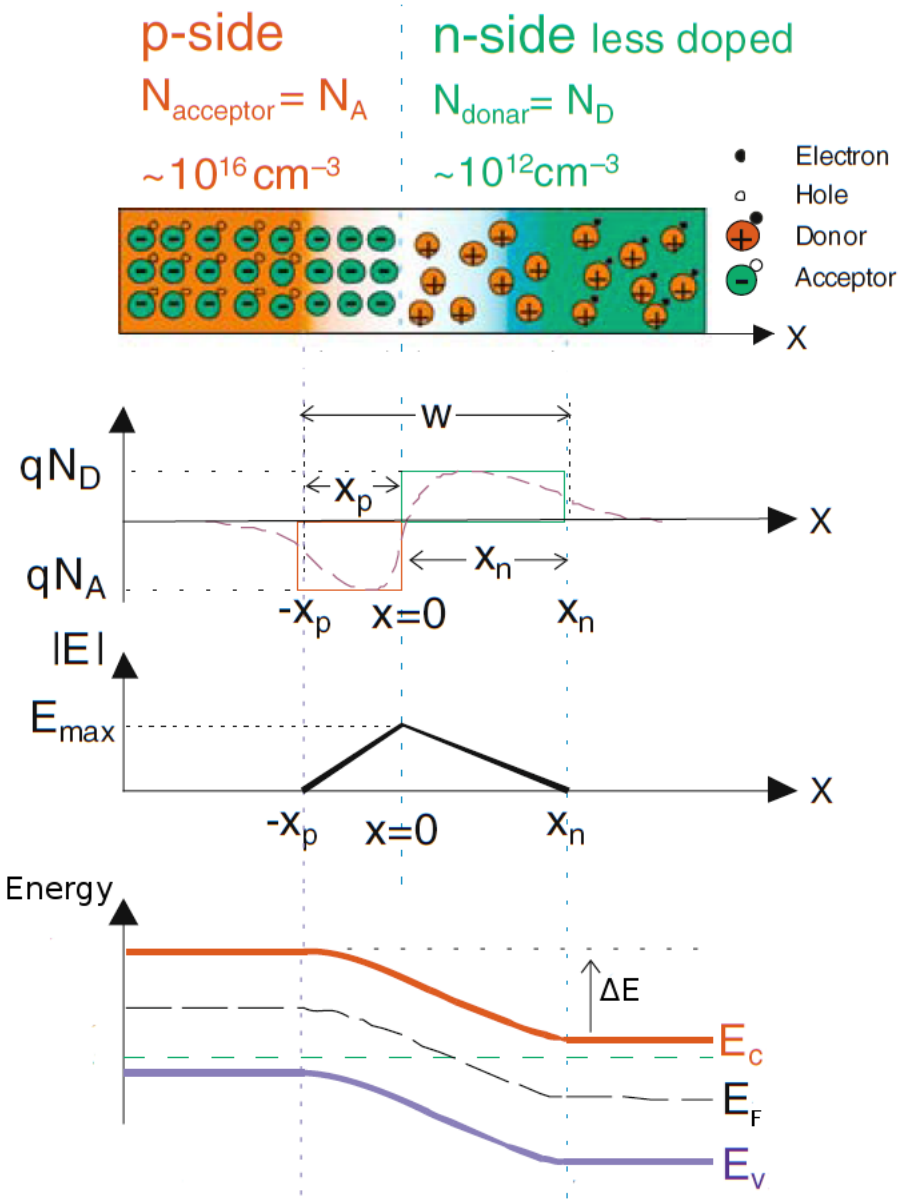

Figure 2.8: From top to bottom: schematic representation of a pn junction, its charge density, the electric field intensity and the potential.

2.3.1 The reverse biased junction

A depleted junction can be used as a detector: the charge created by the ionizing radiation crossing the depleted region can in fact be collected at the junction edges and then readout. The charge which originates in the undepleted (neutral) zone recombines with the free carriers and gets lost. Increasing the width of the space charge region the collected signal increases; this can be obtained by applying an external potential difference, V_{bias}, of the same sign of V_{bi}. The height of the barrier thus becomes:

$$V_B = V_{bias} + V_{bi} \tag{2.16}$$

and the junction is reverse biased (figure 2.9). In this case, assuming N_A=10^{15} cm^{-3}

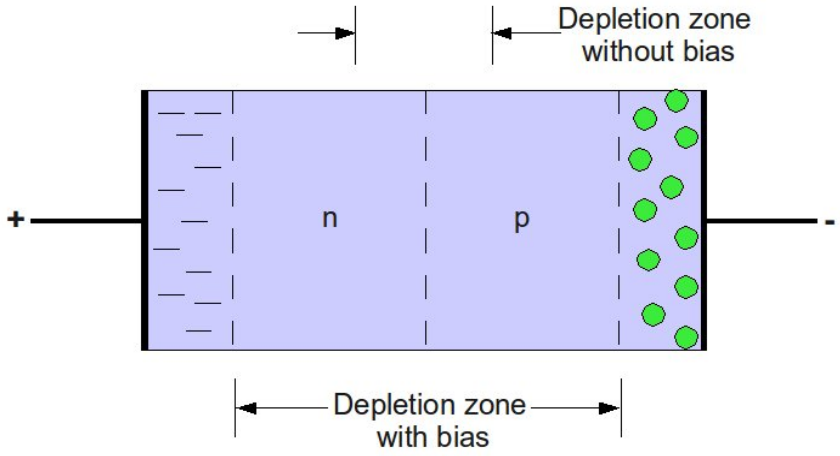

Figure 2.9: The reverse biased junction; the positive voltage is applied to the n-side and the negative to the p-side.

and N_D=5·10^{12} cm^{-3} for a p$^+$n junction, the width of the depletion layer on the p-side is 0.4 μm while on the n-side is 300 μm applying a biasing voltage of 100 V [47].

In such detectors the background is due to the thermally generated minority carriers. The depleted region is free of majority carriers but at the equilibrium electron-hole pairs are continuously generated within the crystal volume. If the electric field is absent, the created carriers recombine; on the other hand, if an electric field is applied, the pairs are separated and have a small possibility to recombine. Electrons and holes drift under the influence of the electric field originating the so-called *leakage* or *reverse current*. Depending on the region where the charge generation occurs, two components contribute to this current:

- a *generation current* (J_{gen}) due to the charge created within the depleted zone. Assuming that in the depleted zone the carrier density is very low (n,$p \ll n_i$), the generation current is:

$$J_{gen} = \frac{qn_iW}{2\tau_0} \tag{2.17}$$

  where τ_0 is the effective lifetime of the minority carriers within the depleted zone [47]. This current contribution is proportional to the width of the depleted zone W, which in turn is proportional to $\sqrt{V_B}$. The temperature dependence of J_{gen} is through n_i. Using equation 2.9, it can be shown that n_i increases of a factor two when the temperature increases of 8 K; it is therefore important to keep the temperature constant in order to have a stable operation condition of the detector;

- a *diffusion current* (J_{diff}) caused by the charge originated in the neutral zone and diffusing to the space charge region. In the neutral region in fact there is no electric field and electron-hole pairs created there recombine. If however they are generated close to the depleted region, they have a probability to diffuse in it before the recombination process. Indicating with τ_n and τ_p the lifetimes of the electrons in the p-region and the holes in the n-region, the widths of the layer from which the carriers may diffuse are:

$$\begin{aligned} L_n &= \sqrt{D_n\tau_n} \\ L_p &= \sqrt{D_p\tau_p} \end{aligned} \tag{2.18}$$

  where D_n and D_p are the diffusion constants for the electrons and holes. The diffusion current densities can be expressed as:

$$\begin{aligned} J_{diff,n} &= \frac{qn_pL_n}{\tau_n} \\ J_{diff,p} &= \frac{qp_nL_p}{\tau_p} \end{aligned} \tag{2.19}$$

  where n_p is the density of electrons in the p-side and p_n the density of holes in the n-side. These equations describe the net generation rate of carriers in the neutral regions.

In normal operating conditions a silicon detector is fully depleted therefore the measured leakage current is the generation one. In order to have a low leakage current, special attention should be given to the lifetime of the minority carriers. Since the lifetime depends on the generation and recombination processes due

to the presence of impurity atoms, the crystal should be kept clean during the processing [47].

Since in the depleted region the charge depends on the voltage, a junction capacitance can be defined as:

$$C_j = \frac{\mathrm{dQ}}{\mathrm{dV_B}} = \frac{\mathrm{dQ}}{\mathrm{dW}}\frac{\mathrm{dW}}{\mathrm{dV_B}} = \sqrt{\frac{q\epsilon_{Si}N_A N_D}{2(N_A+N_D)V_B}} \tag{2.20}$$

where dQ represents the charge increment; for the case in which $N_A \gg N_D$ equation 2.20 becomes:

$$C_j = \sqrt{\frac{q\epsilon_{Si}N_D}{2V_B}} \tag{2.21}$$

The junction capacitance decreases increasing the bias voltage and reaches a minimum value at the full depletion voltage. Figure 2.10 shows the capacitance of a silicon detector as a function of the bias voltage.

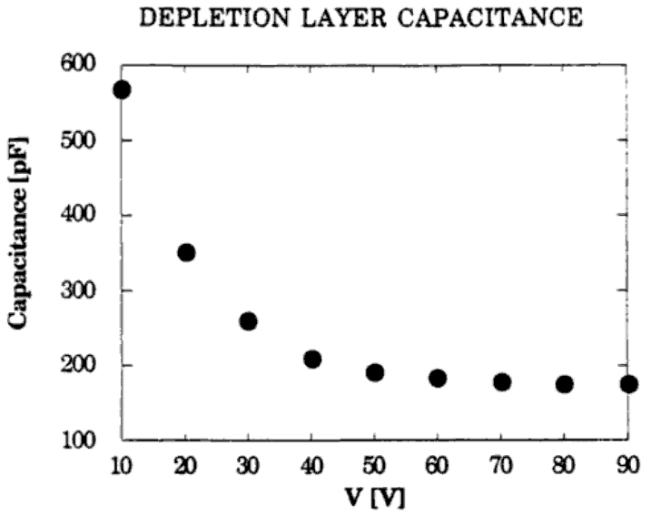

Figure 2.10: Depletion layer capacitance as a function of the applied voltage measured in a detector with a surface of 4.5 cm^2 [47].

2.4 Silicon detector features

Silicon is the preferred material for high precision tracking detectors, as well as for a wide range of radiation detectors, for several reasons [48]:

- its very good intrinsic energy resolution. The energy resolution of a detector is defined as follows [49]:

$$R = 2.35\sqrt{\frac{Fw}{E}} \tag{2.22}$$

where w is the average energy required to create an electron-hole pair, F is the *Fano factor*[3] and E is the energy of the particle. Silicon detectors have a very good intrinsic energy resolution since the average energy to create an electron-hole pair is 3.6 eV, a small value if compared to the ionization energy in a gaseous detector ($\sim$30 eV) or to the one required to extract a photon in a scintillator ($\sim$300 eV). Moreover the Fano factor for silicon is of the order of 0.12 which improves the resolution value;

- its energy band gap of 1.1 eV, small enough to allow a large production of charge carriers from a MIP[4] (Minimum Ionizing Particle);

- the possibility to achieve very high precision position measurements (below 10 μm). Gaseous tracking detectors, for instance, have a limited precision of some tens of microns due to the diffusive spread of the electron cloud and for this reason they are not adequate for precision vertex location. Studies performed on high precision liquid tracking detectors have also shown many problems, mainly related to the medium purity preservation. In contrast, silicon devices can be exposed to the atmosphere and assembled in complex geometries, with no degradation of their bulk electron lifetime characteristics [46];

- it is a low Z element of excellent mechanical properties and therefore an ideal material to use in tracking detectors where the multiple scattering represents an important problem;

- the possibility of selective growth of insulating layers (SiO_2 and Si_2N_3) with the microlitographic techniques.

[3]The Fano factor depends on all the various fundamental processes which can lead to an energy transfer in the detector. This includes all the reactions which do not lead to ionization, as for instance the phonon excitations [50].

[4]A minimum ionizing particle (MIP) is a particle whose average energy loss rate in matter is close to the minimum [15].

2.5 The breakthrough: microstrip detectors to measure the hit position

The position localization capability of silicon detectors is obtained by segmenting the large area of the pn diode into many small regions [51]: strip like shaped implants act as independent charge collecting electrodes. Two dimensional position measurements can be achieved by segmenting the wafer backside as it is done in the double side technology. Figure 2.11 presents the two different geometries.

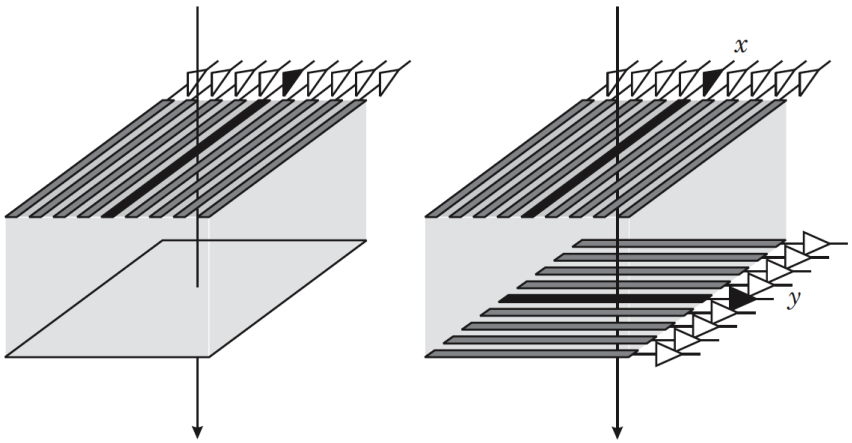

Figure 2.11: One (left) and two (right) dimensional position measurement with silicon detectors.

2.5.1 Single side versus double side technology

The basic scheme of a silicon microstrip detector is presented in figure 2.12. A block of high purity n-type silicon features parallel strips of p^+ silicon on one side and a layer of highly doped n^+ silicon on the other. The p^+ layer is needed to deplete the junction, while the n^+ one to prevent the depletion zone from reaching the backplane and to ensure a good ohmic contact. A metal layer has to be deposited on the p^+ strips to allow the connection with the electronics. The silicon surface is passivated to protect the silicon itself from the environment.

When an incident particle ionizes the n-bulk and the detector is reverse biased, the resulting holes and electrons drift towards the p^+ and n^+ sides. The charge produced by the energy deposit of the particles spreads during the drift towards the electrodes with a Gaussian distribution with a full width at half maximum (FWHM)$<$20 μm. Typical silicon microstrip detectors have a strip pitch (the distance between two contiguous strip centers) ranging from 20 μm to 250 μm and a

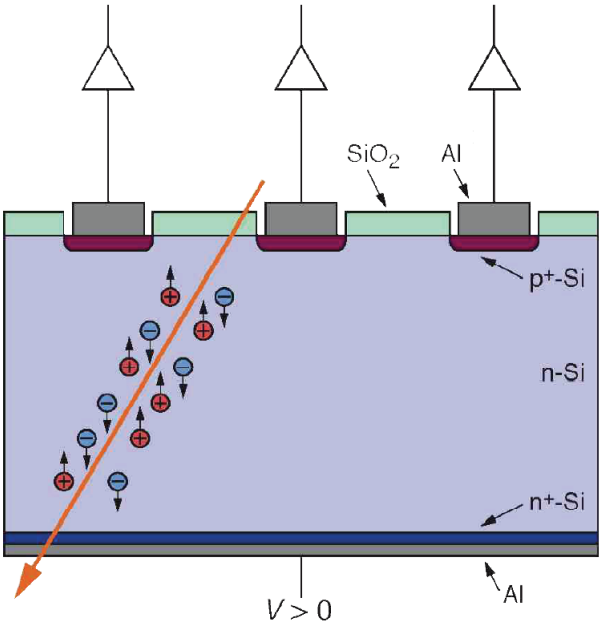

Figure 2.12: Cross section of a DC-coupled microstrip detector.

thickness between 250 and 500 μm[5]. These parameters depend on the application and have to be optimized taking into account the readout electronics.

In double side silicon detectors the strips are implanted on both sides of the bulk material usually with a different orientation[6] allowing the reconstruction of the hit in 2D. The correlation between the pulse heights recorded on both sides of the detector can be used to solve the ambiguities due to multiple hits [4]. Furthermore by combining two measurements on one piece of bulk silicon the overall material budget is substantially reduced. A schematic cross section of a double side detector is shown in figure 2.13. The strip implants are p^+-type on the junction side and n^+-type on the ohmic one. One of the main difficulties in the manufacturing of double side detectors is the implantation of strips on the ohmic side. The presence of the fixed positive charge at the SiO_2 interface in fact attracts electrons (figure 2.14) which short circuit the n^+ strips. To be able to readout the n^+ strips signals it is necessary to insulate them one from the other. Several solutions have been proposed (figure 2.15) [52]:

- the *p-stop technology* which requires a p^+ implant between each n^+ strip;

[5]A larger thickness requires a much larger bias voltage (equation 2.15). This could represent a problem in the charge collection by the electrodes and from the point of view of the signal to noise ratio.

[6]Common strip orientations are 90° or a small stereo angle like 0.1-0.2° [46].

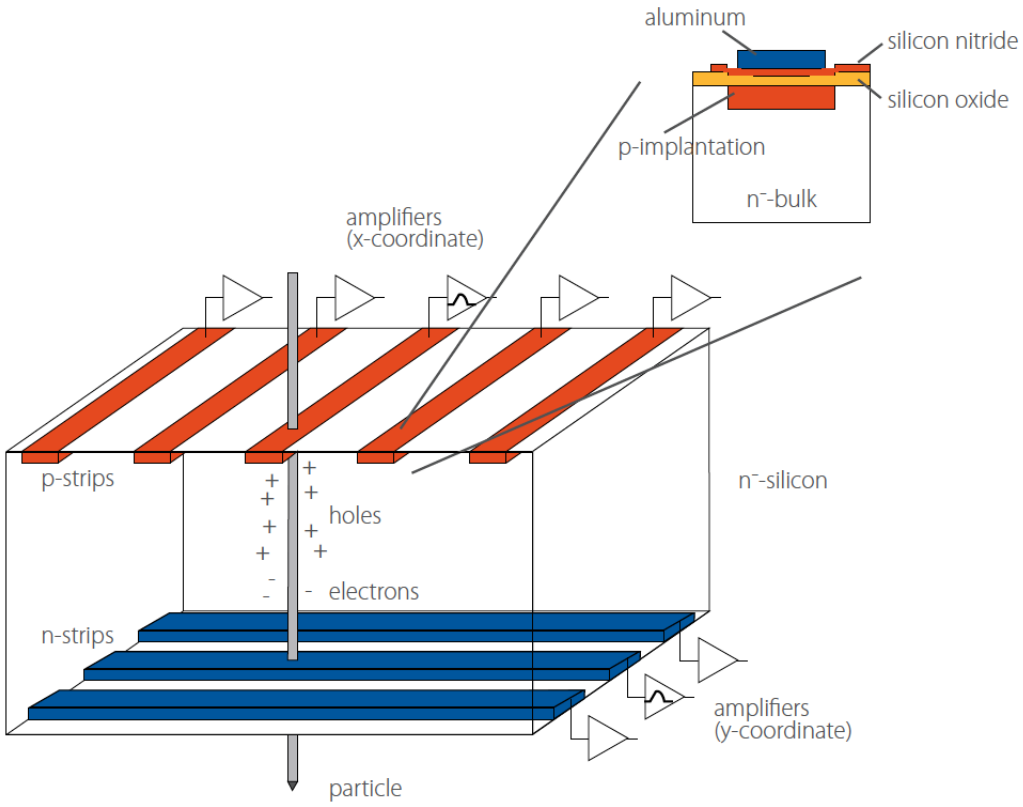

Figure 2.13: Schematic cross section of a double side silicon microstrip detector.

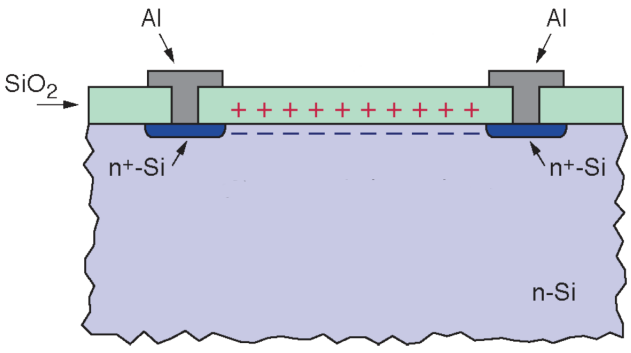

Figure 2.14: Positive charges in the oxide attract electrons in the n-bulk material to the interface, forming an electron accumulation layer that short circuits the strips.

- the *p-spray technology* where a layer of p-dopants is diffused on the whole surface;
- the *field plate technology* which increases the aluminium strip widths, applying a negative potential to repel the electrons in the strip region.

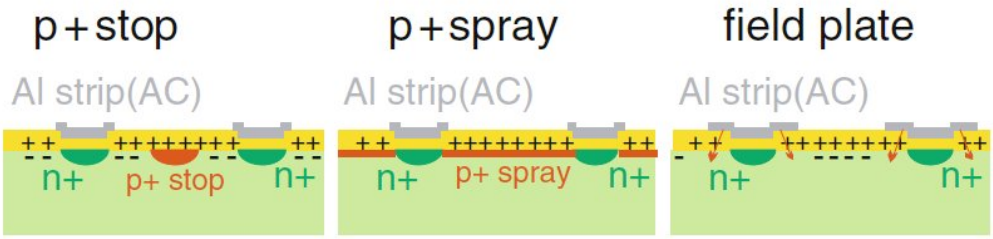

Figure 2.15: The basic mechanisms to avoid the short circuit of the n^+ strips on the ohmic side.

2.5.2 AC-DC coupling and biasing

In order to allow the connection with the input of the amplifier of the readout electronics, a metal layer (typically aluminum) is deposited on the top of the strip implants. In case of a direct contact with the strip (*DC-coupling*) the detector leakage current would flow right into the amplifier (figure 2.12); if this current is large, noise would increase and the saturation of the amplifier may be reached. Therefore in most cases capacitive coupling is used. In modern applications the capacitors are integrated into the detector; external capacitors are in fact difficult to fit and the number of connections (bondings) doubles. Internal capacitors are implanted by inserting an insulating SiO_2 layer between the strip implant and the metallization[7], as presented in figure 2.16. A failure in the oxide is called *pinhole*[8], and it allows the DC current to flow into the amplifier. In an *AC-coupled* configuration, the leakage current is filtered by the capacitor. DELPHI used integrated coupling capacitors of 7-15 pF/cm, while the CMS experiment reaches values of the order of 300-600 pF/cm depending on the geometry.

[7]The metal layer is from 50 nm to 200 nm thick.

[8]Pinholes are caused by large voltage drops across the SiO_2 layer, which can locally break. The internal capacitors are built to withstand drops of up to 100 V. By contrast external capacitors break at far smaller voltages.

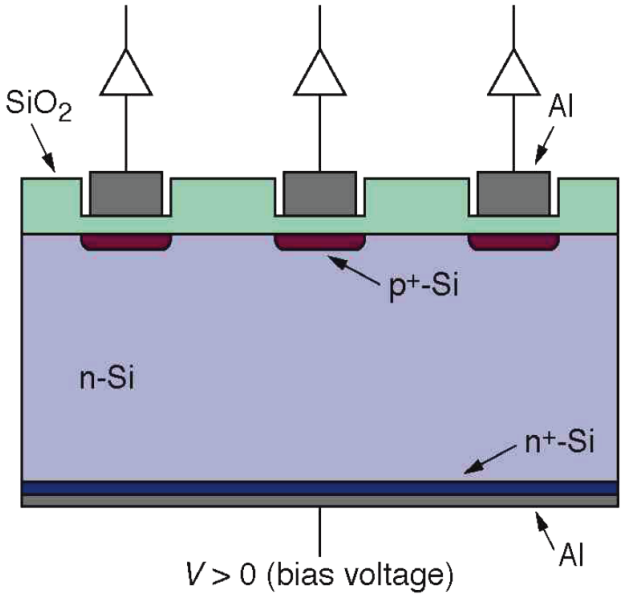

Figure 2.16: Cross section of an AC-coupled silicon microstrip detector.

A detector has to be fully depleted in order to detect particles. The full depletion voltage for a p^+n junction can be expressed in terms of the resistivity

$$\rho = \frac{1}{q\mu_n N_D} \tag{2.23}$$

using equation 2.15:

$$V_B = \frac{W^2}{2\epsilon_{Si}\rho\mu_n} \tag{2.24}$$

where μ_n is the majority carrier mobility for the n-type silicon and W is the detector thickness in case of a fully depleted detector. For a 300 μm thick detector with ρ=10 kΩ·cm, the full depletion voltage is about 32 V.
To reach the full depletion, the individual strip implants are connected to a "bias line" which provides a fixed potential to all the strips, through polysilicon resistors integrated in the detector. The value of these resistors has to be large, of the order of a few MΩ to limit the strip current: if the capacitor breaks in fact, the current goes directly into the amplifier. The bias resistors of the CMS silicon devices are of the order of 1-2 MΩ [53]. Figure 2.17 shows a cross section of a microstrip detector with integrated coupling capacitors and polysilicon bias resistors.

The sensor is surrounded by one or several "guard rings" that define the active volume of the detector, protect the sensor from field border effects (like charge accumulation at the silicon edges) and prevent the leakage current from being absorbed by the edge strips [54]. Figure 2.18 presents a top view of the different elements of a silicon microstrip detector.

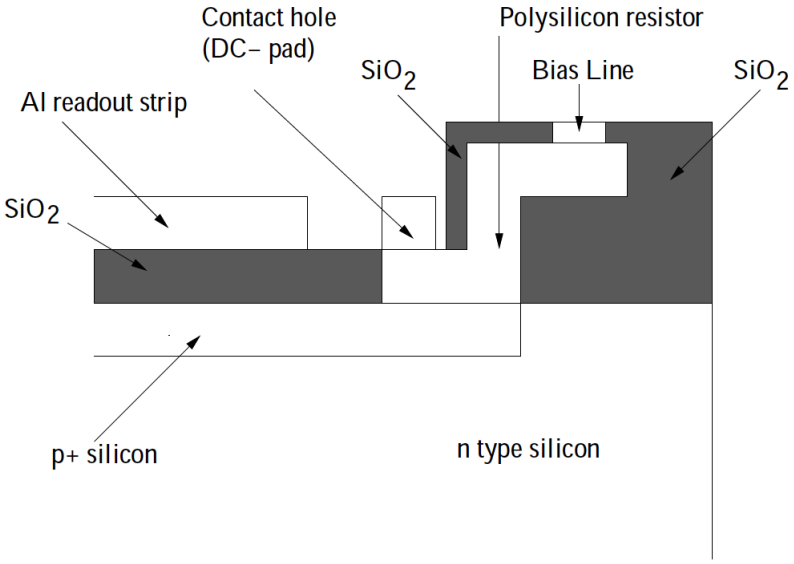

Figure 2.17: Cross section of a microstrip detector with integrated coupling capacitors and polysilicon biasing resistors.

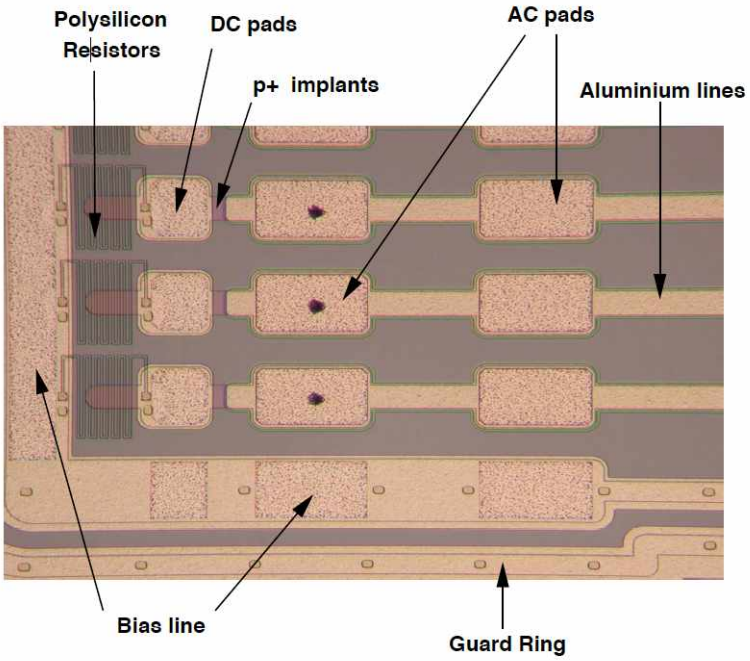

Figure 2.18: Top view of the different elements of a silicon microstrip detector [54]. The black spots on the AC pads are the marks left by the probecard during the test.

2.5.3 The spatial resolution

Microstrip detectors allow to compute the particle hit position. This capability is defined through a parameter called *spatial resolution* that is the rms distance of the measured coordinate from the true hit position; it depends on two categories of effects [47]:

- *physical processes* such as the statistical fluctuations of the energy loss and the diffusion of the charge carriers;
- *external parameters* such as the strip pitch, the (digital or analog) readout method and the signal to noise ratio.

In the following sections these contributions will be treated in detail.

2.5.3.1 Statistical fluctuations of the energy loss

Silicon position sensitive detectors are thin (250-500 μm) and absorb only a small fraction of the total energy of the particle [55]. The dE/dx energy loss follows a Landau distribution, an asymmetric probability function with a long "tail" towards large energy deposits. Figure 2.19 presents an example of a Landau as measured by a 300 μm thick silicon detector; the most probable and mean values are indicated. These two quantities may be used to parametrize the distribution, as presented in the next chapter (section 3.2.4). A MIP generates a most probable number of electron-hole pairs in silicon of 76/μm while the average one is 108/μm. The long tail in the energy loss distribution is due to δ-electrons which are characterized by a large energy transfer in a single collision. δ-electrons in fact have a high energy (keV) and are produced by rare, hard collisions between the incident particle and the electrons of the detector material.

Figure 2.20 shows that the probability[9] to produce a δ-electron is small, although its range can be quite large. δ-electrons in fact have a long track length in the detector material and may produce electron-hole pairs along the track. This causes a displacement of the measured track: if for instance 20000 electrons are released around the track and a 50 keV electron is produced, this electron may drift perpendicularly to the track. Its range is about 16 μm and almost 14000 electrons are created along its path; assuming that its charge is produced 8 μm away from the particle track the displacement Δx is:

$$\Delta x = \frac{N_\delta \cdot \frac{r_\delta}{2}}{N_\delta + N_p} = \frac{14000 \cdot 8}{34000} \; = \; 3.3 \; \mu\mathrm{m} \tag{2.25}$$

[9]For a 280 μm thick microstrip detector the probability of emission of an electron with an energy larger than 50 keV is 11%.

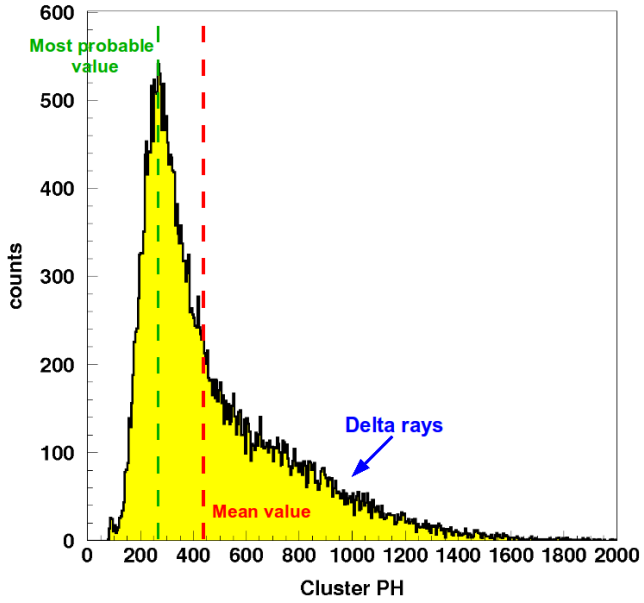

Figure 2.19: The pulse height in arbitrary units for tracks crossing a 300 μm thick single side silicon strip detector (chapter 3).

where r_δ is the average range of the δ-ray, N_δ the number of electron-hole pairs from the δ-ray and N_p the number of electron-hole pairs from the primary track.

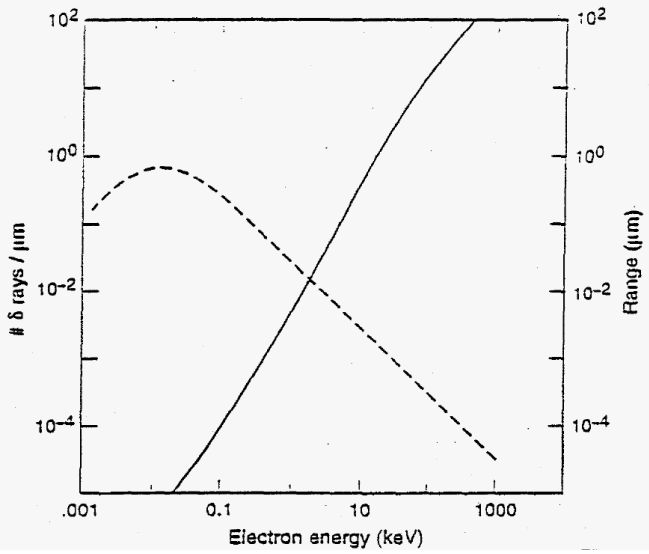

Figure 2.20: Number of δ electrons per micron (dashed line) and their range (solid line) in silicon as a function of their energy [46].

2.5.3.2 Drift and diffusion

Ionizing radiation crossing a semiconductor detector creates electron-hole pairs which are mainly confined in a cylinder with a radius of about 0.5 μm around the track. The produced charge is subject to two different effects: the drift and the diffusion (figure 2.21). The first effect is due to the electric field $\mathcal{E}$. The drift

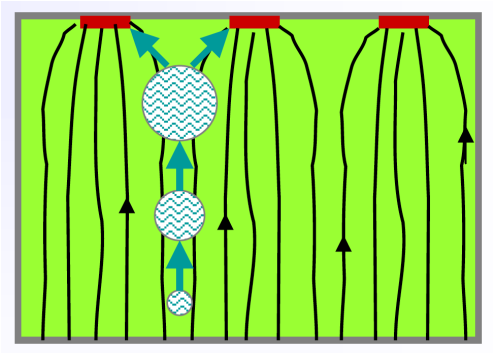

Figure 2.21: Representation of the drift and diffusion processes.

times[10], t_e and t_h, for electrons and holes are:

$$t_{e,h} = \frac{d}{v_{e,h}} = \frac{d}{\mu_{e,h}\mathcal{E}} \tag{2.26}$$

where d is the detector thickness, $v_{e,h}$ and $\mu_{e,h}$ the drift speed and the mobility of the electrons and holes.

Considering typical values such as d = 300 μm, μ_e = 1350 $\frac{\text{cm}^2}{\text{Vs}}$, μ_h = 450 $\frac{\text{cm}^2}{\text{Vs}}$ and the mean electric field $|<\mathcal{E}>|$ = 2.5 $\frac{\text{kV}}{\text{cm}}$ (DELPHI) or $|<\mathcal{E}>|$ = 15 $\frac{\text{kV}}{\text{cm}}$ (CMS), the resulting drift times are t_e = 9 ns, t_h = 27 ns for DELPHI and t_e = 1.5 ns, t_h = 4.5 ns for CMS. Silicon detectors are therefore very fast devices, ideal for high rate experiments with the possibility of being used in the trigger system.

During the drift, electrons and holes diffuse because of multiple collisions with a distribution which follows a Gaussian law:

$$\frac{dN}{N} = \frac{1}{\sqrt{4\pi Dt}} e^{-\frac{x^2}{4Dt}} dx \tag{2.27}$$

where $\frac{dN}{N}$ represents the fraction of charge in the element dx at a distance x from the origin after a time t. The diffusion coefficient D is related to the mobility μ (and to the temperature T) via the Einstein relation:

$$D = \frac{kT}{q}\mu \tag{2.28}$$

[10]The drift time is the time taken by the created charges to reach the electrodes.

The rms of the charge distribution is given by:

$$\sigma = \sqrt{2Dt} \tag{2.29}$$

The charge diffusion, which in practice is the smearing of the charge cloud, represents another limiting factor in the hit resolution. This value was about 6 μm in the LEP silicon detectors running at room temperature [56], and is less than 1 μm in the CMS experiment operating at T = -20°C [57].

2.5.3.3 Strip pitch and readout method

The main external parameter that determines the spatial resolution of a microstrip detector is its readout pitch p. Following the example of the signal detection in gaseous detectors, an essential request is to have a very dense readout in order to measure the signal on several strips and reconstruct the shape of the charge distribution to find the centre. In gaseous detectors however, the amplification of the deposited charge makes the signal to noise ratio so large that even if the signal is spread over many detection elements, the individual signals are larger than the noise. By contrast in silicon detectors there is no multiplication of the charge and therefore the signal spreading over many strips would result in a loss of resolution. Furthermore, since the FWHM of the charge distribution is of the order of 10 μm, the pitch should be of the order of a few micrometers which is not feasible because of mechanical constraints and of the interface to the electronics.

For tracks crossing the detector perpendicularly to it or with a small incident angle, most of the charge is collected by one or two strips at maximum, while for inclined tracks the charge spreads over several strips. The average number of strips in a *cluster*[11] is given by the geometry (figure 2.22) and it is equal to [58]:

$$< N_{cluster} >= \frac{\text{sagitta}}{p} = \frac{d}{p}\tan\theta \tag{2.30}$$

where d is the detector thickness; the sagitta is defined as the projection of the track on the detector plane perpendicular to the strips.

For readout pitches of 20 μm it is expected that in most of the events the charge is collected by a cluster composed of one strip as illustrated in figure 2.23(a). In this case the residual distribution, defined as the difference between the measured hit position and the expected one, has a "top hat" shape, as shown in figure 2.23(b). If the digital mode of operation is used, only the binary information is recorded: the strip is considered if it is above a given threshold. In this case, for tracks

[11] A cluster represents the group of contiguous strips collecting the charge generated by one particle.

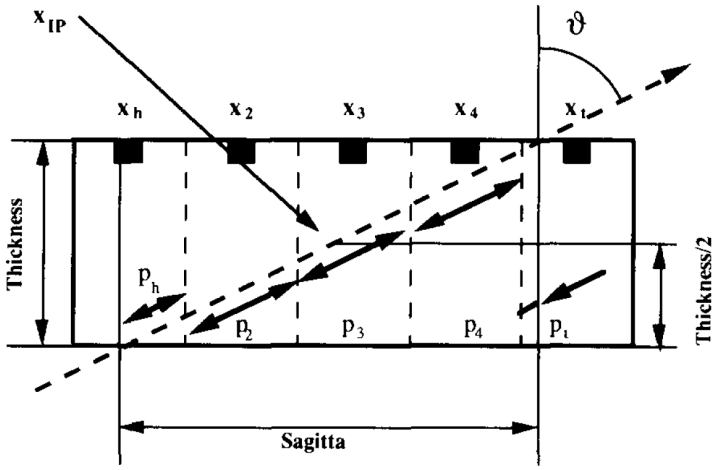

Figure 2.22: The geometry of a silicon microstrip detector used to calculate the average number of strips per cluster. The impact point x_{IP} indicates the point where the particle crosses the mid-plane of the detector. The sagitta is the projection of the track along the coordinate measured by the strips; x_i indicates the position of the ith strip and p_i is the length of the part of the track that crosses the volume of the ith strip [58].

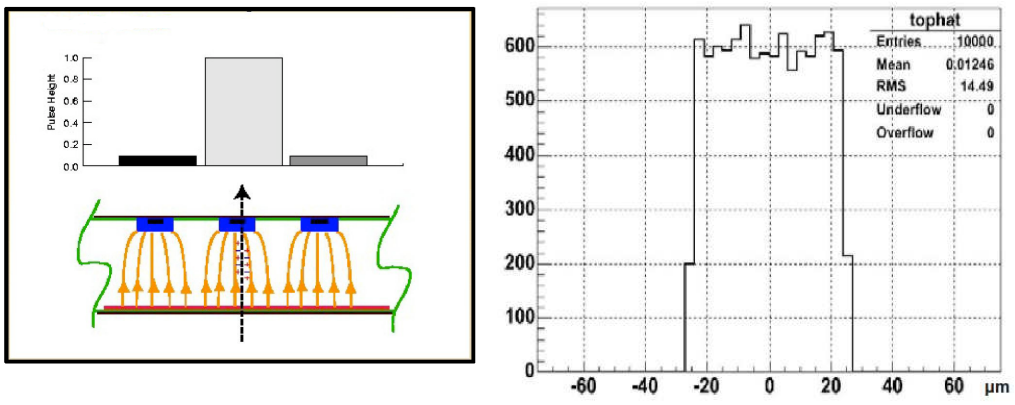

(a) (b)

Figure 2.23: a) A cluster composed of one strip and b) its "top hat" residual distribution [59].

randomly aligned with respect to a strip and thus a residual as the one in figure 2.23(b), the rms resolution is given by:

$$\sigma_{DIG} = \frac{p}{\sqrt{12}} \tag{2.31}$$

For events with a cluster composed of two strips and an analog readout, that is a readout registering the charge detected by each strip (figure 2.24(a)), the position can be measured more precisely by calculating the Center Of Gravity (COG) [60] or using an algorithm which takes into account the effective shape of the charge distribution[12] [58]. In this way the resolution gets better and the residual distri-

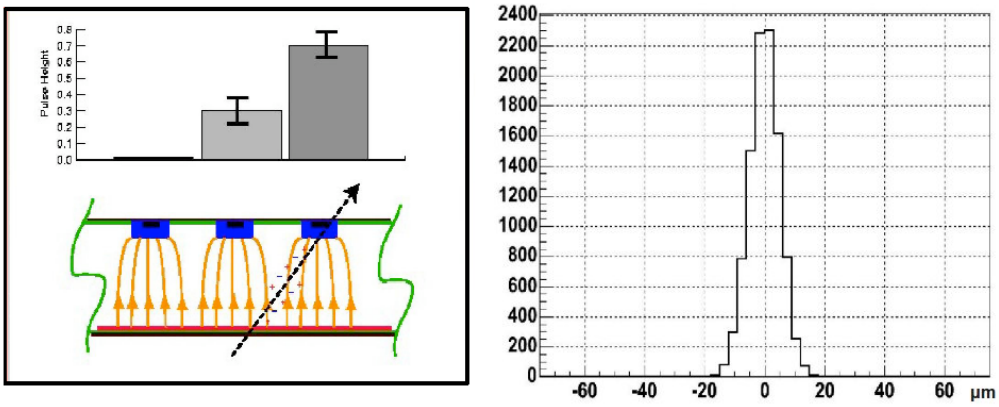

(a) (b)

Figure 2.24: a) A cluster composed of two strips and b) its Gaussian residual distribution [59].

bution has a Gaussian shape (figure 2.24(b)). The center of gravity method is based on the fact that the charge produced between two implanted strips is linearly divided among them and thus the position X of the reconstructed hit can be computed in the following way:

$$X = \frac{\sum_i PH_i \cdot x_i}{\sum\limits_i PH_i} \tag{2.32}$$

where x_i is the position of the i*th* strip of the cluster and PH_i the signal collected by that strip; the sum runs over all the strips which compose the cluster. In this case the spatial resolution depends on the signal to noise ratio SNR [58]:

$$\sigma_{COG} \propto \frac{p}{SNR} \tag{2.33}$$

[12] In this thesis work the *eta algorithm* is used, as presented in chapter 4.

Therefore the larger the SNR the better the spatial resolution. If for instance a sensor with a pitch of 25 μm has a SNR of 50, its position resolution is of the order of 2 μm. If however, because of mechanical constraints or of the electronics cost, the readout density is reduced to 100 μm or 200 μm, the number of events with a cluster composed by more than one strip is very small. In this case the localization accuracy is of the order of 30-60 μm.

A possible solution to improve the resolution without reducing the physical strip pitch is the so-called "floating strip" method, in which one or more strips are implanted between the readout ones [61] (figure 2.25). When the particle crosses a floating strip, the signal is seen by the two nearby readout ones, because of the capacitive coupling between the strips. Depending on the hit position in the floating strip, the two readout strips signals will have a different pulse height, allowing to improve the resolution with the COG method. This configuration allows to reduce

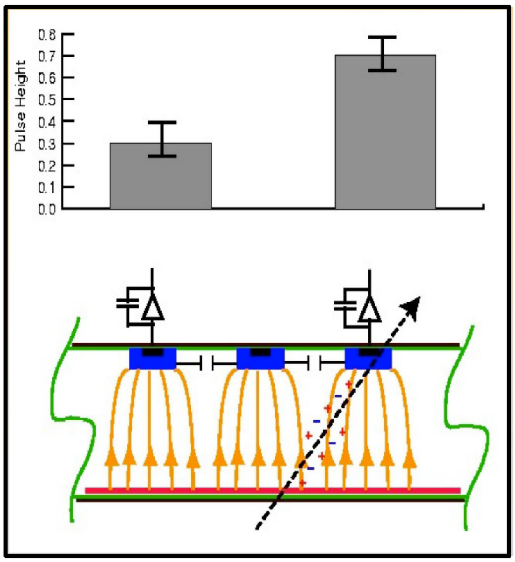

Figure 2.25: The floating strip readout method; the floating strip is located between two readout strips [59].

the number of readout channels maintaining a good spatial resolution. Consider for instance a detector with a physical and a readout pitch of 60 μm and a charge distribution of 20 μm. If the tracks are uniformly distributed, approximately 33% of the events will generate signals on two strips and 66% on one. The average resolution thus is σ = 8.4 μm. If two floating strips are introduced between two readout strips, the physical pitch becomes 20 μm with a readout one of 60 μm: only 33% of the events will be detected by one strip and 66% by two strips. In this way the spatial resolution becomes σ = 3.4 μm [47].
Figure 2.26 presents the case of a very large pitch detector, the AGILE (Astroriv-

elatore Gamma a Immagini LEggero) silicon tracker. The figure shows the pulse height as a function of the hit position in the strip itself [62]: 0 and 242 μm are the centers of two nearby readout strips, 121 μm is the center of the floating one. When the particle crosses the center of the floating strip, the overall collected charge, which is the sum of the charges detected by the two adjacent readout strips, is 76% of the total charge [62].

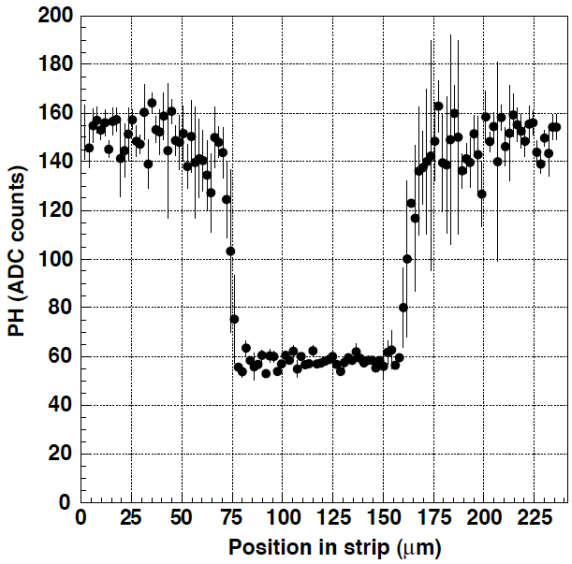

Figure 2.26: Signal pulse height for the AGILE detector as a function of the hit position in the strip: 0 and 242 μm are the centers of two nearby readout strips, while 121 μm is the center of the floating one [62].

2.5.3.4 Noise contribution

The most probable charge deposited in a 280 μm thick silicon detector is about $2{\cdot}10^4$ electron-hole pairs and there is no intrinsic multiplication [47]; therefore if the charge is divided among too many strips (three or more), signals are small and can get lost in the noise distribution. The signal spreading over multiple strips could thus lead to a loss of resolution. Noise is generally expressed in terms of the equivalent noise charge (ENC), defined as the ratio between the noise rms at the shaper output and the amplitude of the signal generated by one electron [63]. Figure 2.27 schematically represents the most important noise contributions of a silicon detector, which are:

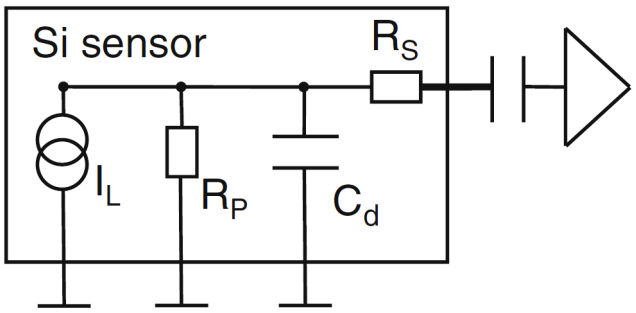

Figure 2.27: The equivalent circuit of a silicon detector together with its amplifier.

- the leakage current I_L. The equivalent noise for a CR-RC filter is given by:

$$\mathrm{ENC_{leak}} = \frac{e}{q}\sqrt{\frac{qI_L t_p}{4}} \tag{2.34}$$

  where e =2.718 is the Euler number, q is the electron charge and t_p is the peaking time, that is the integration time of the shaper;

- the detector capacitance C_d at the input of the charge sensitive amplifier, which is usually the dominant noise source in the detector system. This term can be written as:

$$\mathrm{ENC_{ele}} = A + B \cdot C_d \tag{2.35}$$

  The A and B parameters depend on the amplifier design;

- the parallel (bias) resistor R_P. The noise term can be written as:

$$\mathrm{ENC_{R_P}} = \frac{e}{q}\sqrt{\frac{t_p kT}{2R_P}} \tag{2.36}$$

  where k is the Boltzman constant and T the absolute temperature in K. To achieve low noise the bias resistor should be large. This value is limited by the production process and the voltage drop across the resistor (which is large in irradiated detectors);

- the series resistor R_S, which is given by the resistance of the connection between the strips and the amplifier input (e.g. the aluminum readout lines). It can be written as:

$$\mathrm{ENC_{R_S}} = C_d \frac{e}{q}\sqrt{\frac{kTR_S}{6t_p}} \tag{2.37}$$

  This noise contribution gets smaller if the shaper has a long peaking time.

The total noise is the quadratic sum of all the contributions:

$$\mathrm{ENC} = \sqrt{\mathrm{ENC}_{\mathrm{ele}}^2 + \mathrm{ENC}_{\mathrm{leak}}^2 + \mathrm{ENC}_{\mathrm{R_P}}^2 + \mathrm{ENC}_{\mathrm{R_S}}^2} \tag{2.38}$$

To achieve a large signal to noise ratio in a silicon detector system, in principle the following design criteria should be satisfied:

- low detector capacitance;
- low leakage current;
- large bias resistor;
- low series resistor;
- long integration time.

The optimal design of a detector and its frontend electronics depends on the application. For example at the LHC experiment, where the shaping time has to be extremely short (the bunch crossing occurs every 22 ns), the noise is mainly due to the $\mathrm{ENC}_{\mathrm{ele}}$ term. Table 2.2 presents the noise contributions and peaking values for the DELPHI and CMS silicon detectors.

Detector	t_p dependence	DELPHI MVD	CMS tracker
T_p		1.8 μs	50 ns
T		20°C	-10°C
C_d		9 pF	18 pF
$\mathrm{ENC}_{\mathrm{ele}}$	$\sim \frac{1}{t_p}$	520 e^-	711 e^-
$\mathrm{ENC}_{\mathrm{leak}}$	$\sim \sqrt{t_p}$	78 e^-	24 e^-
R_P		36 MΩ	1.5 MΩ
$\mathrm{ENC}_{\mathrm{R_P}}$	$\sim \sqrt{t_p}$	169 e^-	131 e^-
R_S		25 Ω	50 Ω
$\mathrm{ENC}_{\mathrm{R_S}}$	$\sim \sqrt{\frac{1}{t_p}}$	13 e^-	230 e^-
total ENC		552 e^-	760 e^-

Table 2.2: Different noise contributions for a DELPHI and CMS silicon strip detector [4]. In the quadratic sum the $\mathrm{ENC}_{\mathrm{ele}}$ term is the most significant.

2.5.4 The electronics for microstrip detectors

Silicon detectors do not have an intrinsic multiplication of the charge as gas detectors. This means that a dedicated low noise electronics is needed to treat the signal. The radiation released in the detector has to be converted into an electrical signal which is then amplified, shaped and digitized. The first element of the electronics chain is usually indicated as frontend electronics and consists of dedicated ASICs (Application Specific Integrated Circuits) able to perform several of the tasks listed above. The ASICs are the last step of a huge development of the electronics in these last 50 years, that has moved the technology from discrete components to hybrid systems and then to the complete integration on a very large scale (VLSI - Very Large Scale Integration) on a silicon substrate. The passage to VLSI has happened in 20 years: from the bipolar technology of the 1960s to the large scale of integration in the 1970s (LSI - Large Scale Integration) with the MOS (Metal Oxide Semiconductor) transistors and to VLSI in the 1980s with the CMOS (Complementary MOS) technology. The present ASICs are compact devices with an area of a few tens of mm^2 for a number of channels ranging from 32 to 128.

The block diagram of a typical ASIC channel for silicon detectors consists of three main components (figure 2.28):

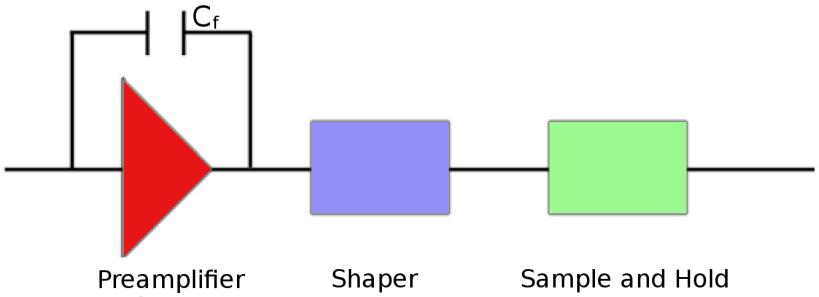

Figure 2.28: The three main components of each ASIC channel.

1. **the preamplifier**. The signal of a MIP in a 300 μm thick silicon detector is 4 fC, which is in fact quite small. Given the collection time is small (<30 ns), the signal can be represented as a current δ pulse whose integral Q is the total charge. This charge is integrated on the feedback capacitor C_f using a charge sensitive amplifier (CSA) [64] producing a voltage step with an amplitude $-\frac{Q}{C_f}$. The CSA is usually chosen because of its low noise characteristics and its gain independence from the detector features. The reset of the CSA can be performed with a digital signal (which is usually avoided because of the low noise requirement) or placing a resistor R_f in

parallel with C_f. The R_f value should be large enough to keep the noise under control and at the same time small enough to allow the ASIC to work with a fast input rate;

2. **the pulse shaper**. The preamplifier output signal is sent to a filter which has to filter the noise and to shape the signal. There are two types of filtering: the time variant and the time invariant one. In the first case, the circuit network is modified during its operation. This is the category of circuits where the integration stage is activated by the presence of a gate signal, with the signal shaping that precedes or follows the gate. This kind of filter is usually implemented with capacitors and switches controlled by digital signals [65], as in the MX-family where two capacitors are employed to integrate respectively the background and the signal (double correlated sampler). In the time invariant case (which is the one used in the electronics of this thesis work), the circuit network is fixed; a typical example is the CR-RC^n shaper consisting of a differentiator followed by n integrators. The output shape is a semi-Gaussian one; these filters belong to the time continuous filtering category, given the shaper is always active;

3. **the sample and hold**. The output of the shaper is usually stored in a capacitor to be readout afterwards. The capacitor stores the signal when a dedicated digital signal is active (hold signal). This is the third block for the analog readout. If a digital output is foreseen, usually each channel has a discriminator which is fed with the shaper output.

The analog output of the ASIC is usually a multiplexed one which is digitized by an external ADC (Analog to Digital Converter), even if ASICs have been developed with analog pipelines (APV-25[13]) or with a sparse readout (VATAGP2.5[14]).

The ASIC used in this thesis work belongs to the VA and VATA family of Gamma Medica - IDEAS[15]. The layout of a VA channel is described in section 3.1.2; in the VATA case, each channel features also a fast shaper whose output is fed to a discriminator for the digital output. These ASICs are optimized for input capacitances ranging from 10 to 100 pF and are characterized by low noise (depending on the ASIC, it can be of the order of 30 e^- ENC) and good speed (the shaping time is of the order of a few hundreds of nanoseconds and can be made longer to increase the SNR). The details of the ASIC used in this work will be described in chapter 3.

[13] http://www.meanwell.com/search/APV-25/APV-25-spec.pdf
[14] http://www.gammamedica.com/ind_asic_products.html
[15] http://www.gm-ideas.com

2.6 An application example: bent crystal physics

As already stated, silicon detectors have become a must whenever tracking with a low material budget and high precision is needed. This section presents the improvements that the use of the INSULAB silicon telescope has allowed in the field of bent crystal physics. Bent crystals are devices able to deflect relativistic charged particles, producing the same effects of a huge magnetic field, thanks to the coherent interaction of particles with the ordered crystalline structure. Bent crystals have a great potentiality for many physics applications, such as beam collimation, beam steering, photon production; a complete discussion of the bent crystals theory and their applications can be found in [66]-[67].

Crystals are characterized by an ordered and symmetrical arrangement of the atoms. The crystal spatial structure, that is called *lattice*, consists of a grid of straight lines (which represent the interatomic bonds) and vertices (corresponding to the single atoms in the simplest case) as shown in figure 2.29. The primitive cell of the lattice is a parallelepiped which is characterized by the distance between the vertices in three dimensions and the angles among bonds [67]. A particle going

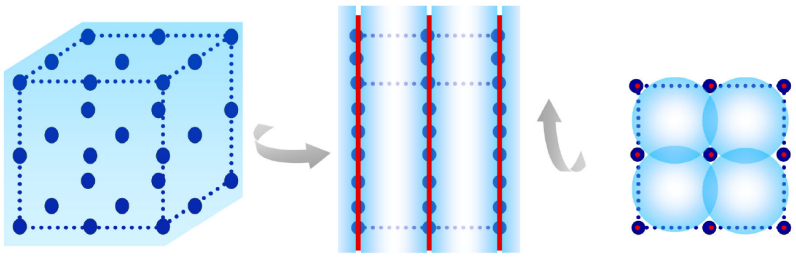

Figure 2.29: A regular crystalline structure; the atoms appear: in a non-ordered structure (left); arranged in planes, after a rotation around an axis (center); arranged in strings after a rotation around the orthogonal axis (right) [68].

through an amorphous material or a misaligned crystal experiences uncorrelated collisions with the single atoms through a variety of processes depending on the different impact parameters; among them, angular scattering with nuclei and energy loss with atomic electrons are the most common. However, the intrinsic crystal structure allows to reduce these effects.

The idea that certain directions in a crystal could be more transparent to the passage of charged particles than in an amorphous material was first suggested by Stark [69] in 1912; he realized that the motion of a charged particle which enters a crystal at a small angle with respect to the crystal lattice direction can be confined in crystal regions called *channels*. These regions are characterized by a low nuclear and electronic density so that the energy loss of a particle which is crossing

them is reduced [66]. His hypothesis was confirmed by several simulations and experiments in the early 1960s, when the channeling effect was discovered using ions.

In 1964, the theoretical explanation of the channeling effect was formulated by Lindhard [70] who demonstrated that when a charged particle impinges on the crystal with a small impact parameter with respect to the crystallographic axis, a number of correlated collisions with the crystal lattice atoms occurs. The potential of each atom in fact could be replaced with an average continuous potential in the approximation of a small incoming angle with respect to the atomic planes as shown in figure 2.30. The particle is trapped in the channel if its transversal

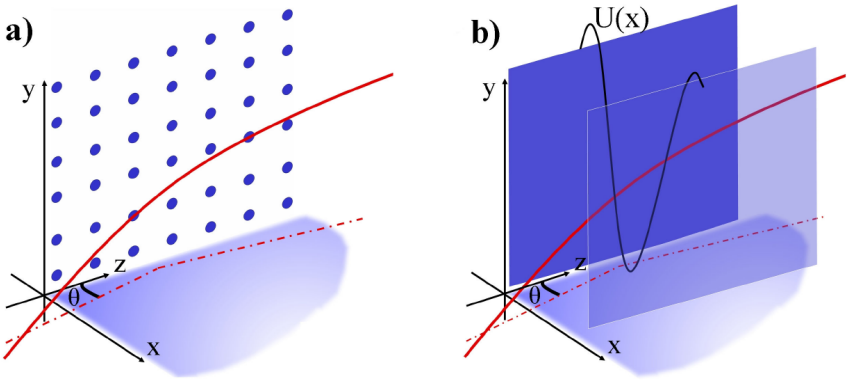

Figure 2.30: A particle (red line) moving in a crystal misaligned with respect to the axis but at a small angle with respect to the crystalline plane (z-y plane). b) The particle experiences an average potential due to the planes, represented by the black line [66].

energy E_t is smaller than the maximum value of the potential barrier U_{max} that is $E_t < U_{max}$. The alignment condition is defined by the critical channeling angle θ_C (the maximum angle available for channeling):

$$\theta_C = \sqrt{\frac{2U_{max}}{pv}} \tag{2.39}$$

where p is the momentum and v the velocity of the particle. For a silicon crystal U_{max} is about 20 eV thus θ_C is 9.42 μrad at 450 GeV.

Starting from the motion of a particle confined in a channel of a straight crystal, in 1976 Tsyganov [71] suggested the idea to steer a high energy particle beam using a bent crystal. The bending of the crystallographic planes in fact produces a curved channel which is able to deflect the channeled particles. A curved channel can be obtained from a straight one bending a crystal with a mechanical holder.

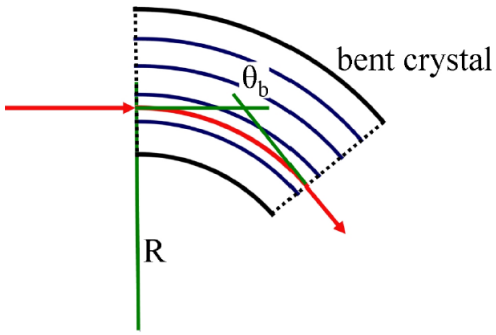

Figure 2.31: The bent crystal working principle [68].

Figure 2.31 shows the scheme of a bent crystal. The red line represents the particle trajectory which is deviated of the angle:

$$\theta_b = \frac{L}{R} \tag{2.40}$$

where R is the curvature radius of the crystal and L its length along the beam. The first confirmation of Tsyganov's idea was obtained by pioneering experiments at Fermilab and Dubna [72].

However it can happen that the multiple scattering in the channel increases the transverse momentum and the particle can overcome the potential barrier and exit the channel (the so-called *dechanneling effect*). In this case a reverse mechanism could be foreseen: a particle which enters the crystal, misaligned with respect to the crystallographic plane (thus with a high transverse momentum), can lose energy because of the multiple scattering and can be captured in a channel; this phenomenon is called *volume capture*. This latter occurs for impact angles larger than the critical one as long as the impact angle stays smaller than the bending one ($\theta < \theta_b$).

In 1987 a new phenomenon was discovered in computer simulations [73]: the *volume reflection*. It describes the particle deviation in a single tangency point inside the crystal due to an elastic scattering with the atomic potential barrier. It can be demonstrated that in this case the total angular kick is:

$$\theta_r = 2\theta_C \tag{2.41}$$

Figure 2.32 summarizes the different deflection effects that can occur in a bent crystal.

The first volume reflection observation was performed at the IHEP (Institute for High Energy Physics) laboratory in Protvino (Russia) on the U-70 accelerator

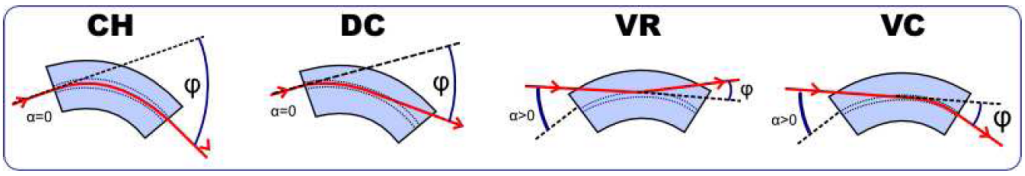

Figure 2.32: Schematic description of the different deflection effects in a bent crystal: channeling (CH), dechanneling (DC), volume reflection (VR) and volume capture (VC) [68].

with a 70 GeV/c proton beam [74]. A silicon crystal was prepared and bent using the elastic quasimosaicity effect which allows to reach a very small thickness in the beam direction; the crystal was 0.72 mm (along the beam) with an area of 20×60 mm^2; the bending angle was 423 μrad. In this condition, if the crystal is properly oriented, the volume reflection should overcome both the beam spread and the multiple scattering of the crystal being easily detectable. Figure 2.33 shows the experimental setup essentially characterized by integration detectors (emulsion films) and beam monitors. The beam profile after the crystal was mea-

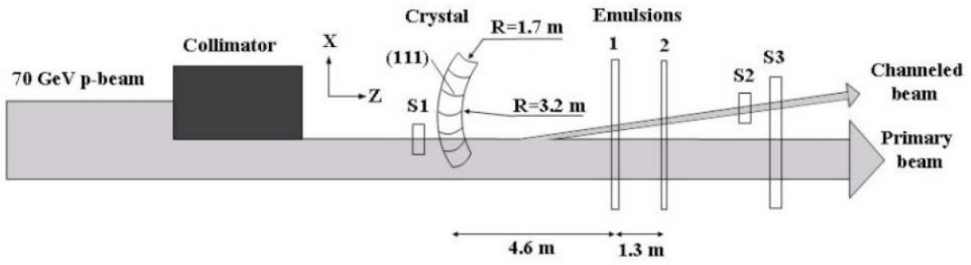

Figure 2.33: The IHEP experimental setup [68].

sured by two emulsion plates. The intensity profile recorded by the first plate is shown in figure 2.34 (left). Three different regions can be identified marked with the letters A (primary beam overlapping the reflected one), B (beam absence), C (channeled beam).

The first very high precision channeling and volume reflection measurements have been performed by the H8RD22 collaboration in 2006 at the CERN SPS H8 line [75] using the INSULAB microstrip silicon telescope, the main topic of this thesis. The experimental layout is presented in figure 2.35; it consists of a set of 50 μm readout pitch double side microstrip silicon modules, a high precision goniometer for the alignment of the crystal with the beam and a pair of plastic scintillators which provide the trigger signal. This tracking system is able to re-

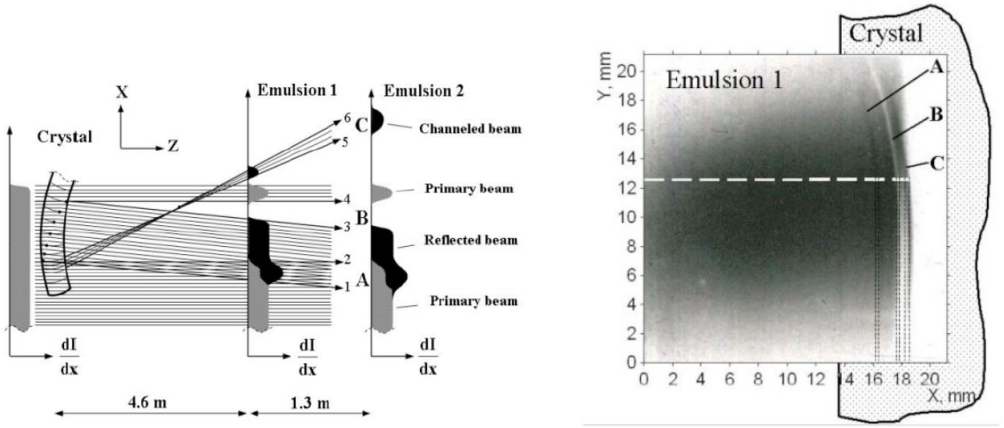

Figure 2.34: Schematic view of the horizontal trajectories crossing the crystal and the emulsion (right); the profile reconstructed with the first emulsion crossed by the beam. Three different regions can be identified: A (primary beam overlapping the reflected one), B (beam absence) and C (channeled beam) (left).

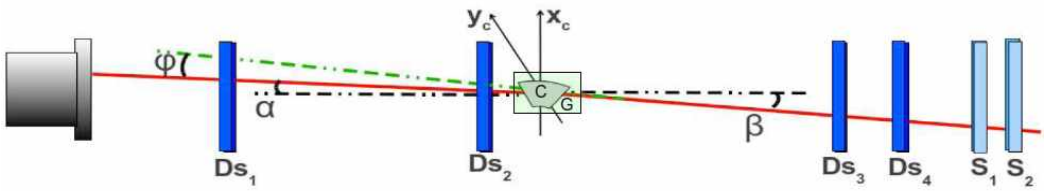

Figure 2.35: The 2006 experimental setup used by the H8RD22 collaboration: a set of 50 μm readout pitch double side microstrip silicon modules (Ds_{1-4}), a high precision goniometer (G) to align the crystal (C) with the beam, a pair of plastic scintillators (S_{1-2}) to generate the trigger signal.

construct both the incoming (α) and the outgoing (β) angle of the particle with respect to the crystal with a spatial precision of 5 μm and an angular resolution of 0.5 μrad. Thanks to this high precision system the different phenomena induced by the bent crystal become clearly distinguishable with respect to the earliest studies (figure 2.34). The typical plot obtained with this new system is presented in figure 2.36 [75].

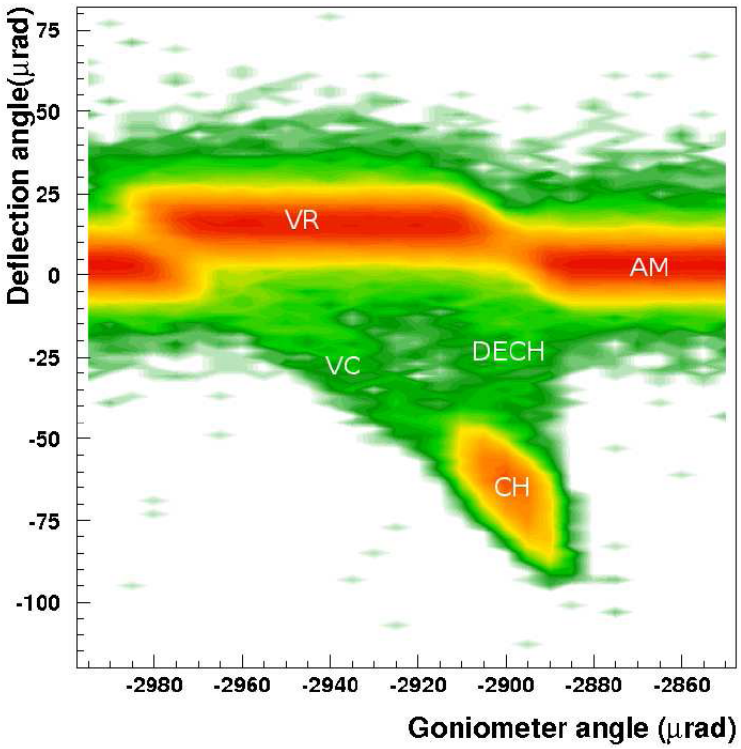

Figure 2.36: The crystal behavior as a function of the angle between the incoming particle and the crystallographic planes (obtained changing the goniometer angular position). The different bent crystal phenomena are indicated; AM indicates that the crystal is in the amorphous position, that is not oriented with respect to the beam [67].

Chapter 3

The INSULAB telescope and its new fast readout system

A tracking system is fundamental to test detectors ranging from calorimeters up to more complex systems (as in the bent crystal physics setup described at the end of chapter 2). Such a system is usually called *telescope* and it consists of a set of silicon microstrip modules with a high spatial resolution of the order of a few microns. The telescope needs to be tested on high intensity high energy beams in order to define its features not being affected by multiple scattering and with a statistics large enough. A fundamental requirement is to have a fast readout system in order to maximize the statistics.
The INSULAB telescope consists of four double side silicon microstrip detectors with a 50 μm readout pitch. To comply with the high rate of the CERN North Area extracted beams, a new readout system has been developed and tested.
This chapter describes the INSULAB telescope modules and its tests with the standard electronics at the Como laboratory and the results obtained with the new readout electronics at the CERN SPS H4 line.

3.1 The INSULAB telescope

The INSULAB telescope consists of several independent elements called *modules*. Each module features one double side silicon detector with its frontend and readout electronics. The standard system taken at the beam has four modules (D1-D4 in the following) with CSEM (Centre Suisse d'Electronique et Microtechnique Neuchatel, Swiss) detectors readout by VA2 ASICs (Gamma Medica - IDEAS[1]). Several new modules have been developed with a different readout ASIC (VA1TA) and different detectors (single side ones by HAMAMATSU and

[1] http://www.gm-ideas.com

double side by FBK-irst). The following sections describe the standard system components.

3.1.1 The silicon detectors

The silicon microstrip detectors used in this thesis work were developed by INFN Trieste and produced by CSEM.
Each module consists of a double side high resistivity 300 μm thick silicon microstrip detector with a sensitive area of 1.92×1.92 cm^2 [76]. The detector p-side (or *junction side*) has a p^+ strip every 25 μm and a readout pitch of 50 μm: a one floating strip scheme is implemented. The n-side (or *ohmic side*) has a n^+ implantation every 50 μm, perpendicular with respect to the p-side strips. Each module has 384 strips on each side. The detectors are fully depleted with a bias voltage in the range of 36-50 V depending on the module and the average leakage current is of the order of 1.5-2.0 nA per strip. Table 3.1 summarizes the features of these detectors.
The readout of each detector side is performed by three 128 channel VA2 ASICs [77]. Each silicon microstrip detector together with the three VA2 readout

Number of strips	384
Bulk thickness	300 μm
Detector dimension	1.92×1.92 cm^2
p-side strip pitch	25 μm
p-side readout pitch	50 μm
n-side strip pitch	50 μm
n-side readout pitch	50 μm
Resistivity	>4 kΩ cm

Table 3.1: General features of the INSULAB telescope silicon detectors.

ASICs and the hybrids (the ceramic boards hosting the ASICs) is assembled on a 12.5×12.5 cm^2 1 cm thick fiberglass frame, as presented in figure 3.1. The strips are capacitively coupled to the input of the amplifier-multiplexer ASICs using custom 128 channel capacitor chips (figure 3.2(a)) built on a quartz substrate. Each capacitor chip channel comprises a 150 pF capacitor and protection diodes against the capacitor breakdown [76].

3.1.2 The VA2 readout ASIC

Three VA2 ASICs are necessary to readout the 384 strips on each side of the module. The three ASICs are glued with conductive epoxy glue (H20E by Epotek)

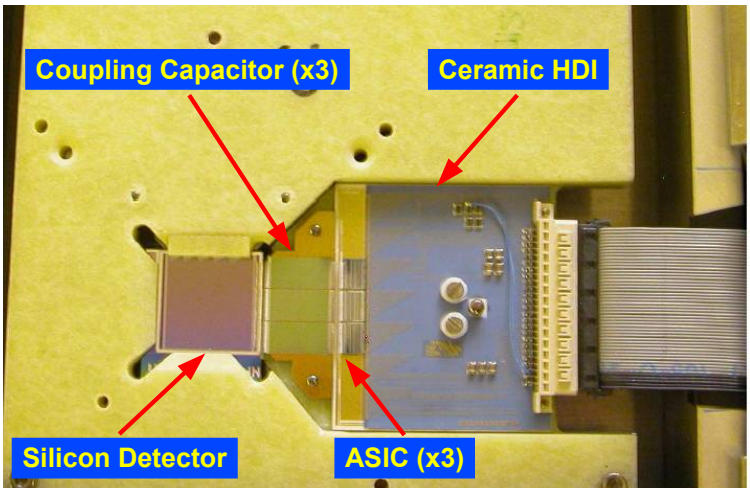

Figure 3.1: The telescope module: the 384 strips of the silicon detector are readout by three VA2 ASICs which amplify and shape the signals.

on ceramic multilayer hybrids (figure 3.1) and their control and output pads are bonded with 17 μm diameter Al wires (figure 3.2(b)).
The VA2 ASIC, presented in figure 3.3, is a 128 channel ASIC built with the 1.2 μm N-well CMOS technology; it has a 40.6 μm input channel pitch matching the detector strip pitch; the input pads in fact are staggered on two rows so that even and odd strips are bonded on the two different rows [77]. Its features are summarized in table 3.2. Each ASIC channel (figure 3.4) consists of:

- a low-noise/low power charge sensitive preamplifier;
- a CR-RC slow shaper;
- a sample and hold circuit.

The VA2 ASIC has several adjustable parameters to properly operate the shaper and the preamplifier and thus to obtain a proper shaping time and gain. The main analog input parameters which can be adjusted are the following (figure 3.5):

- *sha_bias* which sets the biasing current for the shaper and adjusts the shaping time;
- *pre_bias* which sets the biasing current for the preamplifier;
- *vfs* which sets the biasing voltage determining the resistance of the feedback transistor of the shaper;

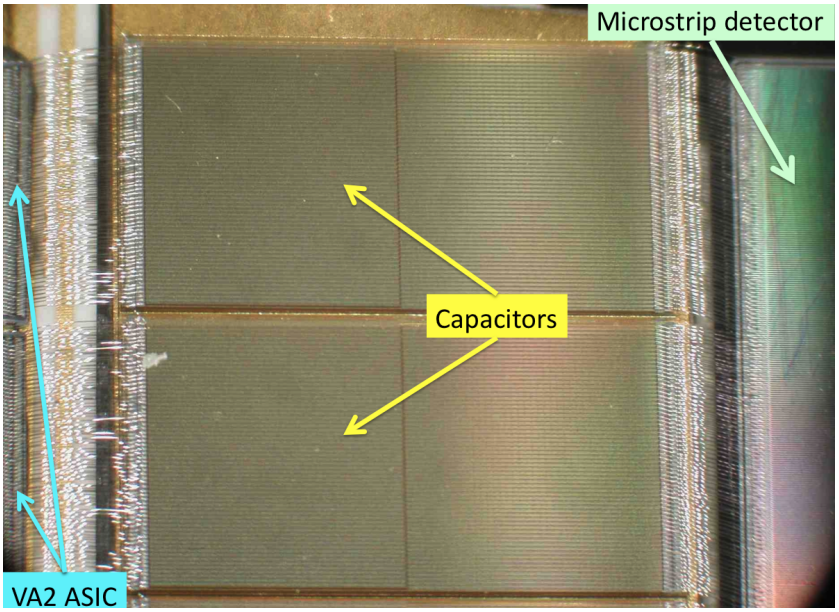

(a)

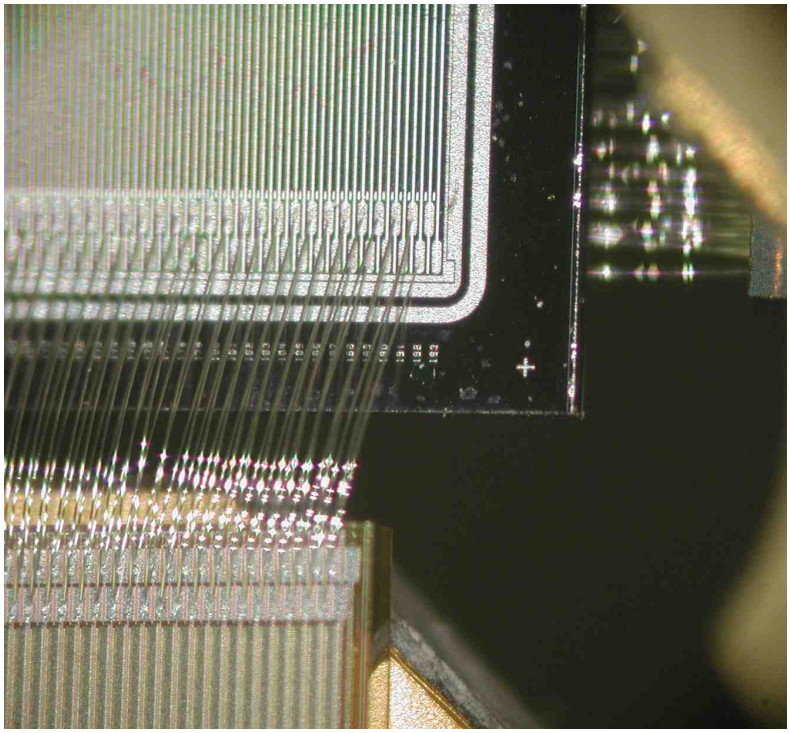

(b)

Figure 3.2: One of the INSULAB telescope modules: a) the capacitors built on a quartz substrate, bonded with the microstrip detector and the ASICs; b) the detail of the Al bonding wires.

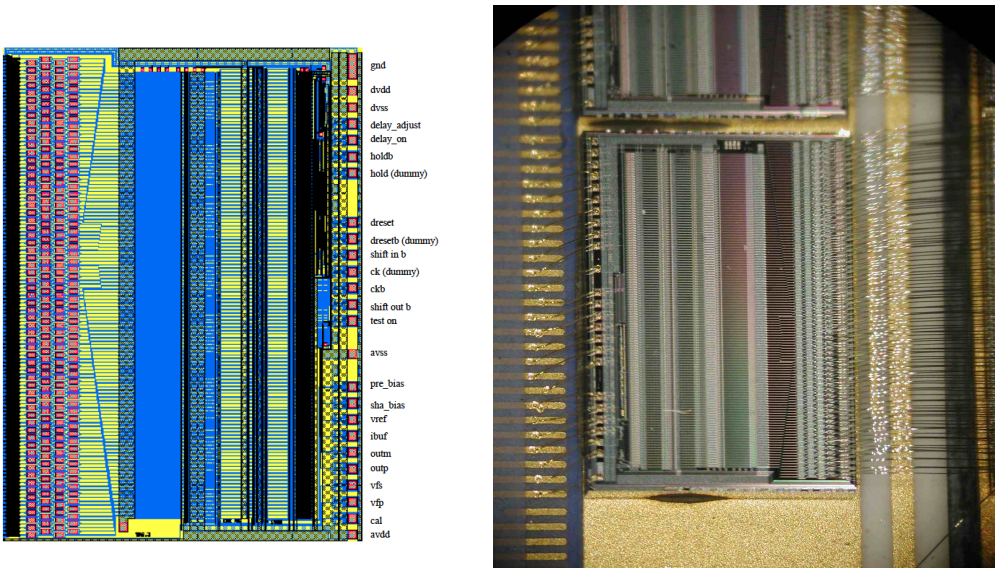

(a) (b)

Figure 3.3: a) The VA2 ASIC layout and b) its top view.

Process	1.2 μm N-well CMOS
Die surface	6.18 mm$\times$4.51 mm
Die thickness	$\sim$600 μm
ENC at 1 μs of peaking time	80 $e^-\pm$15 e^-/pF
Power consumption	170 mW
Shaper peaking time	1-3 μs
Dynamic range	$\pm$4 MIPs
Sha_bias (nominal value)	22 μA
Pre_bias (nominal value)	500 μA
Vfs (nominal value)	700 mV
Vfp	-0.2 V to -0.5 V
Ibuf (nominal value)	140 μA

Table 3.2: Technical features of the VA2 readout ASIC [77].

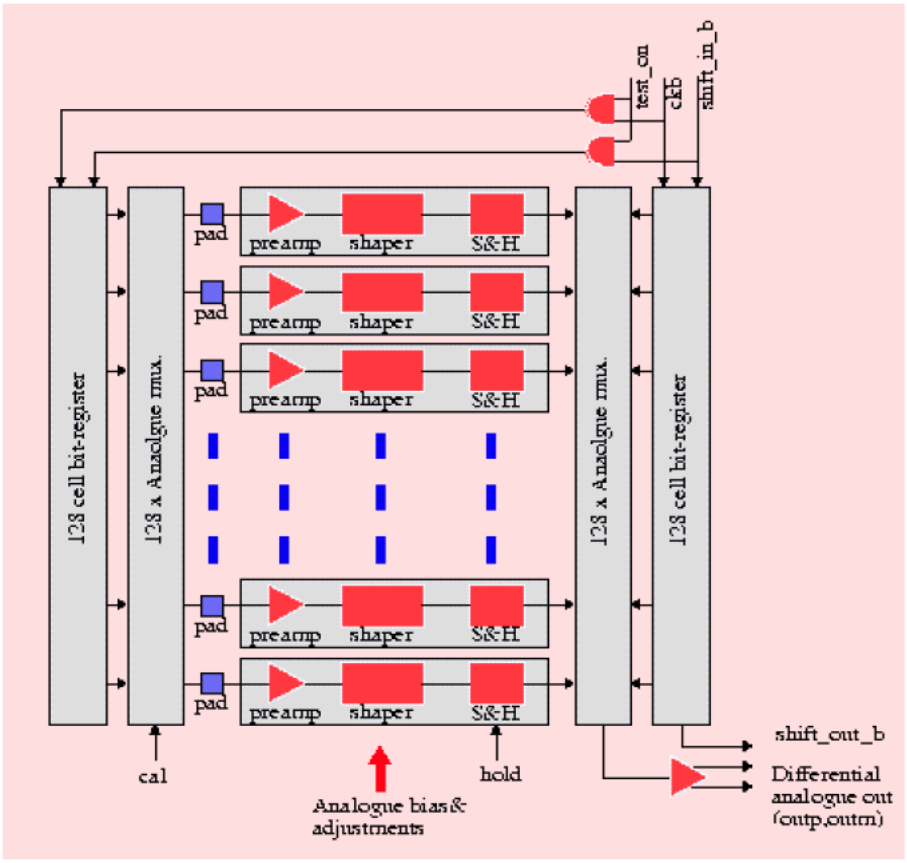

Figure 3.4: The VA2 ASIC architecture; S&H indicates the sample and hold circuit.

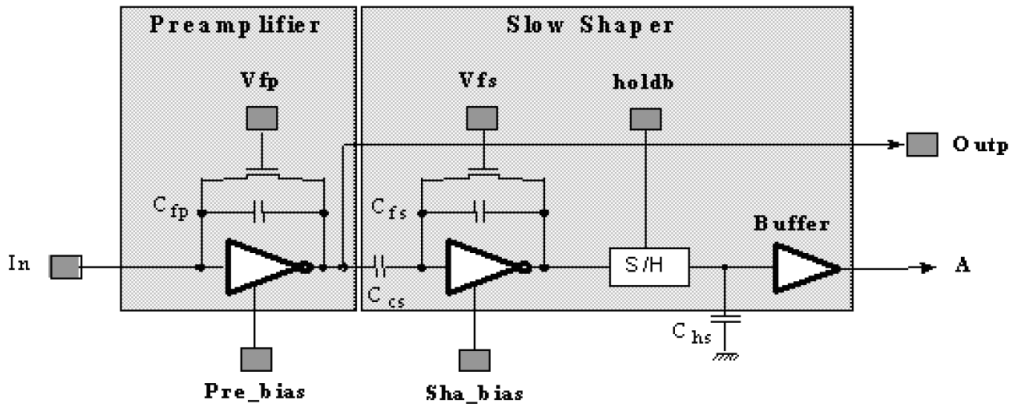

Figure 3.5: The layout of a VA channel; the main analog input setting parameters (sha_bias, pre_bias, vfs and vfp) are indicated.

- *vfp* which sets the biasing voltage determining the resistance of the feedback transistor of the preamplifier.

The analog output information is serialized: thus all the 128 S&H outputs are multiplexed into one output line, with a maximum frequency for the clock of 10 MHz. Figure 3.6 presents the VA readout sequence. The signal corresponding to the particle energy deposit is amplified and shaped and its peak amplitude is sampled by a hold signal, which is generated by the readout electronics at the correct time. Once the signals are held, the correct combination of the shift-in signal and the readout clock starts the multiplexing of the data.
Figure 3.7 shows the shape of the signal for the ohmic and junction side of a single channel; this plot has been obtained by enabling only one channel and by observing its response to a pulse (the calibrate signal). The peaking time for the junction side is ∼1500 ns while for the ohmic one ∼2000 ns; the gain of the two sides depends on the full electronics chain.

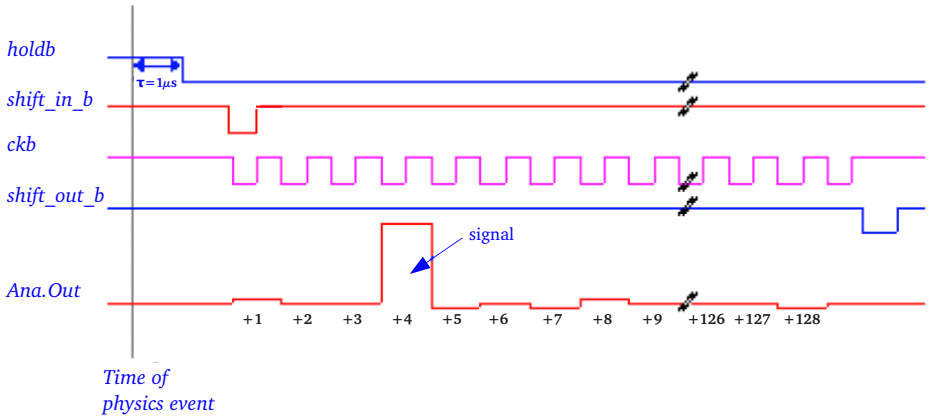

Figure 3.6: The VA readout sequence.

3.1.3 The repeater and the optocoupler boards

The interface between the frontend (the detector and the hybrid with the ASICs) and the readout electronics (section 3.2.1.2) is represented by the repeater boards (figure 3.8), which are 4 layer PCBs (Printed Circuit Boards) with the following tasks:

- they transform the RS422 differential signals to single ended ones as requested by the ASICs; the signals are differential in order to transport them to long distances without being affected by noise;

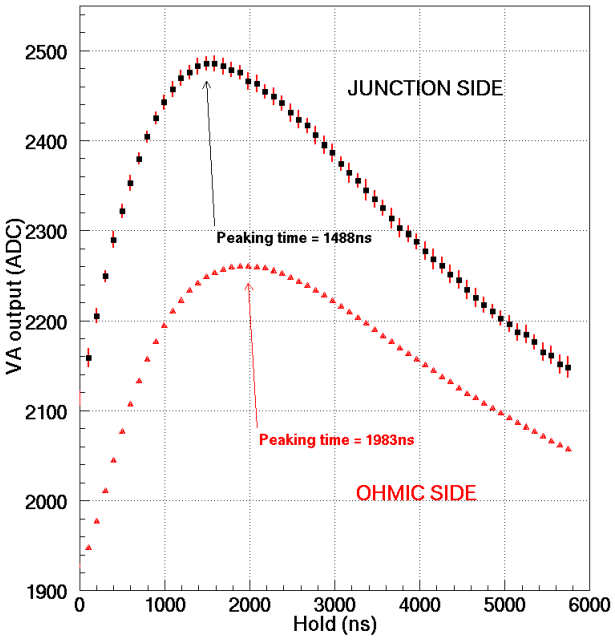

Figure 3.7: The signal shape for the ohmic and junction side of a single channel measured with the calibration input.

- they provide the bias to the detector and the ASICs and the digital signals to the ASICs through 50 pin ERNI cables. The silicon detectors full depletion voltage is in the 36-50 V range while the ASIC power rails are ± 2 V and they are generated by power regulators on the repeaters themselves (starting from ± 6 V). The digital and the analog supplies are filtered separately;

- they amplify the analog output of the hybrid (that is the 384 multiplexed channels of the three ASICs). The output is a differential voltage one (it is converted from current to voltage on the hybrid itself) and is amplified by a NE592[2].

Figure 3.8 presents a photo of the repeater with its main logic blocks. The repeater has been designed to be used with different ASICs, which is the reason of a block dedicated to the choice of the configuration settings. The threshold and trigger block is used with the VATA family to set the threshold for the discriminators and to transform the ASIC trigger output to a TTL (Transistor-Transistor Logic) signal.

The n-side of the silicon detectors has a "zero" level which in fact is not ground (0 V) but the bias voltage (several tens of Volts). There are two possible ways to

[2]ON Semiconductors.

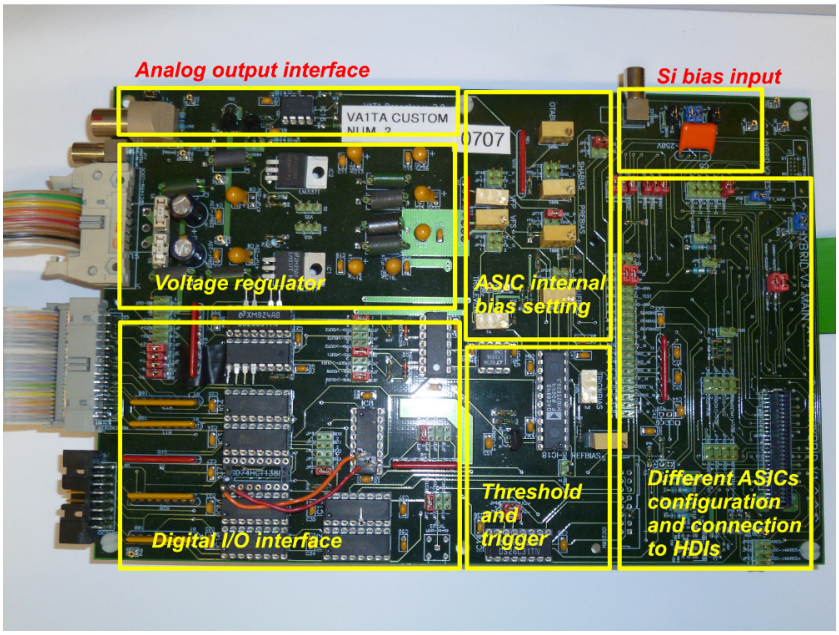

Figure 3.8: The repeater board and its main logic blocks.

deal with the readout of the ohmic side:

- the frontend and the readout electronics are operated as in the junction case (0-5 V). In this case the silicon capacitors have to withstand the drop of the bias voltage across them, given the amplifier input is set at ∼-1V;

- the frontend electronics ground is not set to 0 V but to V_{bias} so that the electronics operates at V_{bias}-(V_{bias}+5 V). In this case no voltage drop is present across the capacitors and the risk of the capacitor breakdown (and thus of pinholes) is much smaller.

The INSULAB telescope uses this second option. Given the ADC and the VME boards, to generate the configuration and readout signals, work with the standard 0-5 V of the junction side, both the analog and digital signals have to be level shifted from and to the module. This task is performed by the optocoupler (figure 3.9) using the ADUM 2400[3] for the digital signals and the HCPL 4562[4] for the analog ones.

[3] Analog Devices.
[4] AVAGO Technologies.

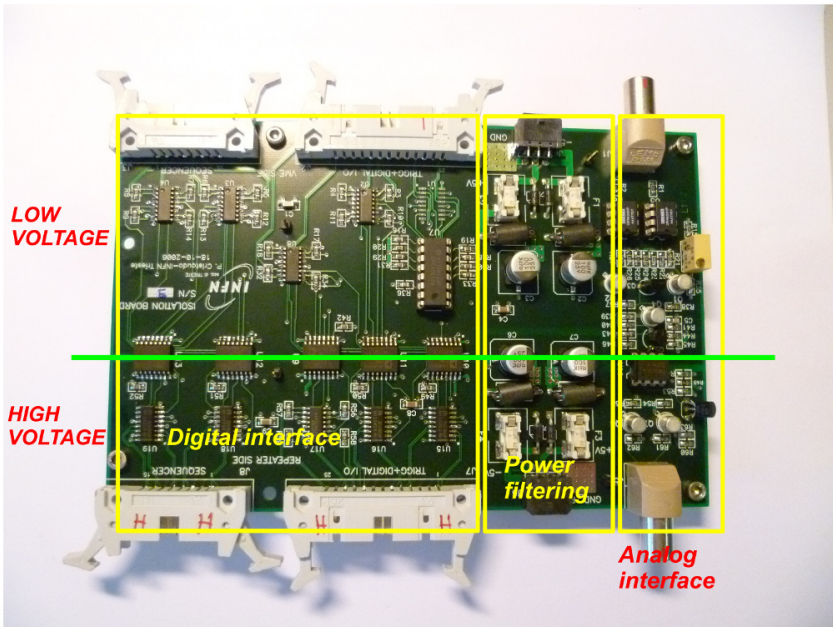

Figure 3.9: The optocoupler board.

3.2 Commissioning tests at the Como laboratory

Several characterization tests have been performed on each silicon microstrip module at Como using a ^{90}Sr β-source and the old readout electronics. This section presents the experimental setup, the readout chain and the results obtained for one of the four modules since the behavior of the other three is similar.

3.2.1 The experimental setup

The experimental setup is shown in figure 3.10. It consists in:

- the ^{90}Sr β-source;
- the silicon microstrip module under test;
- a plastic scintillator (section 3.2.1.1) used for the trigger generation;
- the standard data acquisition system (section 3.2.1.2).

3.2.1.1 The plastic scintillator counter

The plastic scintillator counter consists of a polystyrene tile with an active area of 3×10 cm^2 (figure 3.11). The light produced by the particle interaction is readout

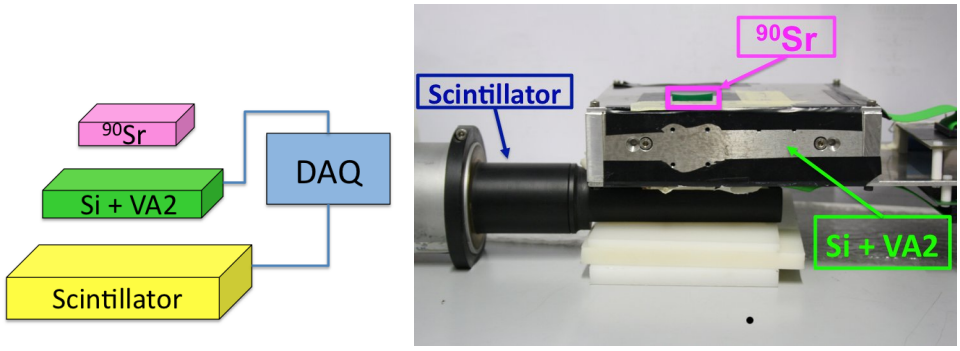

(a) (b)

Figure 3.10: a) A schematic view and b) a photo of the experimental setup with the ^{90}Sr source used to test each silicon microstrip module; the plastic scintillator has been used for the trigger generation.

by a PMT (PhotoMultiplier Tube) directly connected to the scintillator tile. After the particle passage, the trigger signal is sent to the trigger board and then to the VME sequencer which generates the DAQ trigger that starts the readout sequence, as explained in the next section.

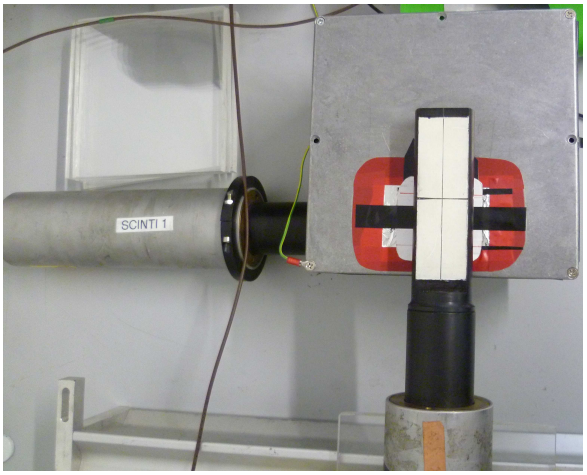

Figure 3.11: The plastic scintillator counters used in this thesis work. The photo refers to the VA1TA tests (appendix A) where the coincidence signal of the two scintillators was used to generate the trigger.

3.2.1.2 The DAQ system

Figure 3.12 presents the DAQ (Data AcQuisition) chain used in the 2012 tests in the laboratory. The system is a VME (Versa Module Eurocard) one controlled by a SBS[5] Bit3 620 board optically linked to a PC running linux. This board al-

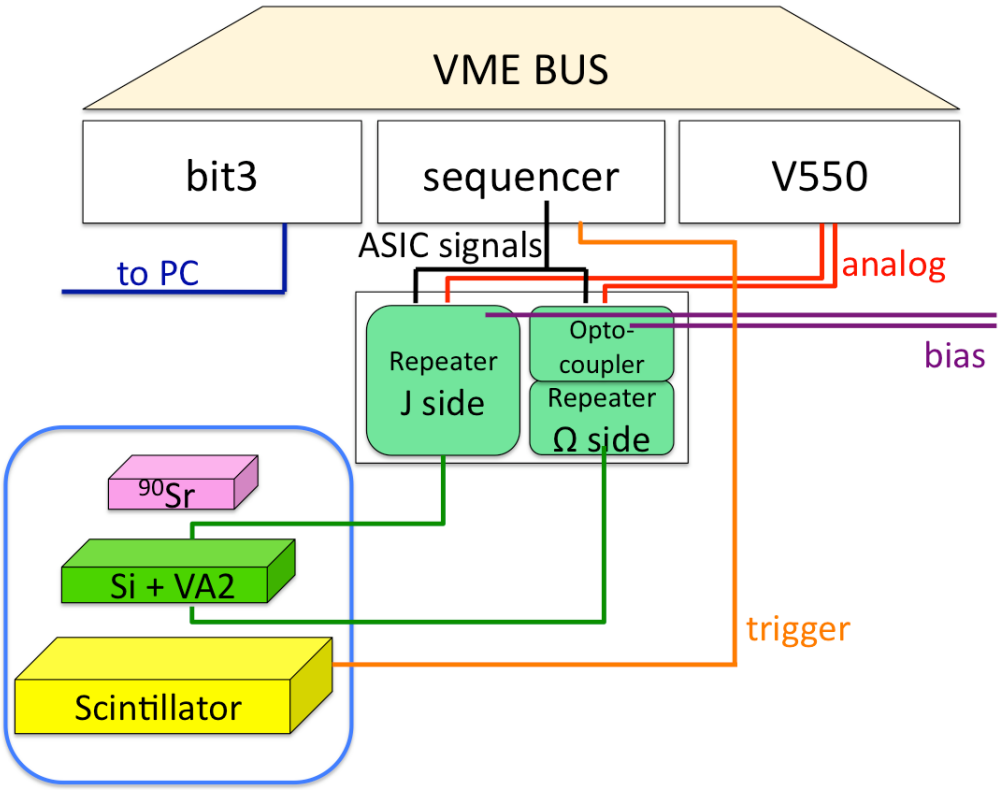

Figure 3.12: The DAQ chain used in the tests performed at Como.

lows a VME cycle duration of 1 μs in the DMA (Direct Memory Access) mode[6]. The DAQ software is written in C with Tcl/Tk for the user graphical interface (figure 3.13). The trigger signal is sent to the trigger board and then to a VME sequencer (designed by INFN Trieste) to generate the DAQ trigger which is the one starting the readout sequence. The ASIC readout signals are generated by the sequencer and brought to the detector by a 16 pin scotchflex cable. The analog signals are converted to digital ones by the CAEN[7] V550 flash ADCs.
The V550 ADCs can work in "zero suppression" mode: only the channels over

[5]SBS Technologies, Inc., US, http://www.sbs.com

[6]The DMA is a special access mode in which the data are transferred from the VME memory to the computer one without the PC generating the address of each location to be transferred.

[7]http://www.caen.it

Figure 3.13: The DAQ user interface.

a given threshold are readout. During the readout, data are transferred from the ASICs to the ADCs with a 5 MHz clock; in the ADCs, pedestals (section 3.2.3.1) are subtracted and the result compared with a threshold that depends on the channel noise. Typically less than 5 strips (out of 384) are over threshold reducing in this way the readout time. In the laboratory tests, this mode has not been used and thus all the strips have been readout.

3.2.2 The test goals

The goal of the tests performed at Como was to analyze the behavior of each telescope module when the particles (electrons coming from a ^{90}Sr source with a maximum energy of 2.280 MeV) cross the detector. Each INSULAB telescope module has been studied with the following figures of merit:

- the *noise*: it has been evaluated considering the pedestal runs (section 3.2.3.1). The common mode noise contribution has then been estimated;

- the *pull distribution*: it allows to select the events in which the particle has crossed the detector (section 3.2.3.2);

- the *cluster identification*: in order to find the exact position of the particle in the detector the center of gravity method has been applied (section 3.2.3.2);
- the ^{90}Sr *profile*: it allows to determine the dead or noisy strips and exclude them from the analysis (section 3.2.4);
- the *cluster pulse height distribution*: it allows to study the signal shape of the obtained cluster for each module (section 3.2.4);
- the *cluster SNR distribution*: it allows to estimate the signal over the noise ratio for each side of the four modules (section 3.2.4);
- the *hold scan*: it has been performed in order to study the correct sampling of the signal generated by the VA2 ASIC (section 3.2.4.1). The ASIC shaper peaking time can vary in the range 1-3 μs depending on the ASIC parameters; the scan allows to measure the analog shape of the signal and thus to evaluate the hold value to be chosen.

3.2.3 The analysis procedure

The event selection has been performed taking into account only the single track events, that is the events in which only one single particle crosses the double side microstrip detector. The basic procedure for the data analysis consists in:

- the acquisition and the analysis of the pedestal run (section 3.2.3.1) baseline, its noise and the common mode contribution;
- the data acquisition and selection of the good events (section 3.2.3.2); given that in each event the particle can deposit its energy in more than one strip, a cluster-finding algorithm has been applied to identify the exact position of the particle crossing the detector. The position is defined using the center of gravity method.

3.2.3.1 The pedestal analysis

A particle crossing a silicon microstrip detector deposits a charge which moving under the influence of an electric field generates a current which is then amplified, sampled and sent to the ADC for the digitization. When there are no particles, the ADCs digitize anyway a signal which is the baseline of the complete detector+electronics chain: this baseline is called *pedestal*.

To evaluate the pedestal and the noise of each channel, a pedestal run of 200 events is acquired with a random trigger. The mean value of each channel represents the pedestal while the rms corresponds to the noise. Figure 3.14 presents

an example of a pedestal of one silicon module (both for the ohmic and junction side): figure 3.14(a) shows the pedestal where the three different regions correspond to the three readout ASICs; figure 3.14(b) shows the noise rms. The black histogram is the global noise rms while the red one the noise rms after the common mode subtraction. The common mode noise is the noise contribution due

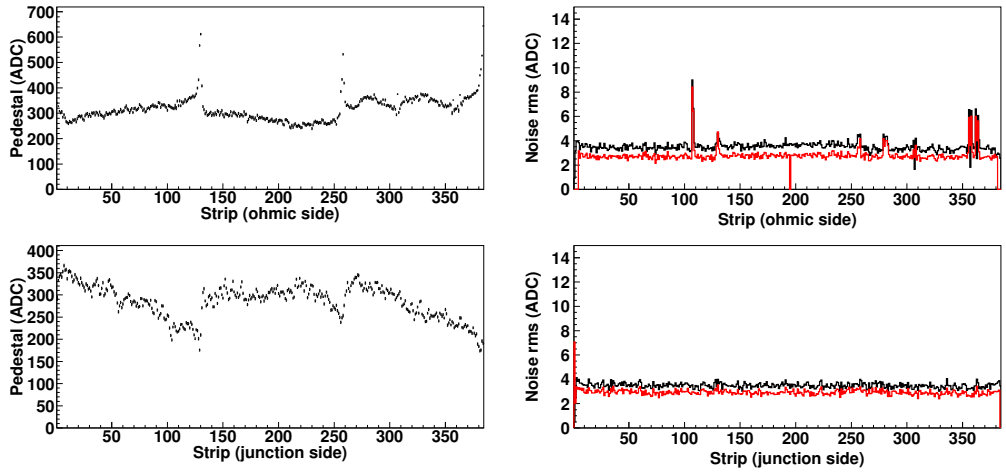

(a) (b)

Figure 3.14: The pedestal analysis: a) the pedestal value for each strip of the ohmic and junction side of the detector module; b) the corresponding noise rms (in black) and the noise rms after the common mode subtraction (in red).

to the external noise on the detector bias line (for example the electromagnetic noise). It causes a common variation of the baseline of all the strips on an event by event basis. In order to compute the pedestal and the noise rms without the common mode contribution (that is the intrinsic noise), the following procedure has been applied:

- the pedestal and the noise rms values of each strip have been evaluated;
- the common mode for each ASIC has been computed:

$$CM_j = \frac{\sum_i^N (raw_i - pede_i)}{N} \tag{3.1}$$

where j represents the number of the ASIC and runs over the total number of ASICs (1-3), while i is the number of channels for each ASIC and may run over the total number of ASIC channels (1-128). The pedestal value

of each channel ($pede_i$) is subtracted from the raw data (raw_i) event by event. The mean value (CM_j) has been computed excluding the dead or noisy channels (N represents the number of good channels). The rms value associated to this number represents the common mode noise;

- the common mode value has been subtracted event by event from the raw data;
- the pedestal and the noise rms distributions have been re-computed.

Figure 3.15 shows the common mode distributions for the ohmic and junction side of the considered module; both of them have been fitted with a Gaussian function: the mean value is practically 0, while the rms is $\sim$1.7 ADC in the first case and $\sim$1.8 ADC in the second one. Taking into account figure 3.14(b), it can be seen that an average value of $\sim$3 ADC has been obtained for the global noise after the common mode subtraction.
Figure 3.16 presents the correlation of the common mode distribution of two dif-

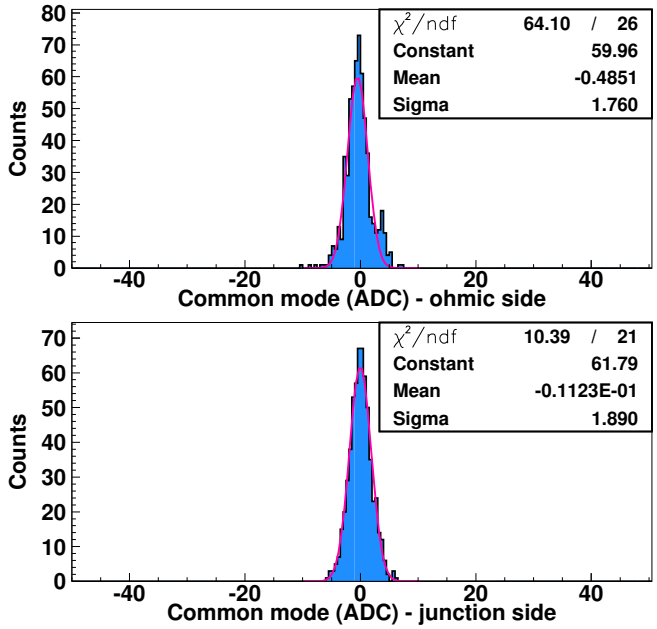

Figure 3.15: The common mode distributions for the ohmic and junction side of a telescope module.

ferent ASICs connected to the same silicon detector: the correlation demonstrates that the common mode noise is a detector feature.
Given the ADCs work in "zero suppression" during the data taking on the beam

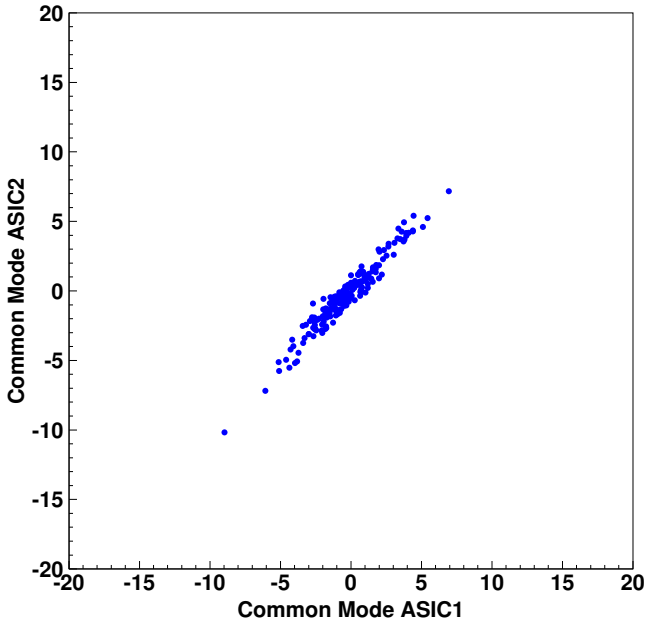

Figure 3.16: The common mode correlation of two readout ASICs of the same silicon detector side.

(section 3.2.1.2), the pedestals are subtracted online. The threshold for the zero suppression is set to 5 times the noise rms value (the global one, not the common mode subtracted one). To read the silicon detectors in this mode, the common mode contribution to the total noise should be small; in case of a high noise in fact the threshold should be increased reducing the detector efficiency or the number of strips per cluster (and therefore the spatial resolution). On the other hand, high noise and standard threshold means a larger number of strips to read per module (since they are over threshold) and thus a smaller DAQ rate. Figure 3.17 presents the study of the number of strips above the threshold as a function of the considered threshold value (cut); by using a high cut (i.e. 30) the lateral strips which form the cluster are lost and therefore the center of gravity is shifted from the real position. On the contrary, with a low cut (i.e. 6) the number of strips above the threshold takes into account the lateral strips and the position reconstruction is adequate. The number of strips above threshold on the ohmic side is smaller given there is no floating strip and thus the number of strips forming a cluster is smaller.

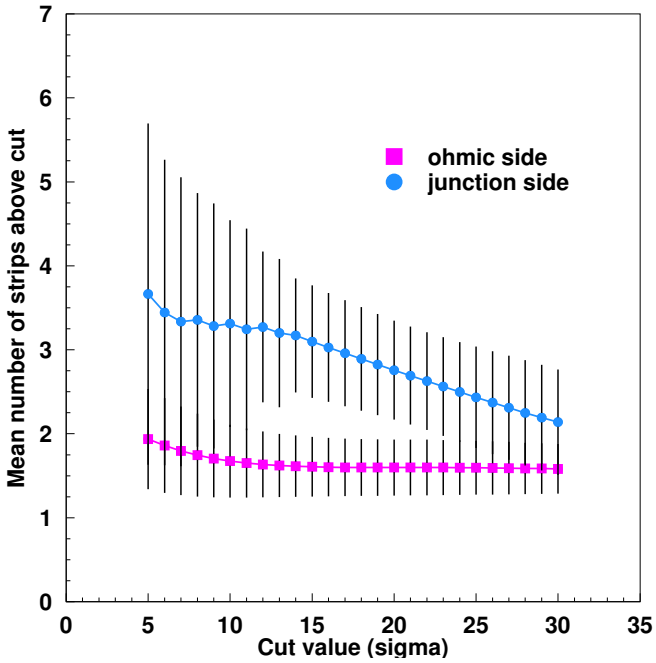

Figure 3.17: Number of strips above the threshold as a function of the cut value.

3.2.3.2 The good event selection

To find the exact position in which the particle has crossed the detector, identifying the group of strips in which the particle has released its energy, the *pull* distribution has been evaluated. It is defined as the ratio between the pulse height (that is the particle signal which is obtained subtracting from the raw data the pedestal value) of the strip with the maximum signal in the event and its corresponding noise rms: in other words the signal is expressed in terms of its noise rms. The pull distribution of one detector module (ohmic and junction side) is shown in figure 3.18. The threshold (magenta line) is set to exclude the region corresponding to the noise (the peak at very small values).

Given that the tracks incidence angle is not always perpendicular with respect to the strip, the charge can be released (and thus readout) in several neighbouring strips: this set of adjacent strips is called cluster. A cluster-finding algorithm has been applied to find the exact position of the particle in the detector by means of a center of gravity method. The cluster identification has been performed taking into account the strips that surround the one with the maximum and choosing a lower threshold for their signals (typically the chosen threshold was 5σ). The

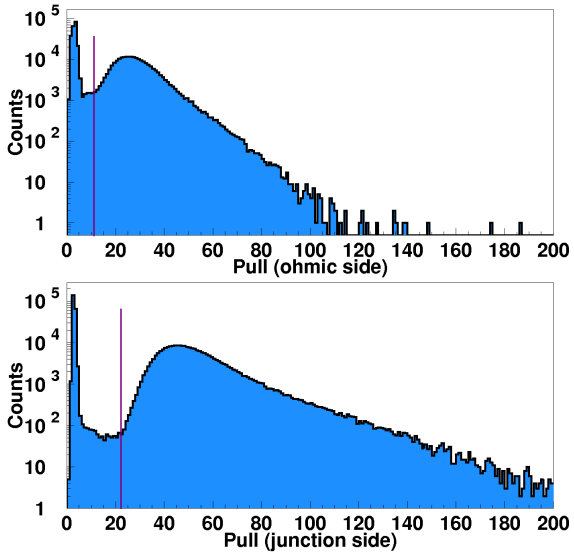

Figure 3.18: The pull distribution of one silicon detector module (ohmic and junction side); the magenta line indicates the threshold for the analysis to consider an event as good: in the ohmic case it is around 8 while in the junction one around 22.

crossing position of the particle is defined as:

$$xpos = \frac{\sum_i (x_i \cdot PH_i)}{\sum_i PH_i} \tag{3.2}$$

where the i index runs over the number of strips that compose the cluster, x_i is the position of the i*th* strip of the cluster and PH_i the pulse height of that strip.
Figure 3.19(a) shows the distribution of the number of strips per cluster: generally the cluster is composed of 2-3 strips. The junction side has a larger number of strips because it is readout with a floating strip scheme, thus the charge is capacitively distributed on more strips.
To apply the first event selection, the distribution of the number of clusters per event has been considered[8]: almost 90% of them is a single cluster event as presented in figure 3.19(b). The good events have been therefore defined as the ones in which only one cluster is present on each side of the silicon detector.

[8]Two clusters are considered as separated if there are at least two strips below threshold between their facing borders.

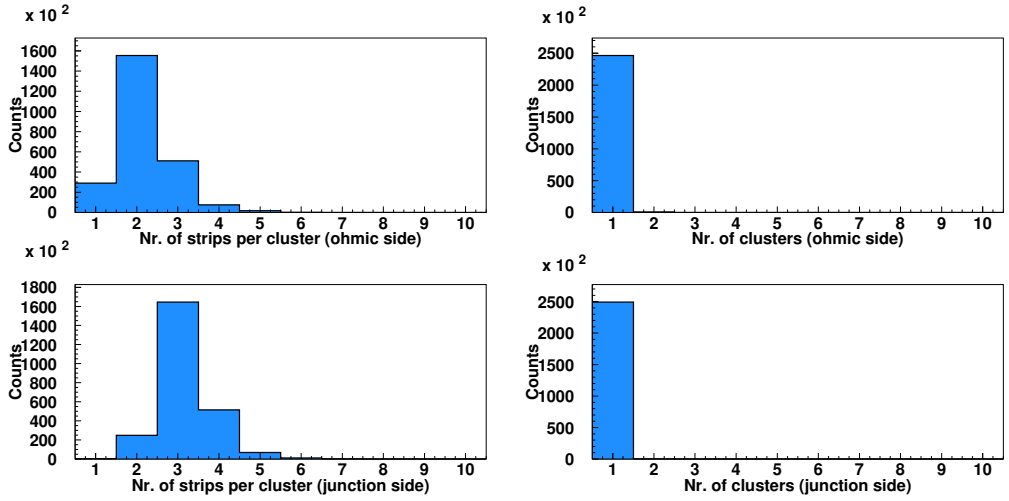

(a) (b)

Figure 3.19: The distribution of a) the number of strips per cluster and b) the number of clusters for each side of the detector module.

3.2.4 Test results with the ^{90}Sr source

Each silicon strip detector of the INSULAB telescope has been tested at the Como laboratory using a ^{90}Sr β-source (figure 3.20(a)) which has been placed above the module.
The ^{90}Sr isotope undergoes a β^- decay with a decay energy of 0.546 MeV distributed among an electron, an anti-neutrino and the ^{90}Y which in turn undergoes a β^- decay with a half-life of 64 hours and a decay energy of 2.28 MeV distributed among an electron, an anti-neutrino and the ^{90}Zr, which is stable[9] (figure 3.20(b)). Therefore the electrons are isotropically emitted, with an energy spectrum with an end point of 2.280 MeV. The emission rate is about 5000 particles/s. The following plots refer to a high statistics run (460000 events) with the D4 detector; the bias voltage for this module was 36 V (the current was 400 nA). Once the particle position had been identified as explained in the previous section, the profile histograms for the ohmic and junction side of the silicon module have been considered (figure 3.21): as expected both the distributions are quite flat given the β emission is isotropic and the β source was rather far from the detector surface. These distributions allow to identify the dead or noisy channels in order to exclude them from the analysis; in this case, as can be seen in figure 3.21, the switched off strips are:

- on the ohmic side: 1-2-3-384 (dead) and 306-307-356-357 (noisy);

[9] http://atom.kaeri.re.kr/cgi-bin/decay?Sr-90+B-

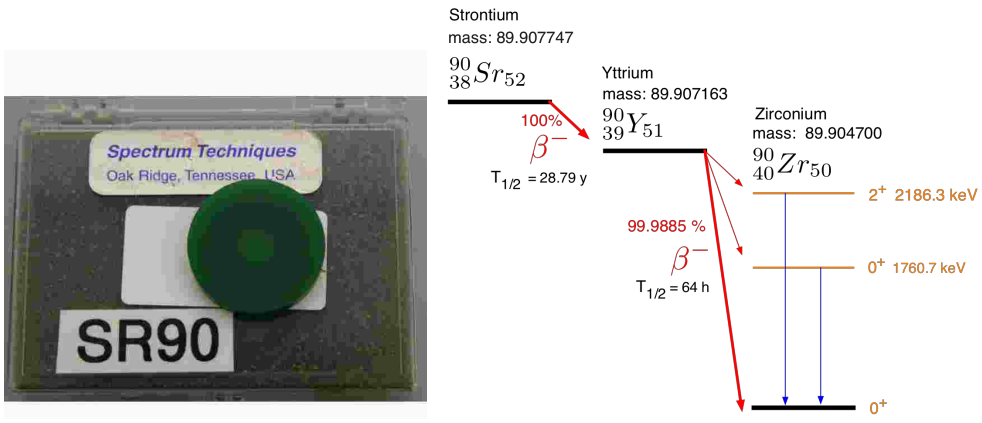

(a) (b)

Figure 3.20: a) The ^{90}Sr source used in the tests and b) its decay scheme.

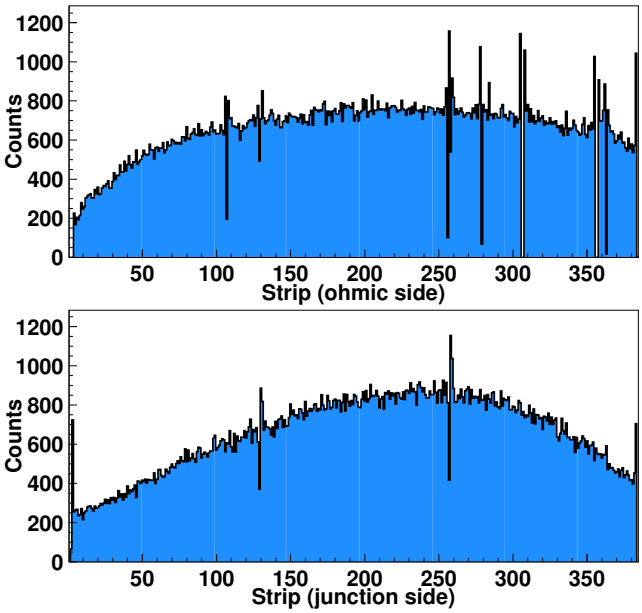

Figure 3.21: The ^{90}Sr profile measured with the silicon microstrip module (ohmic and junction side).

- on the junction side: 384 (dead).

The peaks in the profile histograms are due to these dead/noisy strips or to strips with a low efficiency, which results in the nearby strip detecting the particle.
The following step in the procedure allows to study the analog response of the detector in terms of the cluster pulse height (figure 3.22(a)) and its signal to noise ratio (figure 3.22(b)). The cluster SNR is defined as:

$$SNR_{clu} = \frac{clu}{clunoise} \tag{3.3}$$

where clu is the signal of the cluster (the sum of the pulse heights of all the strips forming the cluster) and $clunoise$ its noise rms after the common mode subtraction. The noise rms of the cluster is defined as:

$$clunoise = \sqrt{\frac{\sum_i^N \sigma_i^2}{N}} \tag{3.4}$$

where σ_i is the noise rms of each strip forming the cluster and N the number of strips per cluster. Both these plots have a Landau-like distribution that can be

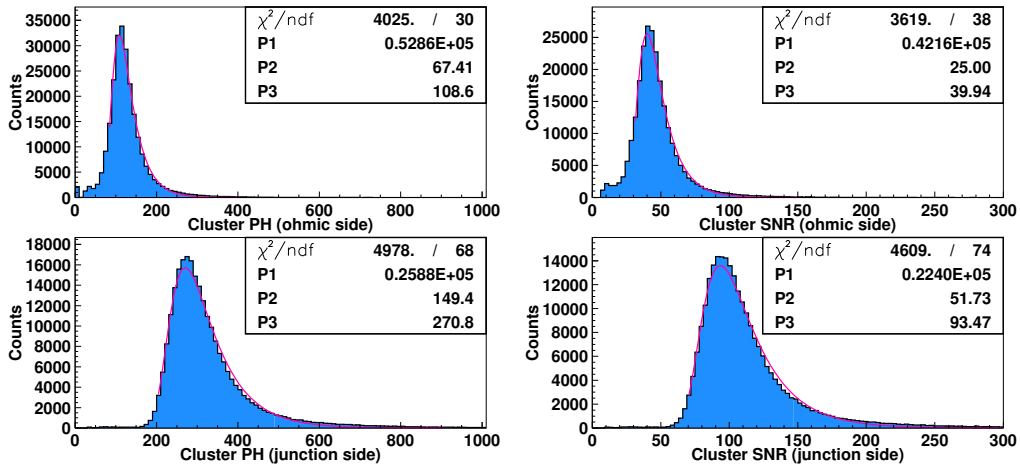

Figure 3.22: The cluster a) pulse height and b) SNR distributions.

fitted with the following parametrization:

$$\begin{aligned} F(\lambda) &= \frac{1}{\sqrt{2\pi}}\exp[-0.5(\lambda+\exp(-\lambda))] \\ \lambda &= \frac{\Delta E - \Delta E_{MP}}{\xi} \\ \xi &= \mathrm{FWHM}/4.02 \end{aligned} \tag{3.5}$$

where ΔE_{MP} is its most probable value (MPV) [50]. The three parameters obtained from the fit represent respectively the normalization factor (P1), the FWHM (P2) and the most probable value (P3). In the ohmic side case, the MPV is 106 ADC for the cluster pulse height and 39 for the cluster SNR while for the junction side the MPV is 271 ADC for the cluster PH and 93 for the cluster SNR.

3.2.4.1 The hold scan

As explained in section 3.2.2, one of the ways to evaluate the analog shape of the signal generated by the VA2 ASIC is the use of the hold scan. The hold is defined as the interval between the trigger signal (which is generated by the particle crossing the scintillator) and the sampling of the signal peak. The idea is explained in figure 3.23. At t=0 the particle crosses the silicon detector and the

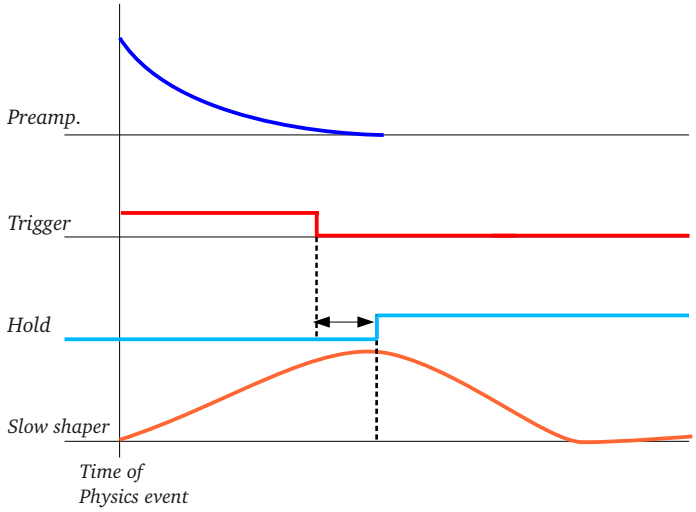

Figure 3.23: After the particle passage, the signal is amplified by the preamplifier; the trigger is generated by the scintillator. The hold signal is generated by the data acquisition system to sample the shaper output peak.

deposited charge is amplified by the preamplifier. The trigger signal is generated by the scintillator and then processed by the VME sequencer which at this point generates the hold delay. The rising edge of the hold signal is the one sampling the shaper output. The sampled value is stored to be sent to the ADC during the readout procedure.
Given that the hold value must be set in order to sample the peak of the signal, the shape of the analog signal can be obtained varying the hold interval in the range 0-2500 ns, the maximum achievable with this readout board, thus sampling the

signal in different places. The hold scan therefore allows to reconstruct the shape of the signal and thus to evaluate the hold value that corresponds to the maximum of the signal. The knowledge of the shape of the signal is fundamental not only to choose the hold value but also to understand how much freedom one has on the beam where such a choice is complicated by long cables.

To perform the hold scan the procedure described above has been applied to all the modules of the INSULAB telescope. A run has been performed for each of the hold values in the range 100-2500 ns and the pulse height of the strip with the maximum signal in the event has been considered and fitted with a Landau function, as shown in figure 3.24. The most probable values have then been plotted as a function of the hold one as shown in figure 3.25.

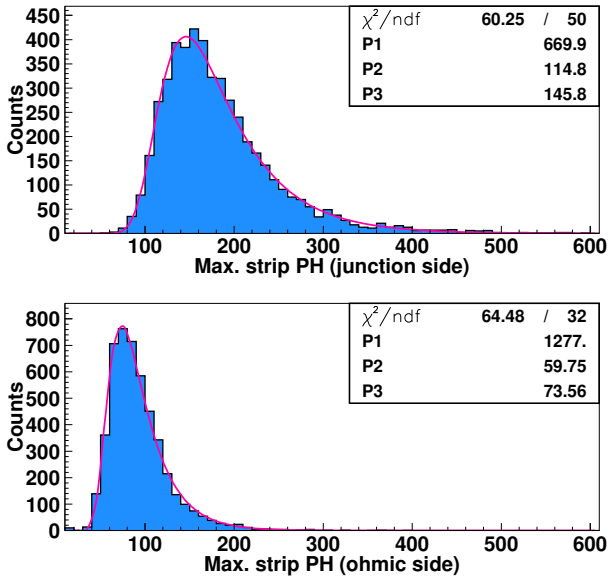

Figure 3.24: The pulse height of the strip with the maximum value fitted with a Landau function for both the ohmic and junction side of the module.

The peaking time is located at ∼1200 ns for the junction side and ∼1500 ns for the ohmic one; both these values are smaller than the ones computed with the calibrate (figure 3.7) because of the delay introduced by the trigger generation. In both cases the top part of the signal is constant for at least 500 ns, which allows some freedom in the hold choice on the beam setup.

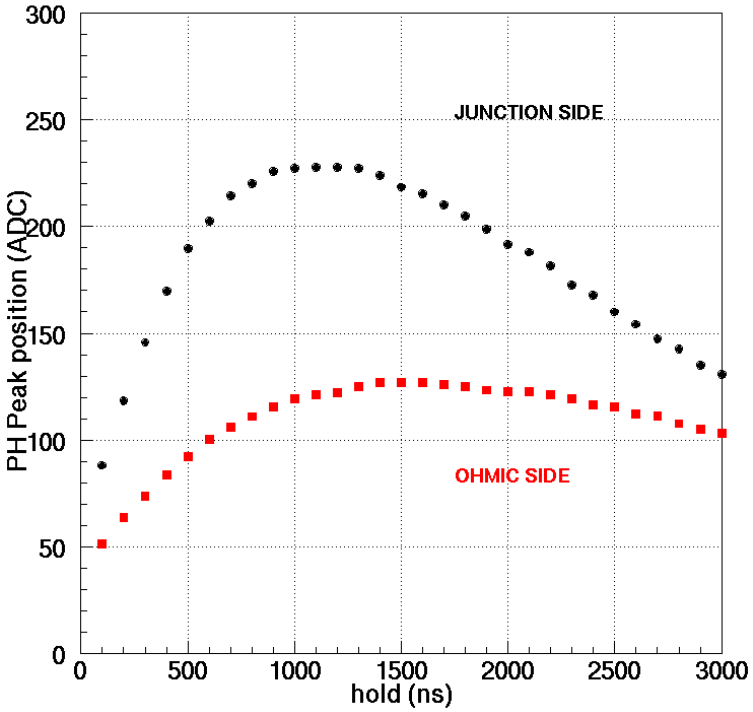

Figure 3.25: The hold scan to reconstruct the signal shape for both the junction and ohmic side; the peaking time is around 1200 ns for the junction side and 1500 ns for the ohmic one.

3.3 Commissioning tests at the CERN SPS H4 line

This section describes the setup used in 2012 on the CERN SPS H4 line: the INSULAB telescope, the trigger system, the new fast readout electronics and its performance. The results in terms of beam profile, pulse height and pull distributions obtained with the new setup are presented.

3.3.1 The H4 beamline

The beamtest has been performed on the H4 line at the CERN SPS (Super Proton Synchrotron) North Area. The SPS (figure 3.26[10]) is a 6.9 km circumference circular accelerator, housed in a tunnel straddling the border of France and Switzerland, and nowadays is used as the final injector for the high intensity proton beams of the LHC experiment. It accelerates protons from 26 GeV/c to 450 GeV/c. The SPS is also used to provide particles with a momentum up to 450 GeV/c to the external lines (North Area), COMPASS (COmmon Muon and Proton Apparatus for Structure and Spectroscopy) and CNGS (CERN Neutrinos to Gran Sasso).

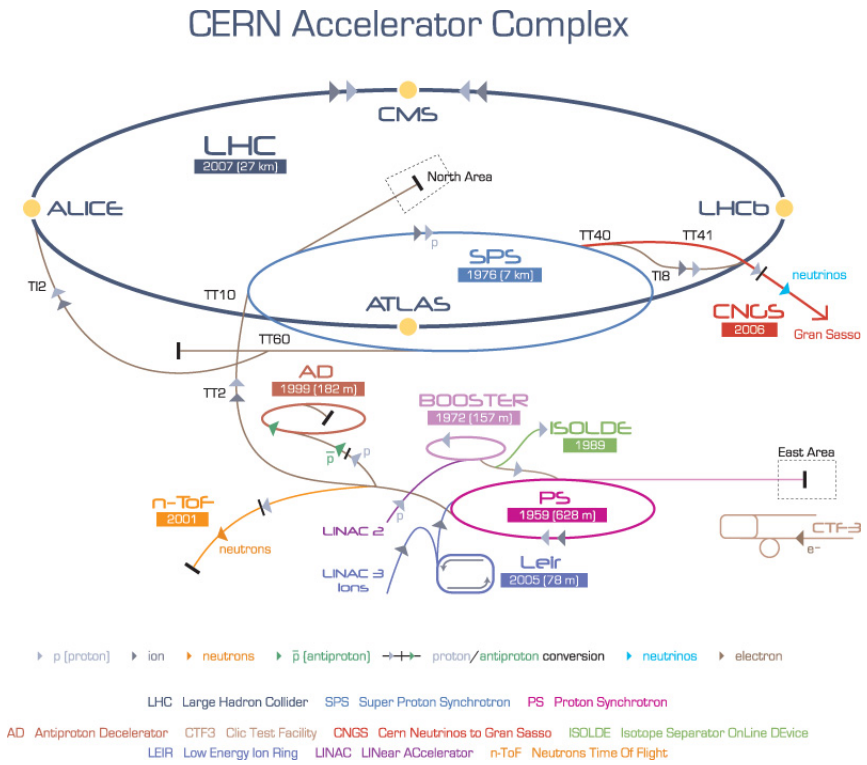

Figure 3.26: The CERN accelerator complex.

[10] http://bigscience.web.cern.ch/bigscience/en/lhc/lhc2.html

The SPS consists of a total of 1317 magnets of which 744 are bending ones to curve the particles along the ring. Radiofrequency cavities can accelerate protons, antiprotons, oxygen and sulfur nuclei, electrons and positrons up to 450 GeV/c: the particles are first accelerated by a LINAC (up to 50 MeV) and by the PS up to 26 GeV/c. In the North Area (figure 3.27), where the H4 line is located, the beam structure foresees a maximum intensity of 2×10^8 particles per bunch (the spill) for a bunch duration in the range of 4.8-9.6 sec with a repetition period of 14-48 sec, depending on the number of facilities which need the SPS extraction.

Figure 3.27: The North Area complex where the H4 line is located.

In June 2012 the tests on the INSULAB telescope have been performed with 150 GeV/c electrons. The electrons on the H4 line are obtained in the following way (figure 3.28):

1. a primary proton beam, extracted from the SPS towards the North Area, splits into three beams of which one is directed onto the T2 primary target;
2. from the T2 target and thanks to the T2 wobbling station[11] two secondary beams are derived: the H2 and H4 beams;
3. the B3T magnet of the wobbling is used as a sweeping magnet: the charged particles are absorbed in the TAX, while the neutral ones go through and hit the converter;

[11] The aim of the wobbling station is to have the maximum flexibility in the use of a given target station by allowing the beam to hit the target under a variable angle.

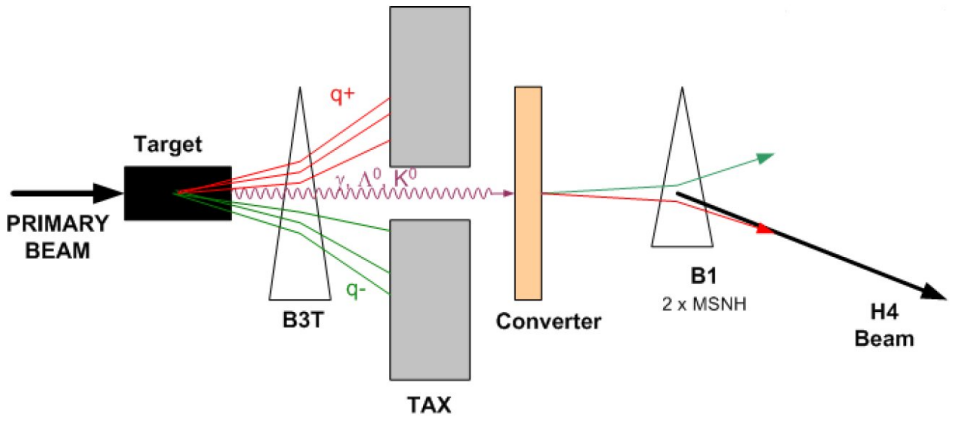

Figure 3.28: The electrons production from γ-conversion on the SPS H4 line.

4. the γ converts in a lead converter to produce electrons and positrons (e^-, e^+);

5. the B1 magnet is used to select the charge and particle for the tertiary beam. The beam intensity on the H4 line is of the order of a few thousands electrons per spill at this energy.

3.3.2 The experimental setup

Figure 3.29 presents the experimental setup. It consists in:

- the INSULAB telescope, described in section 3.1 and shown in figure 3.30;
- a plastic scintillator (section 3.2.1.1) used for the trigger generation;
- the new data acquisition system (section 3.3.2.1).

3.3.2.1 The new DAQ system

The standard DAQ system of the INSULAB telescope (section 3.2.1.2) was based on an off-the-shelf ADC (the V550 by CAEN) which could work in zero suppression allowing to increase the DAQ rate. Such an implementation requires to write the data on the PC at each event, which is not ideal when working with a pulsed beam such as the ones of the CERN extracted beamlines where the spill duration and cycle vary depending on the line. For instance, on the PS East Hall lines the spill lasts 400 msec with one spill per 45 sec cycle in the worst case and 3 spills per cycle in the best one (with a time distance which depends on the cycle type)

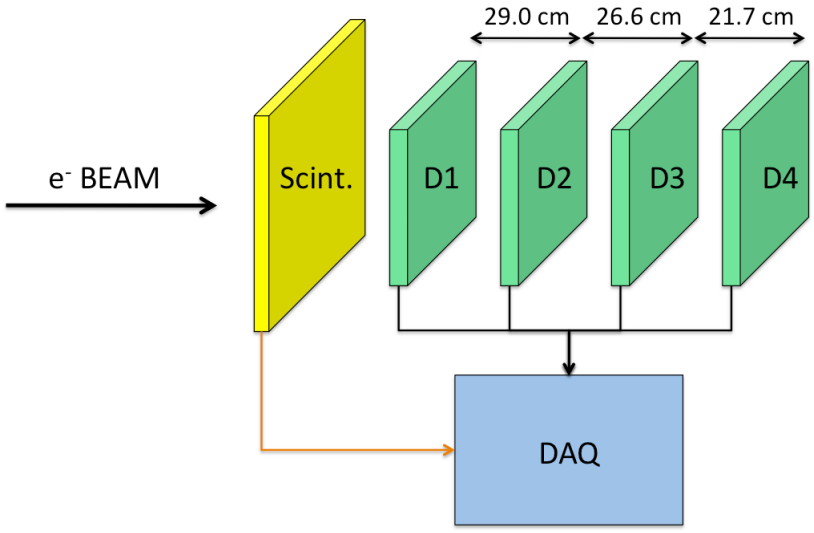

Figure 3.29: A schematic view of the experimental setup used at the CERN SPS H4 line to test the telescope with the new readout system; the distances between the telescope modules (D1-D4) are indicated. The electron beam has a momentum of 150 GeV/c.

while on the SPS North Area lines it lasts 8 sec with a cycle of 45 sec. The standard DAQ system maximum rate was around 3 kHz when only silicon detectors were readout (that is only V550 modules were used and no calorimeters or other detectors were under study) and the overall noise of the silicon modules allowed a large enough cut for the zero suppression in order to have less than 5 strips per module above threshold.
The new DAQ system exploits a different philosophy: the events are stored in dedicated memories on the VME boards and transferred to the PC in the interspill period. The overall scheme is presented in figure 3.31. It consists of the following items:

- VME side:
  - a trigger board (INFN-Trieste) which allows the user to choose the trigger type and generates the DAQ trigger. The input signals to this board are the ones coming from the scintillators, the spill signal (given the trigger generation is vetoed when the spill signal is not present) and a random signal which is used for the pedestal run. Several scalers are present on the board to evaluate the particle rate;

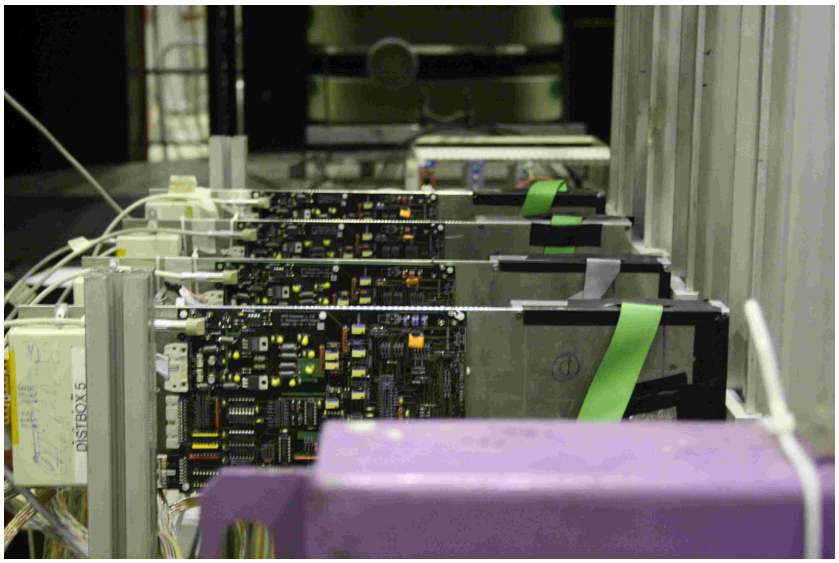

(a)

(b)

Figure 3.30: View of the four INSULAB telescope modules with the new readout system; the electron beam comes from a) the bottom and b) the right.

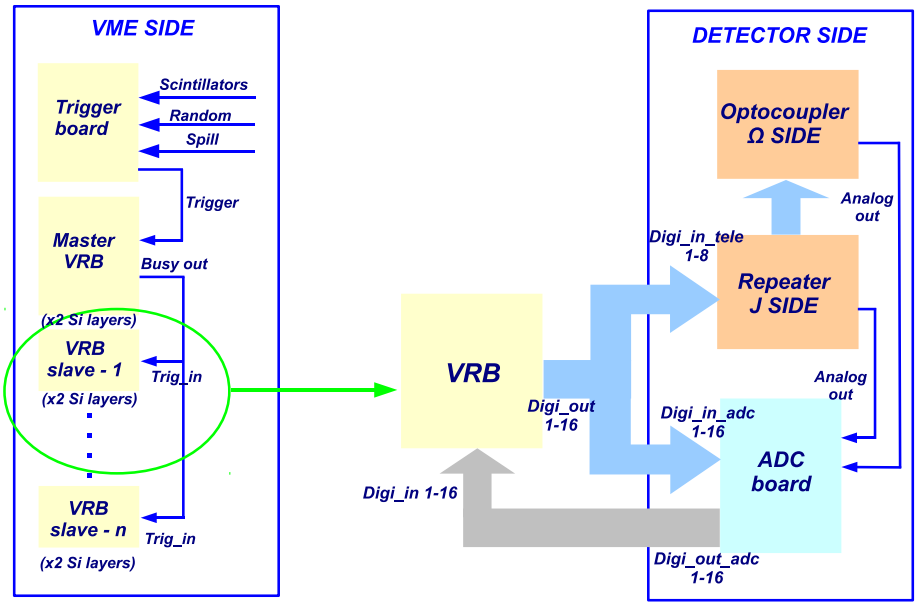

Figure 3.31: The scheme of the new DAQ system.

  - a set of VRBs (VME Readout Board, INFN-Trieste). They are general purpose boards designed for the Electron Muon Ranger [78] of the MICE experiment [79]. One of the boards acts as the master, taking the trigger from the trigger board, starting its readout sequence and generating the busy_out signal which is the trigger for the slave VRBs (which in turn start their readout). Each VRB can read up to 2 silicon sides (in the telescope case, the junction and ohmic side of a single module). The VRB (figure 3.32) hosts an Altera EP2C50 FPGA (Field Programmable Gate Array) with 50k cells and 581 kbit of internal RAM (which allows also to check complex designs with the embedded logic state analyzer) and 4 PLLs (Phase Locked Loop) for the clock generation. The board has 16 LVDS (Low-Voltage Differential Signaling) inputs and 16 LVDS outputs, 2 TTL inputs and 2 TTL outputs, a TLK1501 Gigabit link and 4 Mword of 32 bit RAM. The FPGA is also responsible of the interface with the VME A32D32 and has the possibility to generate interrupts.

- detector side:

  - the interface between the VRB and the detector module is performed by the ADC board (figure 3.33) which hosts up to 3 AD9220 ADCs (in the telescope case, two of them are used) to digitize the data from the ASICs. The interface between the VRBs and the ADC boards uses

only digital signals (given the digitazion is performed on the ADC board itself). The communication with the VRBs is performed with 16+16 I/O LVDS lines. The board is controlled by an Altera EP2C8 FPGA.

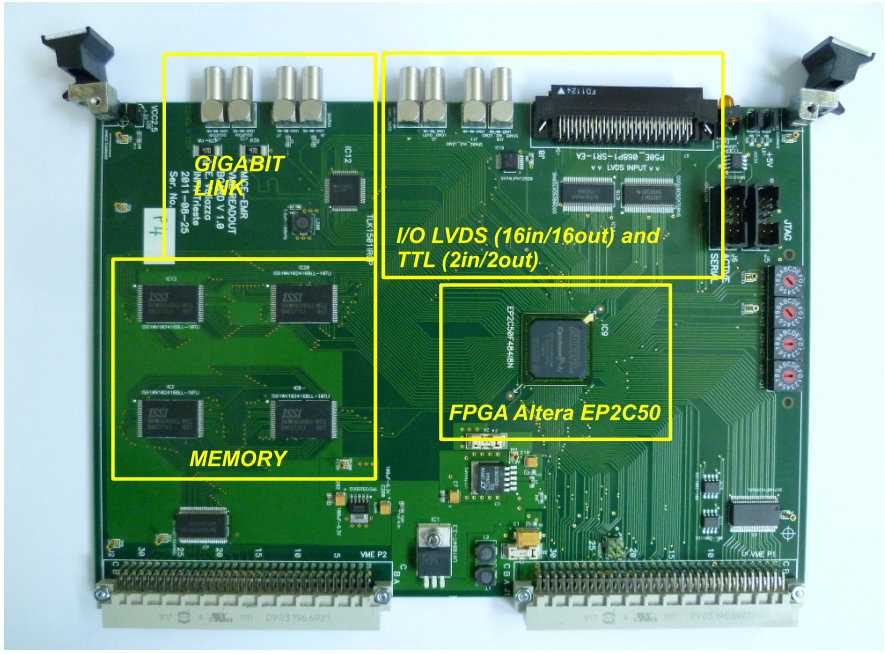

Figure 3.32: The VRB.

The readout sequence is the following:

- the data of each silicon side are multiplexed with a 5 MHz clock, so that each AD9220 receives 384 channels (128 $\times$ the 3 ASICs of each silicon side);
- the AD9220 digitizes at 5 MHz and the ADC board multiplexes the two outputs of the AD9220s on a single line alternating one word from one ADC to one of the other one, that is one channel from the junction side and one channel from the ohmic one. The channel info is stored in a 12 bit word plus 1 bit for the overrange. The multiplexing is performed with a clock of 10 MHz given the input one is at 5 MHz;
- when the VRB receives the data, two possible operation modes are foreseen:
  - case 1: the input from each ADC board is de-multiplexed and each stream of data is copied in the RAM; the VRB has been designed to

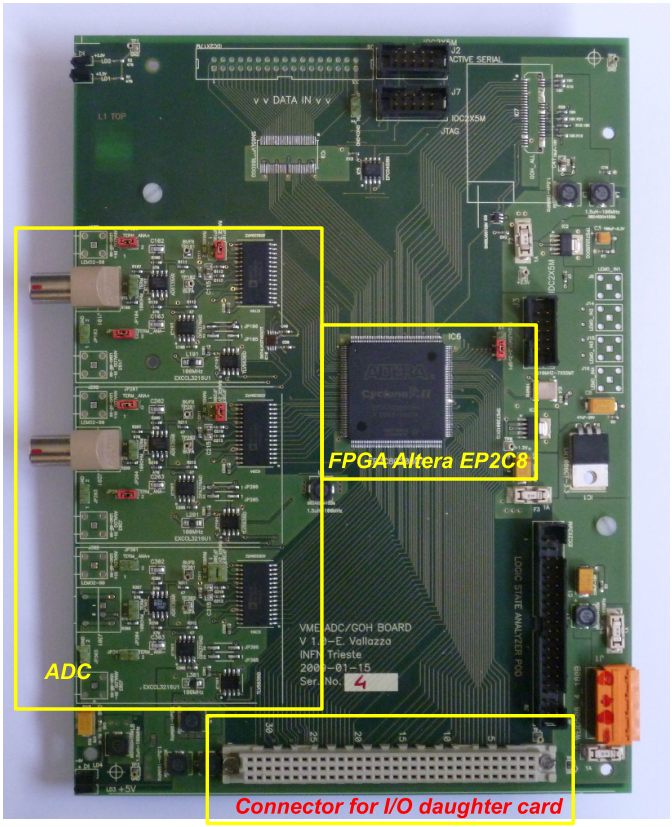

Figure 3.33: The ADC board that is the interface between the VRB and the detector module.

store at maximum 4096 events with 384x2 strips each. This is the solution adopted for the pedestal run and for the non zero suppressed runs;

– case 2: the input from each ADC board is de-multiplexed, the data are zero suppressed in the FPGA and then copied in the RAM. To perform the zero suppression, the FPGA compares the data with the threshold (which is given by the pedestal of the channel increased of n $\times$ the noise rms) and if it is above threshold, it stores the address and the value up to a maximum of 16 strips per event per module (that is per block of 384 strips). The VRB in this case allows to store 65536 events of 16x2 strips each.

- for each event, each VRB generates a timestamp which is sent together with the event number to the corresponding ADC board. The ADC board includes in the stream of data both the timestamp and the event number and

sends them back to the VRB which uses them as a check; if they are not the same, the event is considered corrupt and it is discarded. During the shift of the data from the ADC boards to the VRBs, the ADC board FPGA performs a bitwise XOR of each strip with the following one for all the strips. The final number is the last info of the data stream sent to the VRB which stores it in the memories. During the interspill period, this number is checked by the software to accept the event.

To compute the maximum speed allowed by the new DAQ system, the following considerations hold:

- the main contribution to the non reducible dead time is given by the shift of the data from the ASICs to the ADCs, which is performed with a 5 MHz clock; since 384 channels have to be shifted together with the timestamp and a few dummy clocks required by the readout sequence, this amounts to 80 μs. The only way to reduce this number is to read in parallel the 3 ASICs thus needing only 128 clock pulses, which is not possible with the present version of the telescope;
- the VRBs have to be initialized at each event which requires around 30 μs per board, corresponding to 8 VME instructions.

Adding the two values one obtains an overall time to readout an event of 170 μs if 3 VRBs are used (that is 6 silicon sides are readout) which corresponds to a DAQ rate of about 6 kHz. It must be underlined that the time distribution of the particles on the extracted beamlines is poissonian, which means that this maximum DAQ rate can be reached if the particle input rate is large enough.

3.3.3 The test goals

The goal of the tests performed at the CERN H4 beamline was to analyze the performance of the INSULAB telescope with its new readout electronics, using an electron beam with a momentum of 150 GeV/c. This section presents the results obtained in terms of:

- *noise*, *pull distribution* and *cluster identification* with the procedure explained in section 3.2.3;
- *beam profile* in order to determine the dead or noisy strips excluding them from the analysis;
- *cluster pulse height*;
- *cluster SNR*.

Next chapter will deal with the spatial resolution which is the most important feature of a tracking system.

3.3.4 The H4 beamtest results

In the analysis procedure the events with one cluster per module side have been selected as described above. The junction sides measure the x position while the ohmic the y one. The pedestal analysis has been performed to evaluate:

- the pedestal distributions for each side of the INSULAB telescope (figure 3.34(a));
- the corresponding noise rms distributions before and after the common mode subtraction (figure 3.34(b)).

Figure 3.34 presents an example of such distributions obtained with one silicon module (D4): figure 3.34(a) shows the pedestal for the junction (top) and ohmic (bottom) side, while figure 3.34(b) its corresponding noise rms distributions.
The beam profile reconstructed with the telescope is presented in figure 3.35; the

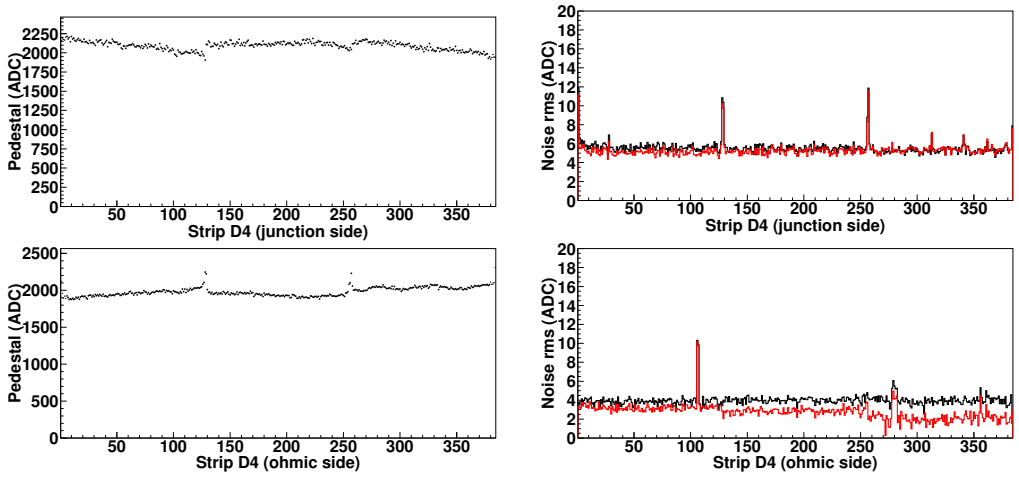

(a) (b)

Figure 3.34: The pedestal analysis in the tests performed at the CERN SPS: a) the pedestal value for each strip of the junction (top) and ohmic (bottom) side of the D4 detector module; b) the corresponding noise rms (in black) and the noise rms after the common mode subtraction (in red).

shape of the distribution is Gaussian-like. The behavior of the ohmic side of the

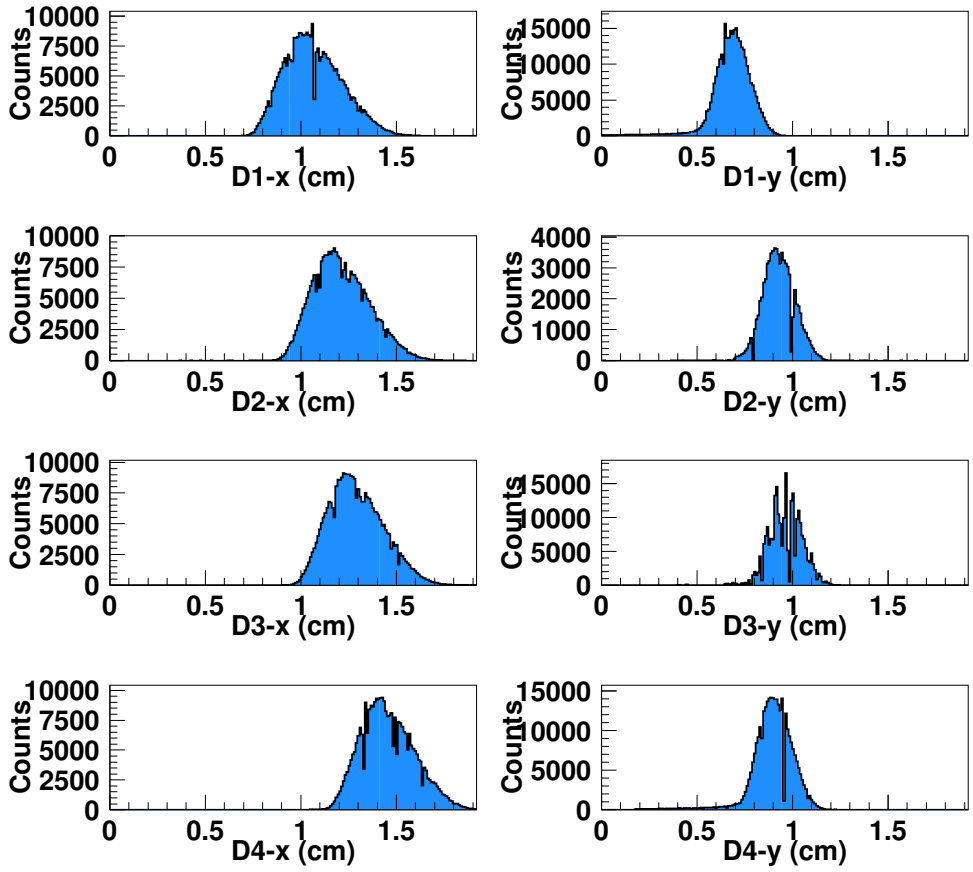

Figure 3.35: The beam profile measured by each of the four silicon telescope modules; the junction sides measure the x position while the ohmic sides the y one.

D3 module was not observed in the tests performed at Como and it has been ascribed to the high particle rate. This module is under investigation. The detectors had not been perfectly aligned on the beam, thus an offline alignment procedure has been applied as described in the next chapter.
Figure 3.36 presents the beam spot as measured by the D1 module: a dead strip causes a visible efficiency loss for x=1.1 cm.

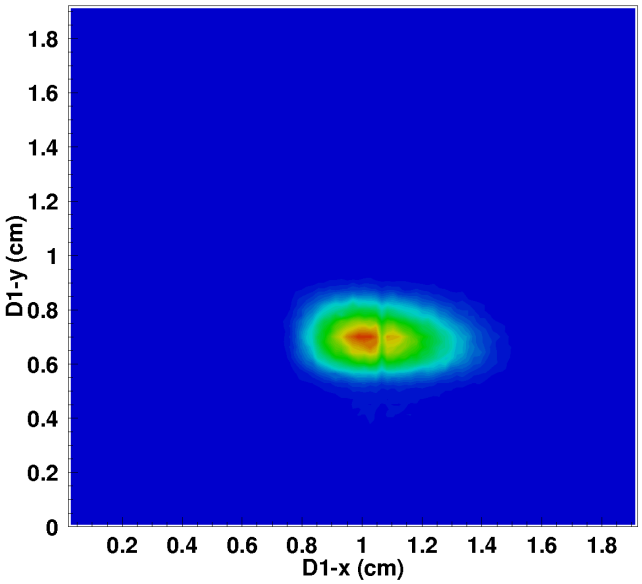

Figure 3.36: The two-dimensional beam profile as measured by the D1 module.

Figure 3.37 presents the beam divergence (that is the rms of the angular distribution of the beam particles) reconstructed using the D1 and D4 modules which is σ_x=132.8 μrad in the horizontal direction and σ_y=127.7 μrad in the vertical one.

Figure 3.38 presents the pull distribution for the strip with the maximum signal in the event computed for one of the modules (D4) both for the ohmic and junction sides. The shape of the distribution on the junction side is due to the presence of the floating strip: the peak at smaller values is generated by the particles that cross the center of the floating strip, while the one at larger values is caused by the particles crossing a readout strip.

The distributions of the number of strips per cluster and of the number of clusters per event have been then analyzed; figure 3.39(a) is an example of one of these distributions, computed for both the sides of the D4 module. Typically the number of strips per cluster varies between 1 and 2. Concerning the number of clusters per event, it has been found that almost 95% of the events has a single

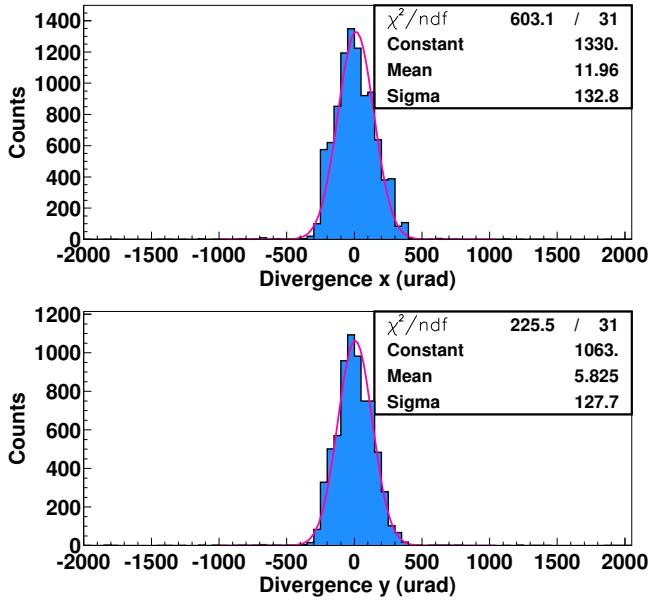

Figure 3.37: The beam divergence.

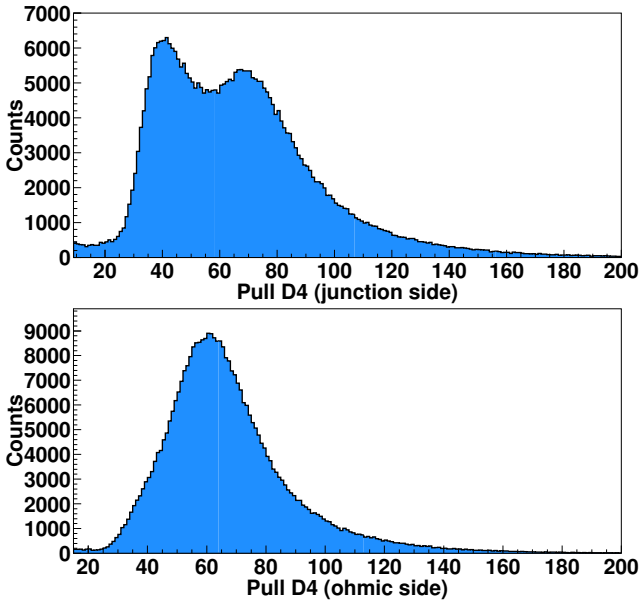

Figure 3.38: The pull distribution of the strip with the maximum signal of the D4 module.

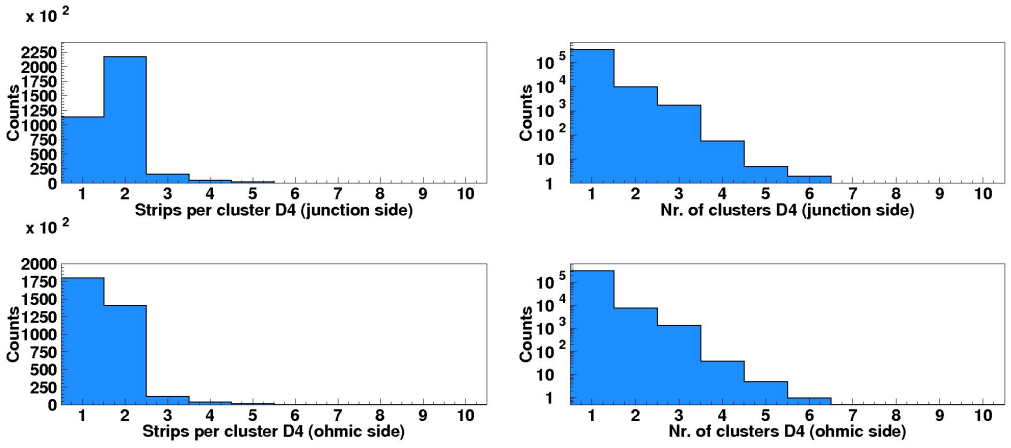

(a) (b)

Figure 3.39: The distribution of a) the number of strips per cluster and b) the number of clusters for the D4 module.

cluster, as shown in figure 3.39(b).
The cluster pulse height and the cluster SNR distributions have been evaluated as shown in figure 3.40 for the D4 module. Table 3.3 summarizes the cluster pulse

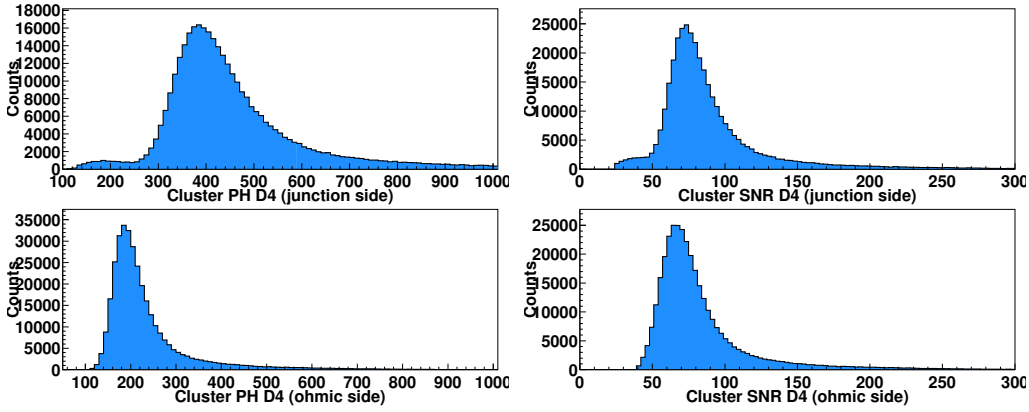

(a) (b)

Figure 3.40: The cluster a) pulse height and b) SNR distributions for the D4 module.

height, noise and SNR values of each of the four silicon telescope modules.

Module	Pulse height (ADC)	Noise (ADC)	SNR
D1-J	349.23	6.12	57.08
D1-Ω	202.15	1.71	118.12
D2-J	256.54	3.09	82.97
D2-Ω	202.15	2.27	89.03
D3-J	393.37	3.49	112.73
D3-Ω	228.64	4.80	47.61
D4-J	381.98	5.28	72.34
D4-Ω	184.99	2.85	64.80

Table 3.3: The cluster pulse height, noise and SNR values for each silicon module (J indicates the junction sides while Ω the ohmic ones).

Chapter 4

The telescope spatial resolution

To reconstruct the trajectory of a particle, position sensitive detectors have to be used: if several of them are present along the particle path (and are thin enough not to perturb the trajectory itself) the interpolation of the crossing positions allows the track reconstruction. The figure of merit of position sensitive detectors is the spatial resolution, that is the capability to reconstruct the impact point of the particle. As explained in chapter 2, in case of an analog readout system (like the one used by the INSULAB telescope) the spatial resolution of the microstrip detectors depends mainly on the following parameters:

- the readout pitch;
- the presence of intermediate strips (not connected to the readout electronic channels);
- the signal to noise ratio;
- the charge carrier diffusion.

In order to evaluate it, the distributions of the spatial residuals have been used: the residual is defined as the difference between the real particle impact point and the reconstructed position, obtained with a position finding algorithm. The spatial resolution of the detectors is defined as the rms of the distribution of the residuals and corresponds to the uncertainty in the reconstructed coordinates.
This chapter describes the results of the measurement of the spatial resolution of the ohmic and junction side of a telescope module. Moreover a detailed study of the particle charge distribution among the strips that compose the cluster has been performed using the η distribution. To reduce the dependence of the charge sharing from the particle impact position inside the strip, a dedicated algorithm has been applied improving the spatial resolution and allowing to compute the effective charge sharing.

4.1 The spatial resolution

As described in section 2.5.3, the spatial resolution is the rms distance of the measured coordinate from the true hit position. Two are the elements that have to be taken into consideration to compute the spatial resolution of a module:

- the *alignment procedure*. Since the silicon modules have not been installed on the beamline perfectly aligned in an absolute reference frame (as it usually happens), as shown in figure 4.1(a), an offline alignment procedure has to be performed. The alignment procedure was based on the translation of the coordinate system of the D2-D4 detectors with respect to the D1 one (figure 4.1);

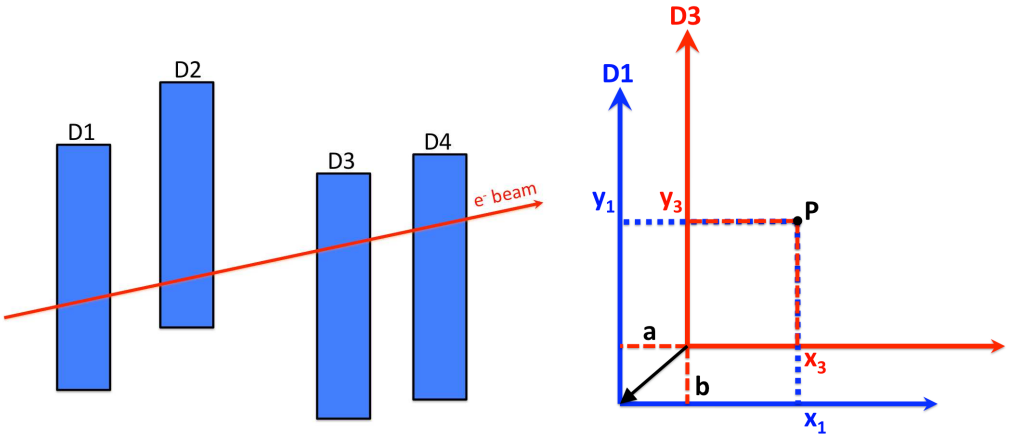

(a) (b)

Figure 4.1: a) The silicon detector alignment; b) example of the D1-D3 modules alignment.

- the *residual method*. Referring to figure 4.2 it consists in the following steps:
  - the reference detectors (i.e. D1 and D3) have been placed at the $z1$ and $z3$ positions along the beamline;
  - the trajectory of the particle has been reconstructed by the reference modules and projected on the D2 detector using the following formulas:

$$\begin{aligned} xproj &= xtan31 * (z2 - z1) + xpos1 \\ xtan31 &= \frac{xpos3 - xpos1}{z3 - z1} \end{aligned} \tag{4.1}$$

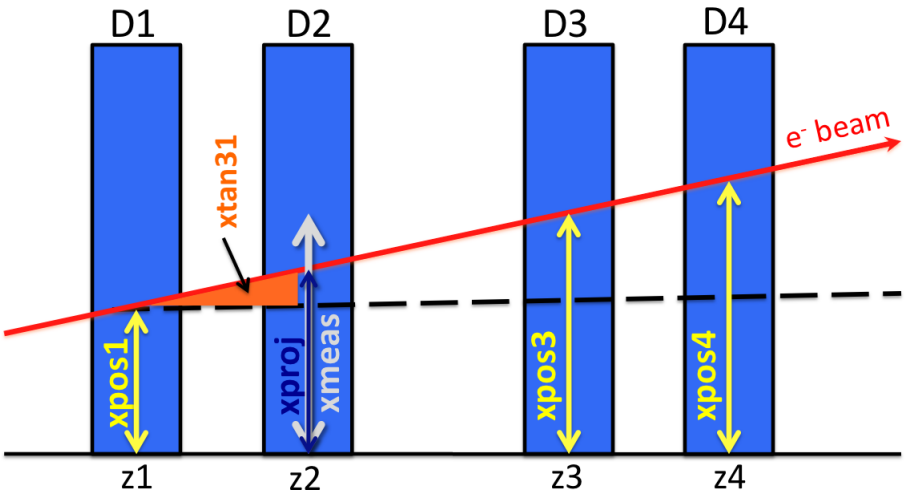

Figure 4.2: Schematic view of the residual method.

where $xtan31$ defines the tangent of the angle between the two reference detectors;

– the *residual* is defined as the difference between the position reconstructed on the D2 module by the two reference detectors ($xproj$) and the one measured ($xmeas$) directly by the D2 module itself:

$$xres = xproj - xmeas \tag{4.2}$$

– the obtained distribution has been fitted with a Gaussian function; the sigma value of the distribution represents the spatial resolution.

4.1.1 The spatial resolution results

The residual distributions for the D2 module have been obtained by using the method explained above. The following distributions have been calculated:

- the horizontal residual (x direction measured by the junction side) using D1-D3 (figure 4.3) as reference detectors. The spatial resolution is σ_x=4.62$\pm$0.01 μm;
- the vertical residual (y direction measured by the ohmic side) using D1-D4 (figure 4.4) as the reference detectors; in this case it was not possible to calculate the residual with the D1-D3 pair given the behavior observed on the D3-y module already discussed and shown in figure 3.35. The spatial

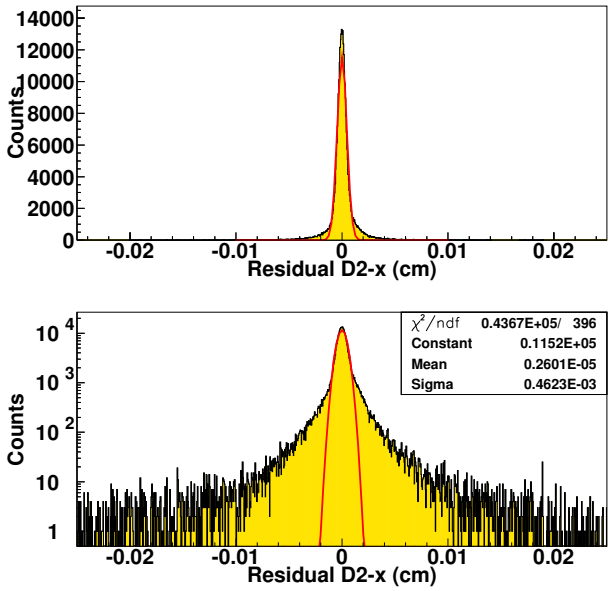

Figure 4.3: The horizontal residual distribution of the D2 module in linear (top) and logarithmic scale (bottom). The spatial resolution is σ_x=4.62$\pm$0.01 μm.

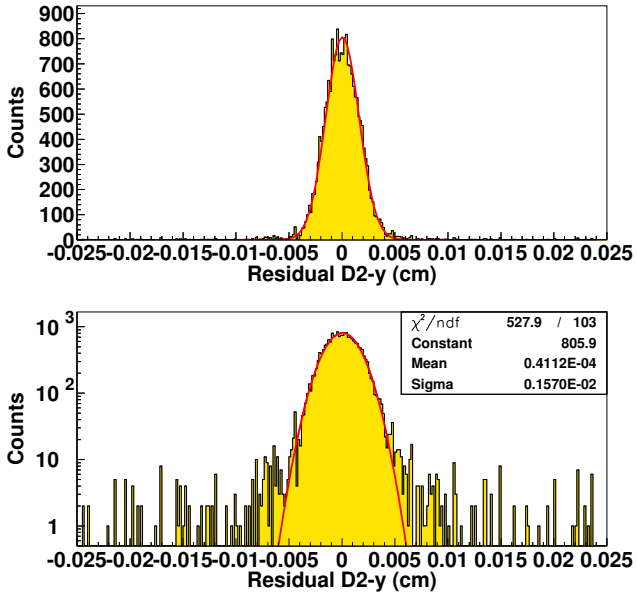

Figure 4.4: The vertical residual distribution of the D2 module in linear (top) and logarithmic scale (bottom), computed with the D1-D4 reference detectors. The spatial resolution is σ_y=15.70$\pm$0.05 μm.

resolution in this case is σ_y=15.70$\pm$0.05 μm. This value is larger than what expected because of two problems:

1. during the data taking one of the adjustable parameters of the ASIC (the "delay on" bit) was set to 1 and this led to an uncorrect sampling of the signal on the ohmic sides;
2. the particle charge is not equally shared among the strips on the ohmic side of the D1 module which is used to evaluate the residuals. This behavior can be observed by considering the distributions of figure 4.5 which are: the pull of the strip with the maximum signal (from now on maximum strip) (red) and the pull of the strip on the right (black) and on the left (blue) of the maximum one. As will be discussed in the next section, if the distributions of the pull of the right and left strip were the same, the charge would effectively be equally shared among these two strips; but this is not the case. Moreover, the pull distribution of the left strip has the same behavior of the one of the maximum strip but with smaller values. This situation suggests that a certain quantity of the signal has been shifted in the left strip. The spatial resolution gets worse because in practice it is like having a detector with a 100 μm readout pitch.

A cross check with a 50 μm pitch single side microstrip detector (FBK-irst), which has the same pitch of the INSULAB module ohmic side, has been performed in order to study this behavior as a function of the clock frequency values (1.25, 2.5 and 5 MHz); the spatial resolution has been evaluated with the residual method: this study has shown that the resolution gets worse of $\sim$70$\%$ when using a 5 MHz clock, thus the real ohmic side spatial resolution can be expected to be around 9 μm. The vertical position resolution will be measured again in the next beamtest.

4.2 The η variable and its distribution

A fundamental aspect in microstrip detectors is the study of the η *distribution* which consists of a non-linear interpolation between the pulse height of the two neighbouring strips (indicated in the following as PH_{right} and PH_{left} respectively) of the one with the largest signal (PH_{high}):

$$\begin{aligned} \eta_{right} &= \frac{PH_{high} - PH_{right}}{PH_{high} + PH_{right}} \\ \eta_{left} &= \frac{-PH_{high} + PH_{left}}{PH_{high} + PH_{left}} \end{aligned} \tag{4.3}$$

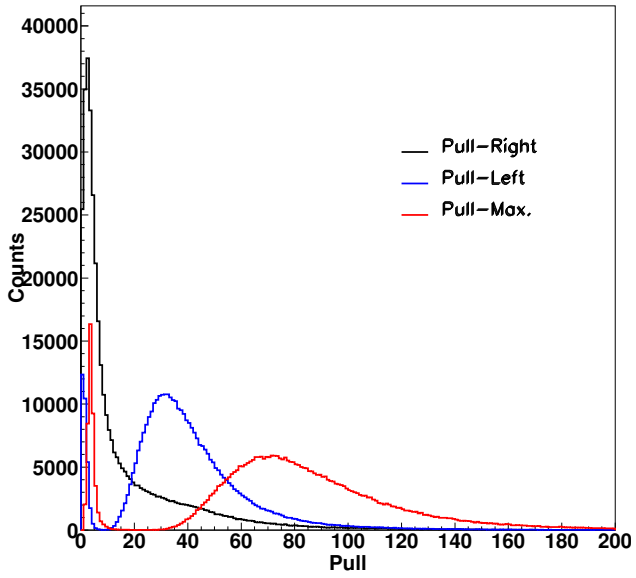

Figure 4.5: The pull distribution of the maximum strip (red) and of the right (black) and left (blue) strip.

The main feature of this distribution is the presence of peaks which means that the charge division is far from being linear, otherwise the distribution should be flat. The non-linearity is due to the width of the diffusion cloud [58]. For tracks crossing the detector at 0° the charge spread is dominated by diffusion; the width of the diffusion cloud is due to the detector parameters such as the thickness, the resistivity and the applied voltage. For a typical 300 μm thick silicon microstrip detector, fully depleted and with a resistivity of a few kΩ·cm, the diffusion cloud is approximately 5-10 μm [58]. Therefore the cloud is smaller than the pitch in most of the common microstrip detectors and in the INSULAB telescope too.

If every strip is readout (like in the ohmic side of the INSULAB modules), two different regions can be distinguished (figure 4.6): the region where the strip is implanted (A region) and the one between two neighbouring strips (B region). If a track crosses the detector in the middle of the B region (dashed line) the charge gets shared between the two strips (i.e. $PH_{right} \simeq PH_{left}$) and therefore the η value is 0; by contrast if it crosses the detector about 10 μm away from the strip edge (A region), most of the charge will be collected by one strip. In this region the η distribution will assume a value close to -1 or +1 because all the charge is deposited on the left or right strip respectively. The peculiar shape of the η distribution is due to the detector characteristics:

- the positions of the lateral peaks in the distribution are related to the capac-

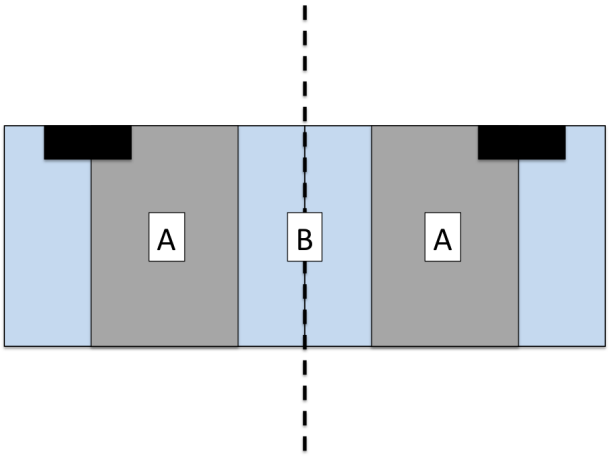

Figure 4.6: The A and B regions: the dashed line in the B region represents the border between the two strips.

itive coupling of a strip to the adjacent ones: the largest the coupling, the farthest the peaks are from -1 and +1 (moving towards 0), since the fraction of transferred charge increases;

- the charge diffusion and the noise tend to fill up the distribution between the two outermost peaks, leaving however the number of peaks unchanged.

If however a floating strip is introduced (like in the junction side of the INSULAB modules), the peaks at η=-1 and η=+1 remain unchanged and a new peak at η=0 appears, corresponding to the intermediate floating strip.

Figure 4.7 presents the η distribution of both sides of a INSULAB module (D4). On the junction side the distribution is symmetric; the large peak centered on 0 is due to the floating strip. The lateral peaks are around $\pm$0.7. On the ohmic side, the η distribution is not completely symmetric because the peak at +0.7 is smaller than its corresponding negative one. The peaks position however remains unchanged with respect to the one on the junction side. This behavior is due to the fact that the capacitive coupling among the strips is the same on both sides.

The η distributions of figure 4.7 represent the ideal case in which the behavior is symmetric. It can happen that there is a problem related to the sampling of the signal when increasing the readout clock rate: if it is performed in the wrong place the symmetry of the η distribution is lost. This can happen when the RC shape of the signal, determined by the NE592 and by the optocoupler board (in the ohmic case), is too slow with respect to the digitizing clock. In this case the measured pulse height may be not the real charge content of the strip and therefore an error on the impact point position evaluation is introduced. Figure 4.8 helps

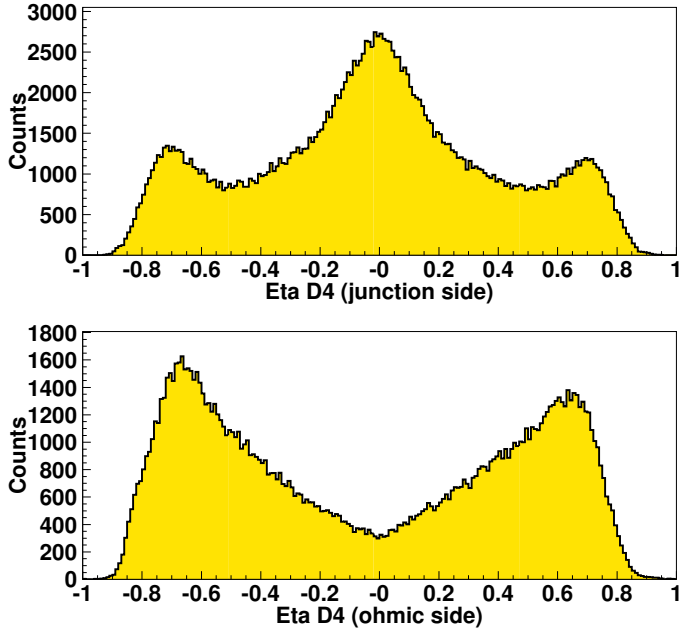

Figure 4.7: The η distribution on both sides of the D4 module using a cluster composed of two readout strips.

to understand the concept. The red line shows the "ideal" shape of the signal for three strips in which the particle has released its energy, while the blue line is the "real" shape of the signal (a RC shape). If the sampling is performed in correspondence of the green crosses, the signal is underestimated (the first two strips) or overestimated (the third strip). Therefore the sampling should be performed in correspondence of the dashed lines where the signal has reached its maximum value.
In order to understand this behavior, a calibrate input signal has been sent to one channel (turning off the others) on the junction side of a module and the multiplexed analog output has been studied for different clock values (figure 4.9); the output signal is shown in red while the clock signal in black. The sampling is performed in correspondence of the rising edge of the clock signal, as indicated by the green crosses; the analyzed clock frequencies f are:

- f=1.25 MHz (figure 4.9(a)). The sampling is performed in the correct position, thus at the maximum of the signal and at the end of the RC shape;
- f=2.5 MHz (figure 4.9(b)). In this case the clock signal is faster than the RC signal shape; in fact the sampling (first cross) is not at the maximum of the signal. Moreover, the second cross, which corresponds to the sampling

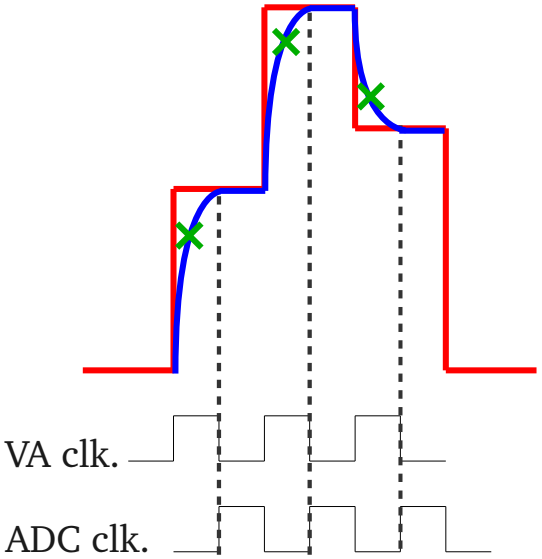

Figure 4.8: The red line indicates the "ideal" shape of the signal for three strips, while the blue line the "real" one. If the sampling is performed in correspondence of the green crosses the signal is underestimated for the first two strips and overestimated for the third one; the sampling is correct if it is performed in correspondence of the dashed lines, at the end of the RC shape, when the signal itself is stable.

of the following channel, collects a small quantity of signal belonging to the previous channel;

- f=5 MHz (figure 4.9(c)). The situation changes dramatically: the clock signal is much faster than the RC shape of the signal. The output signal of a channel is spread on three clock pulses generating a cluster composed of three strips and thus introducing a bias in the position reconstruction.

The η distribution of figure 4.7 has been obtained with a correct sampling of the output signal: the clock used in this case was 1.25 MHz. The pull distributions of the strips adjacent to the one with the maximum signal (figure 4.10) have been analyzed: on the junction side they are similar because the η on that side is symmetric; on the ohmic side they are not properly similar, in fact the peaks in the η distribution are not perfectly symmetric.
An example of a non correct sampling, which makes the distribution asymmetric, is shown in figure 4.11(a); in this latter case f was 5 MHz, therefore the clock

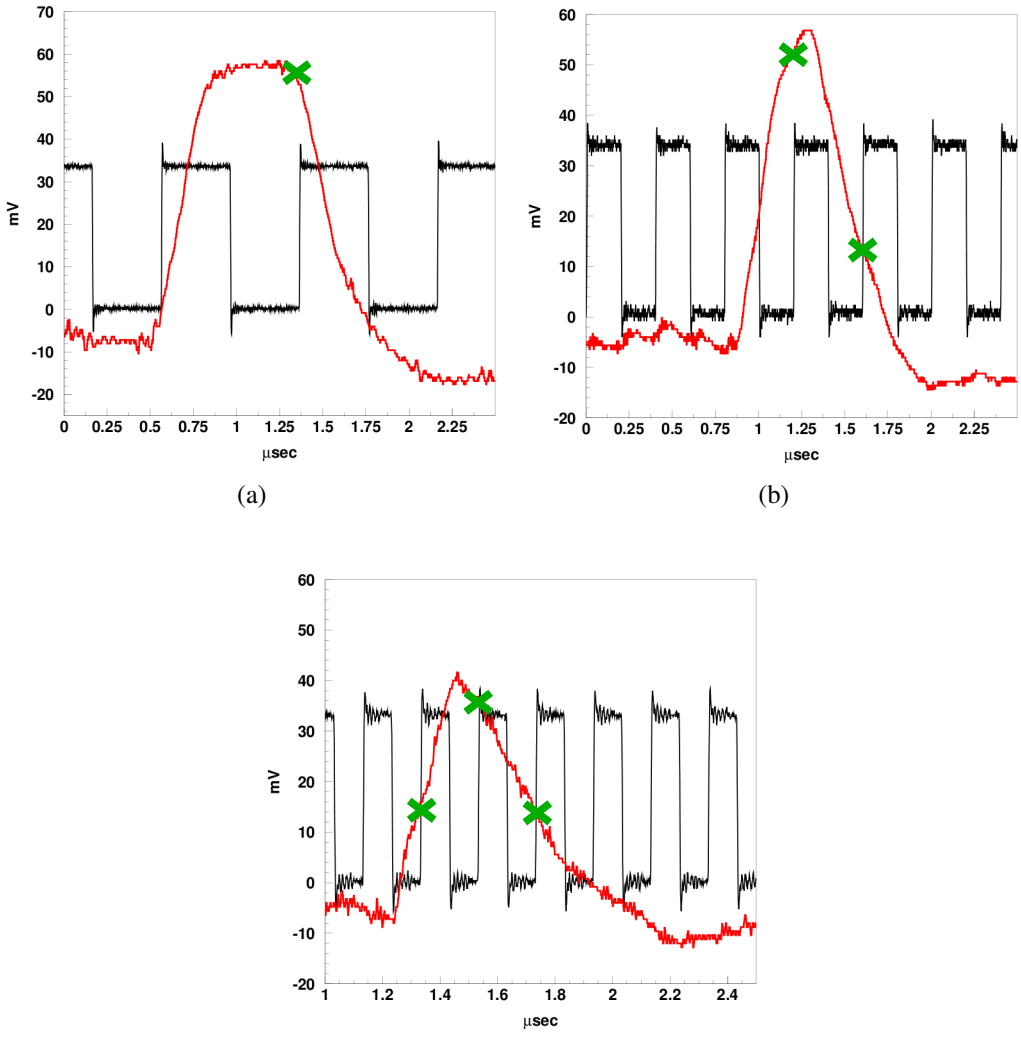

Figure 4.9: The signal shape of a single channel (in red) on the junction side of a module for different clock frequencies (in black): a) 1.25 MHz b) 2.5 MHz and c) 5 MHz.

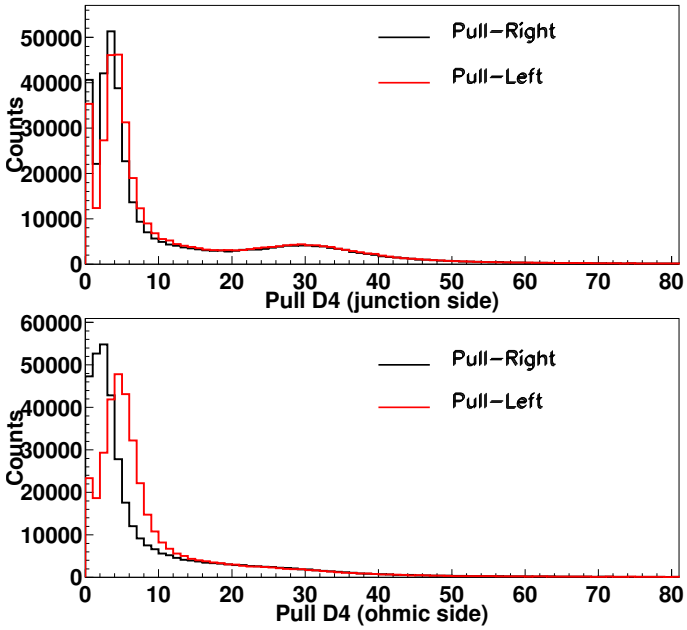

Figure 4.10: Pull distribution for the right (in black) and for the left (in red) strip with respect to the one with the maximum signal.

signal was too fast with respect to the RC shape of the signal. In this case the symmetry of the η distribution is lost (for the reasons described above) as well as the pull distributions of the strips adjacent to the one with the maximum signal (figure 4.11(b)).

4.3 The η correction

The position resolution (section 4.1) has been computed using the impact positions found with the center of gravity method (equation 3.2). As shown in the previous section, the charge collected by the readout strips follows a Gaussian distribution with a FWHM of about 10 μm; although the COG method is a good approximation for a uniform charge distribution, it is inadequate for a Gaussian one [47]. This effect has been shown with the η distribution (figure 4.7) which indicates that the position of the particle is not equiprobable inside the strip.
Therefore considering a non-linear method, the η algorithm, which takes into account the actual shape of the charge distribution, the spatial resolution can be improved. This analysis has been performed for the junction side of the D2 module considering the one cluster events in which the clusters are composed of two

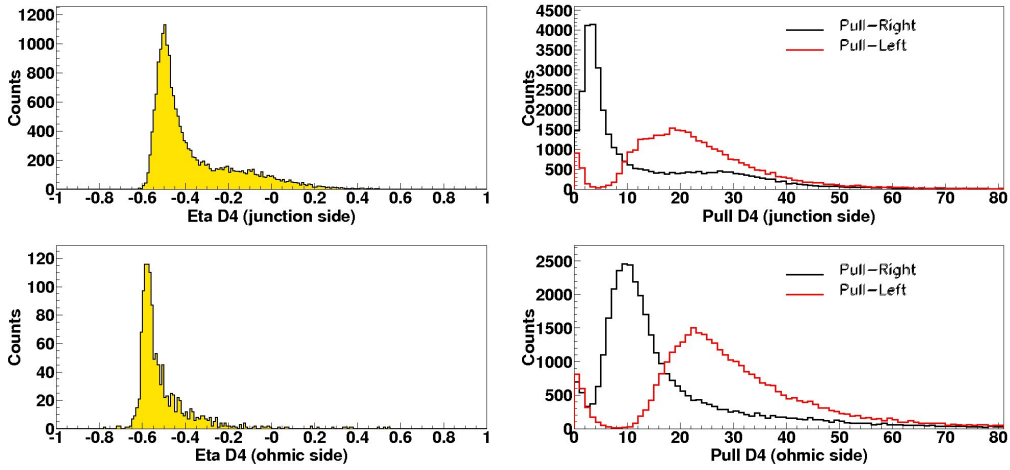

(a) (b)

Figure 4.11: Readout clock of 5 MHz: a) the η distribution and b) the pull distributions for the strips surrounding the one with the maximum signal.

contiguous strips.
This is a reasonable approximation because, for small incident angles, only one or two strips collect the whole charge generated by the ionizing particle (figure 3.19(a)). The correct particle position can be obtained in the following way:

$$xpos = x_{left} + f(\eta) \cdot p \tag{4.4}$$

where x_{left} is the position of the left strip in the pair (figure 4.12) and p the readout pitch. The $f(\eta)$ function is the η cumulative probability distribution function; it

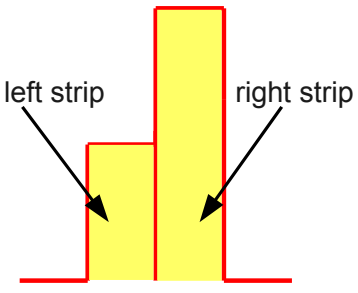

Figure 4.12: Schematic view of the left and right strip of the cluster.

can be estimated as [80]:

$$f(\eta) = \frac{\int_{-1}^{\eta} (\mathrm{d}N/\mathrm{d}\eta^{'})\,\mathrm{d}\eta^{'}}{\int_{-1}^{1} (\mathrm{d}N/\mathrm{d}\eta^{'})\,\mathrm{d}\eta^{'}} \tag{4.5}$$

where $\mathrm{d}N/\mathrm{d}\eta^{'}$ represents the experimental η distribution which is shown in figure 4.13 for the module under study. This method is known in literature as *the η algorithm*.

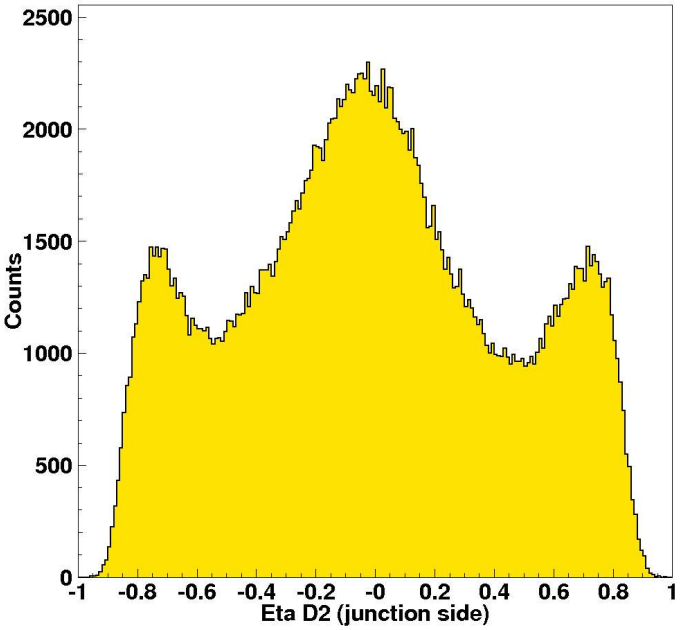

Figure 4.13: The η distribution of the D2 module (junction side).

The procedure for the residual correction using the eta distribution consists in the following steps:

- the positions calculated with the COG method have been rescaled to one strip as shown in figure 4.14 (top) where 0 μm is the center of the first readout strip and 50 μm is the center of the nearby one; the position corresponding to 25 μm is the center of the floating strip. As expected, this distribution is similar to the η one;

- the integral of equation 4.5 has been calculated integrating the eta distribution and normalizing the result;

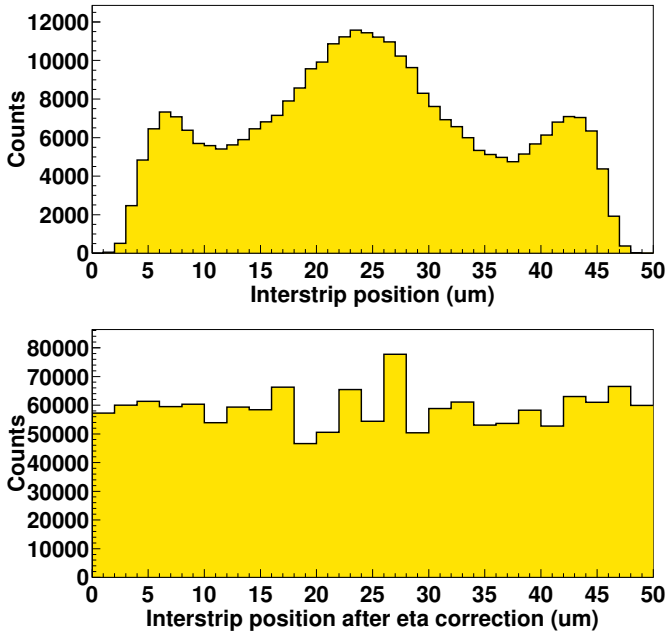

Figure 4.14: The impact point positions rescaled to the strip dimension a) before and b) after the η correction.

- the corrected positions have been recomputed using equation 4.4. The result is presented in figure 4.14 (bottom). As can be seen, the dependence on the position has been reduced: this distribution is flat if compared to the top one;

- the residual distribution has been recomputed by using the correct positions obtained from equation 4.4. The new spatial resolution is σ_x=5.71$\pm$0.01 μm (figure 4.15), therefore it is worse than the one obtained with the COG method. Furthermore, as shown in the logarithmic plot, there are asymmetric tails in the residual distribution even if they are much less populated than the original ones (figure 4.3);

- the new residuals have been plotted as a function of the corrected interstrip position in order to evaluate their behavior (figure 4.16(a)): the correction for the η distribution introduces a further dependence on the position, represented by the slope of figure 4.16(a);

- to evaluate this behavior the plot of figure 4.16(a) has been projected in 50 vertical slices; each slice has been fitted with a Gaussian function, obtaining a set of values for the mean and the sigma. Using this slicing method, the

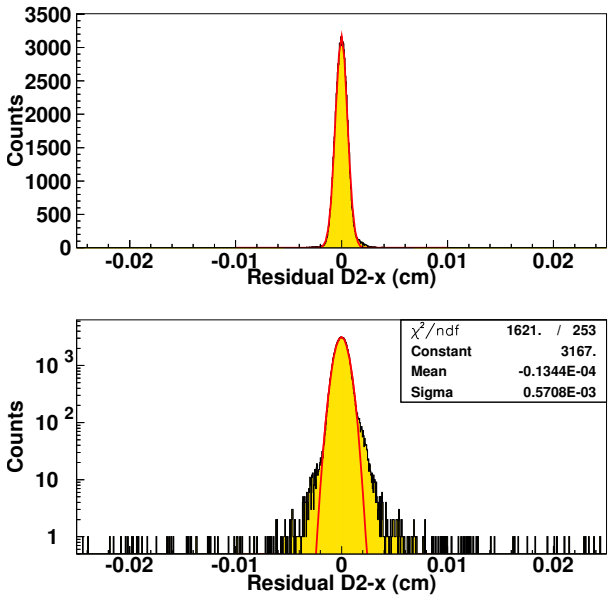

Figure 4.15: The residual distribution of the junction side of the D2 module in linear (top) and logarithmic scale (bottom) after the η correction. The spatial resolution is σ_x=5.71$\pm$0.01 μm.

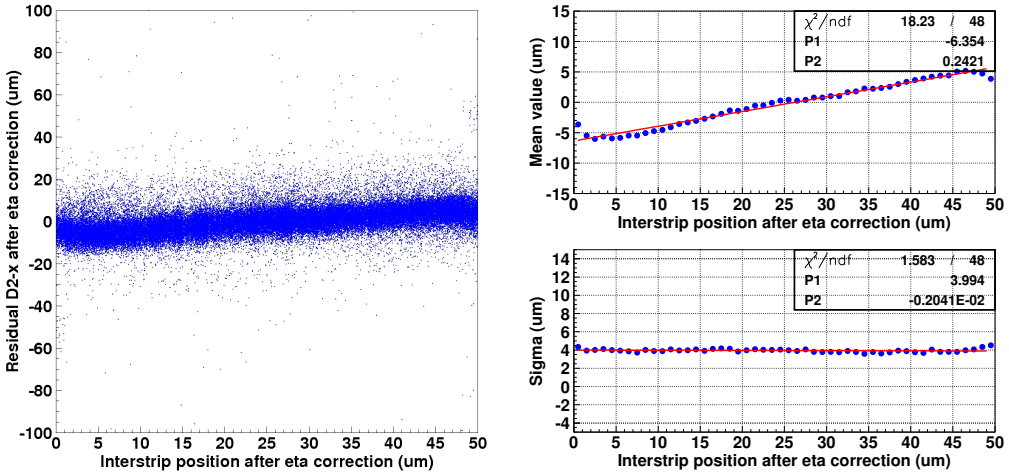

(a) (b)

Figure 4.16: a) The residuals as a function of the corrected interstrip positions; b) the position resolution mean (top) and sigma (bottom) values as a function of the corrected interstrip positions.

following plots have been produced:

- the position resolution mean value as a function of the interstrip position (after the η correction), presented in figure 4.16(b) (top). The points have been fitted with a straight line; the P2 parameter, whose value is 0.2421 represents the slope of the straight line;
- the sigma value as a function of the interstrip position (after the η correction), presented in figure 4.16(b) (bottom). This plot shows that the sigma of the residuals remains constant at 3.99$\pm$0.01 μm;

- the slope has been straightened by introducing an additional correction to the residuals. The obtained result is presented in figure 4.17(a). The same considerations can be made looking at the plot of figure 4.17(b) (top), computed with the same slicing method described above: in this case the P2 value is 0.12×10^{-2}. The sigma behavior (figure 4.17(b) (bottom)) remains practically the same of figure 4.16(b) (bottom);

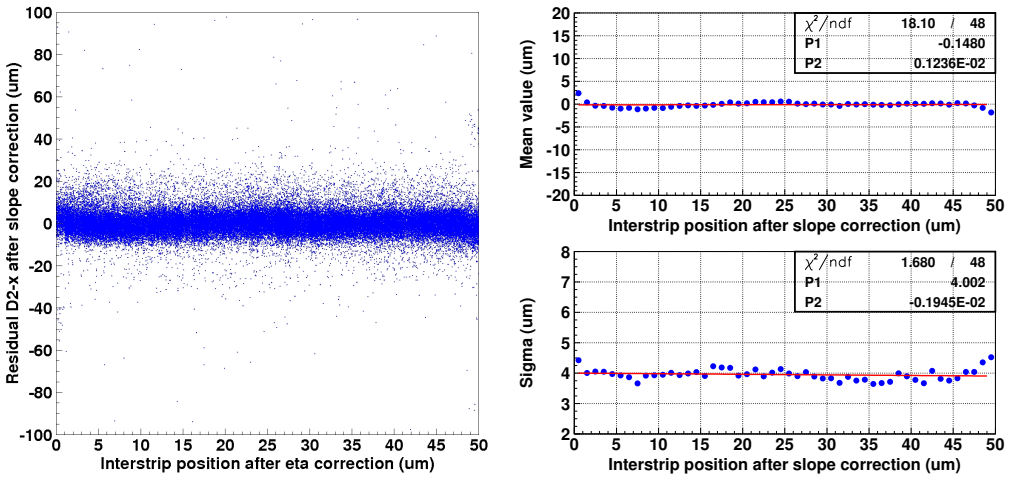

(a) (b)

Figure 4.17: a) The residuals as a function of the corrected interstrip positions after the slope correction; b) the position resolution mean (top) and sigma (bottom) values as a function of the corrected interstrip positions, after the slope correction.

- the residual distribution has been then recomputed (figure 4.18) and the new value is σ_x=4.16$\pm$0.01 μm. It must be noted that the asymmetric tails are still there and this is due to the non 100% symmetry of the starting η distribution. They are anyway much smaller than the ones in figure 4.3.

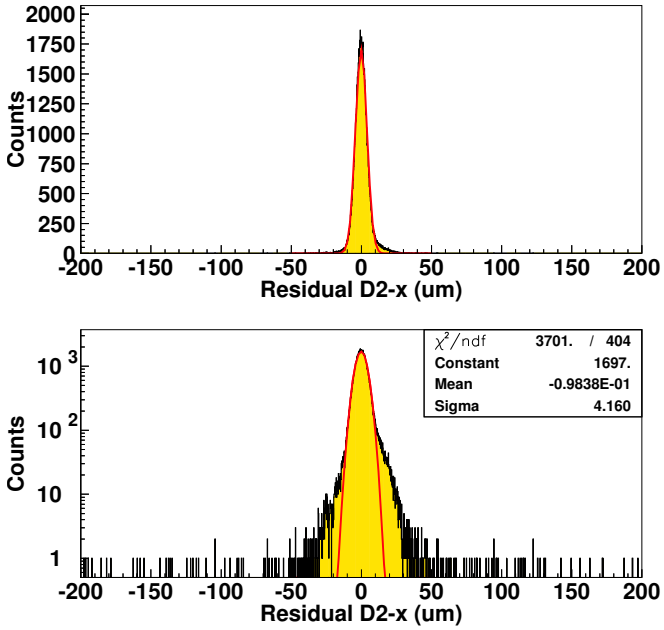

Figure 4.18: The residual distribution of the junction side of the D2 module in linear (top) and logarithmic scale (bottom) after the η and the slope correction. The spatial resolution is σ_x=4.16$\pm$0.01 μm.

4.4 Charge sharing

As explained in the previous sections, in silicon microstrip detectors the capacitive coupling of neighbouring strips causes a charge sharing among them; even when the whole charge drifts inside a single strip, a small fraction of the signal may be seen on the neighbouring strips. When the main cause for charge sharing is the capacitive coupling between strips, the value of this fraction depends only on the interstrip and strip-to-backplane capacitances. Figure 4.19 presents a photo of the metal strips both for the junction (figure 4.19(a)) and ohmic side (figure 4.19(b)) of a INSULAB module: on both sides its width is in the range of 10-12 μm.

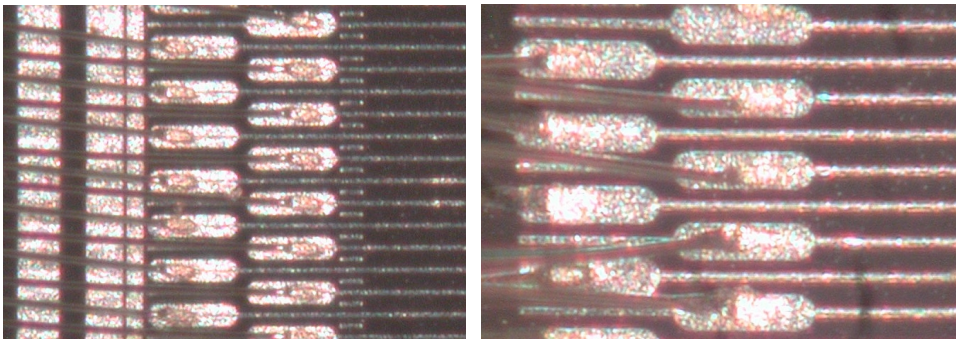

(a) (b)

Figure 4.19: Top view of the metal strips a) for the junction and b) ohmic side of a INSULAB module.

From the data analysis point of view, to study the charge sharing among the strips the pulse height of the strip with the maximum signal as a function of the hit position in the strip itself has been considered[1] (figure 4.20).
The top plot in figure 4.21 presents the charge sharing evaluation using the COG positions; since this method does not consider the dependence of the charge from the particle impact position inside the strip, the "real" charge sharing, calculated after having applied the η algorithm (section 4.3), has been computed.

The same slicing method described above has been applied in order to compute the amount of charge detected by each readout strip as a function of the particle position. In this case each slice (figure 4.21) has been fitted with a Landau-like function in order to evaluate the most probable value of the slice itself.
When the particle crosses the center of the floating strip, the resulting collected charge (given by the sum of the charges collected by the readout strips on the side

[1] Note that 0 and 50 μm are the centers of two nearby readout strips, while 25 μm the center of the floating one.

of the floating one) is 70% of the charge collected when the particle crosses a readout strip.

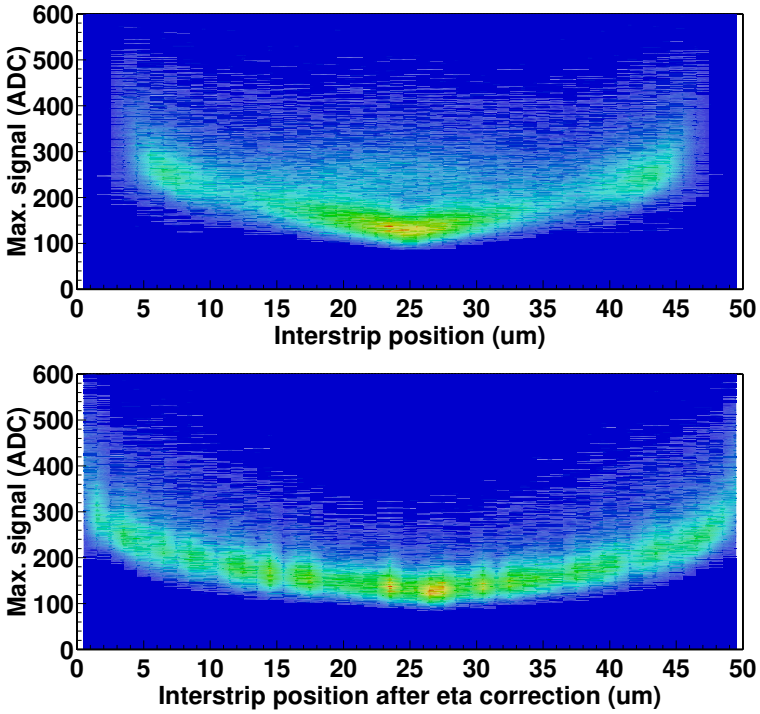

Figure 4.20: The charge sharing evaluation using a) the standard positions calculated with the center of gravity method and b) the ones computed after the η correction.

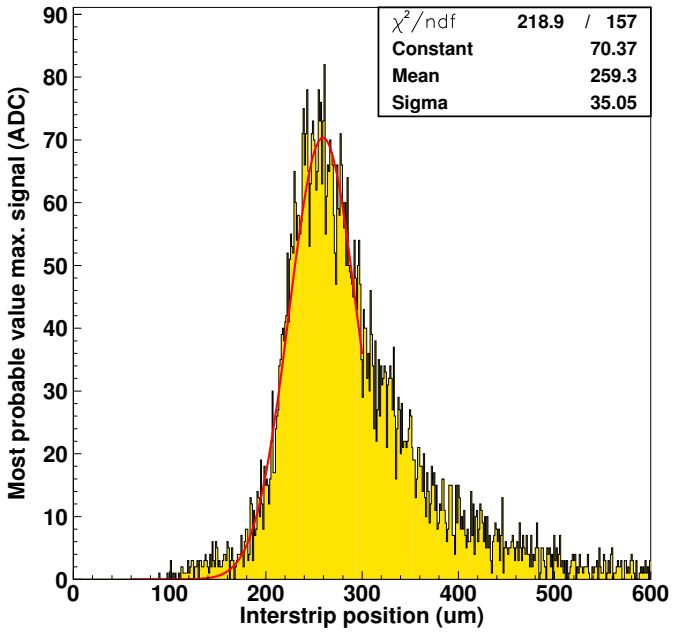

Figure 4.21: An example of a slice fitted with a Landau function.

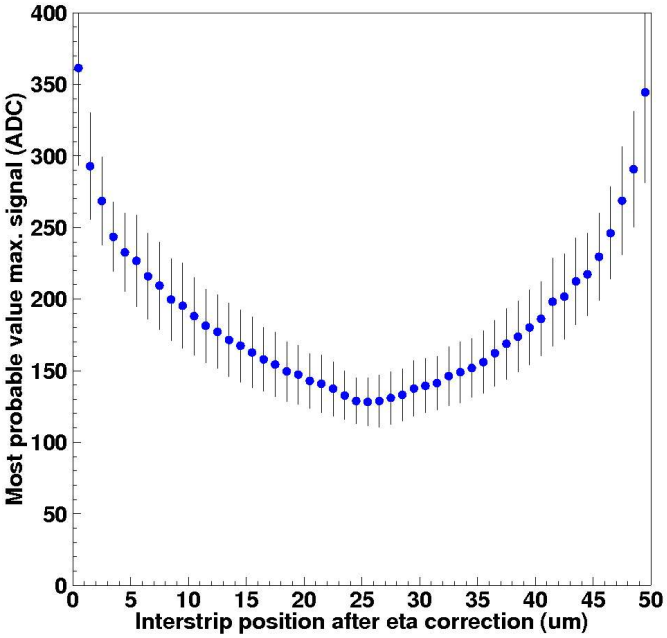

Figure 4.22: The charge sharing distribution using the positions computed after the η correction.

Conclusions & Outlooks

In many experiments the reconstruction and precise determination of the particles trajectory is essential to understand and analyze the physical processes. The tracking detectors are typically built using position sensitive detector elements exploiting the signals particles induce in the detectors when interacting with the detector material. The individual measurements are then used to reconstruct the particle trajectory.
To measure the position of charged particles several technologies have been developed, from the photographic emulsions of the 1930s to the bubble chambers of the 1960s, to arrive to the gaseous detectors and the semiconductor ones, nowadays widely used in colliding beam experiments, allowing a precise tracking and even vertexing. In 1980 Kemmer introduced the planar technology for the production of silicon detectors. This technique allowed the segmentation of one side of the junction and the use of the signals recorded on these segments to determine the particle hit position. The improvement from macro-segments (strips) to microstrips was straightforward and these devices became soon a common tool in high energy physics.

This thesis work has dealt with the study of a high resolution tracking system (the INSULAB telescope) and its new fast readout electronics, built to comply with the high rate of the CERN North Area extracted beams. The INSULAB telescope features four independent modules; each of them consists of a double side high resistivity 300 μm thick silicon microstrip detector with a sensitive area of 1.92$\times$1.92 cm^2 for a total of 384 strips, readout by three VA2 ASICs. The detector junction side has a p^+ strip every 25 μm and a readout pitch of 50 μm, therefore a one floating strip scheme is implemented. The ohmic side has a n^+ implantation every 50 μm, perpendicular with respect to the p-side strips.

The telescope has been initially tested with a ^{90}Sr source and the standard readout electronics at the Como laboratory, while the commissioning of the new readout electronics has been performed in June 2012 at the CERN SPS H4 line, with a 150 GeV/c electron beam.

The standard DAQ system was based on off-the-shelf ADCs (the V550 ADCs by CAEN) which can work in zero suppression allowing to obtain a maximum

DAQ rate of 3 kHz. The main disadvantage of this system is that the data are readout from the VME and written on the PC at each event. This condition is not ideal when working with a pulsed beam such as the ones of the CERN extracted beamlines where typically the spill lasts 8 sec with a cycle of 45 sec.

The new readout system has been designed in order to improve the DAQ rate; the idea is to store the events in dedicated memories on custom VME boards (VRB) and to transfer them to the PC during the interspill period. Each VRB is programmable through an Altera EP2C50 FPGA with 50k cells and 581 kbit of internal RAM; the board has 4 Mword of 32 bit RAM. The interface between the VRB and the detector module is performed by an ADC board; since it has been designed to be placed near the detetector the digitization of the data from the ASICs is performed *in situ*, avoiding the problem of long cables that led to an increase of noise in the old electronics. The new readout system has allowed to reach a DAQ rate of 6 kHz compared with the 3 kHz of the standard electronics.

From the data analysis point of view, the event selection has been performed considering only the single track events, thus the ones in which only one single particle crosses the double side microstrip detector. To identify the position of the cluster (that is the group of contiguous strips detecting the energy deposited by the particle), the center of gravity (COG) method has been applied. The dead or noisy channels have been identified and excluded from the analysis. The cluster pulse height has been evaluated in order to study the cluster SNR which is larger than 50 in all the modules.

The most important feature of a tracking system is its capability to reconstruct with a high resolution the crossing position of the particle. This capability is described by the spatial resolution. The spatial resolution is defined as the rms of the residual distribution, that is the difference between the real particle impact point and the reconstructed position. For the junction side, it resulted to be σ_x=4.62$\pm$0.01 μm while for the ohmic one σ_y=15.70$\pm$0.05 μm mainly because of a non correct sampling of the signal analog peak due to the sampling clock rate which was too fast with respect to the ASIC output buffer speed. This results in a bias in the charge sharing of contiguous strips which in turn becomes a bias on the position.

A detailed study of the charge sharing distribution among the strips that compose the cluster has been performed using the η distribution, a non-linear interpolation between the pulse height of the two neighbouring strips of the one with the maximum signal. Since the COG method does not consider the dependence of the charge sharing from the particle impact position inside the strip, the η algorithm has been applied to recompute the correct positions; using this method the horizontal residuals have been recalculated and the spatial resolution has improved to σ_x=4.16$\pm$0.01 μm.

The telescope and its new fast readout system have been installed on the H8

beamline as a part of the experimental setup for the study of the bent crystals in the COHERENT experiment. As far as the future steps are concerned the telescope will be equipped with a gigabit link (for the transmission of the data on cable or optical fiber with a maximum rate of 1.25 Gbit/s) to improve the connections between the readout and frontend blocks reducing the number of cables between the detectors and the VME crate. A new set of telescope modules will be assembled with self-triggering ASICs (VA1TA by Gamma Medica) with the parallel readout of the three ASICs; the multiplexing of the data in fact is the most time consuming part of the readout cycle. Preliminary tests have been already performed in this direction as described in the appendix of this thesis.

Appendix A

Tests with the VA1TA ASICs

Several characterization tests have been performed on single side silicon microstrip detectors readout by self-triggering VA1TA ASICs [81]. The analog output has been studied as a function of two tunable parameters: the hold and the convert signals. The tests have been performed using two different particle sources: the ^{90}Sr β-source and the cosmic rays.

A.1 The experimental setup

The experimental setup is basically the same for the two tests and is shown in figure A.1. It consists in:

- the silicon microstrip detector under test (section A.1.1);
- a couple of plastic scintillators (described in section 3.2.1.1) used for the trigger generation in the test with the cosmic rays. On the other hand, in the tests performed with the ^{90}Sr source the trigger has been generated directly by the silicon detector, given the β particles are not energetic enough to cross two plastic scintillators and the detector;
- the "standard" data acquisition system (section 3.2.1.2).

A.1.1 The silicon detectors

The two telescope modules under test have been designed by INFN Trieste; the silicon tiles have been manufactured by HAMAMATSU[1]. Each of them consists of two high resolution single side silicon microstrip detectors, assembled one close

[1] http://www.hamamatsu.com

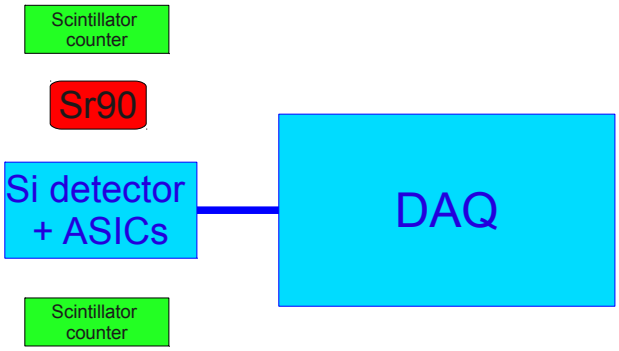

Figure A.1: A schematic view of the experimental setup used for the tests of the single side silicon microstrip detectors. The two plastic scintillators have been used for the trigger generation in the cosmic rays tests, while in the tests performed with the ^{90}Sr source the trigger has been generated by the silicon detector itself.

to the other with the strips oriented perpendicularly; in this way they are able to measure two orthogonal coordinates (x,y). Moreover, a fifth single side silicon microstrip detector of the same type has been tested. Each silicon microstrip detector (figure A.2) is 300 μm thick and has a dimension of 21$\times$21 mm^2 for a total of 384 strips; the physical and readout pitch are 50 μm and no floating strip scheme has been adopted. The detectors are fully depleted with a bias voltage

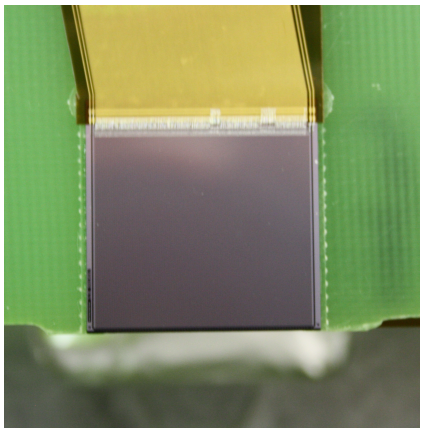

Figure A.2: The single side silicon microstrip detector.

of $\sim$50 V and the average leakage current is of the order of 1.5-2.0 nA per strip. Table A.1 summarizes the general features of these detectors [82].

The readout of each detector is performed by three 128 channel self-triggering VA1TA ASICs. The connection between the detector and the frontend electronics requires the use of a flexible fanout which consists of a 50 μm thick upilex layer

with 5 μm copper lines where about 1 μm of galvanic gold is deposited for the bonding. Two different fanout configurations have been designed. In the first

Number of strips	384
Bulk thickness	300 μm
Detector dimension	21×21 mm^2
Strip pitch	50 μm
Readout pitch	50 μm
Implanted strip width	30 μm
Resistivity	>4 kΩ cm

Table A.1: General features of the silicon microstrip detector used in these tests.

case (figure A.3(a)) the fanout directly connects the strips to the ASIC, while in the second one (figure A.3(b)) the fanout is bent of an angle of 90°. The silicon microstrip detectors are housed inside a metal box with thin aluminum windows together with a part of the frontend electronics consisting of the PCB with the ASICs.

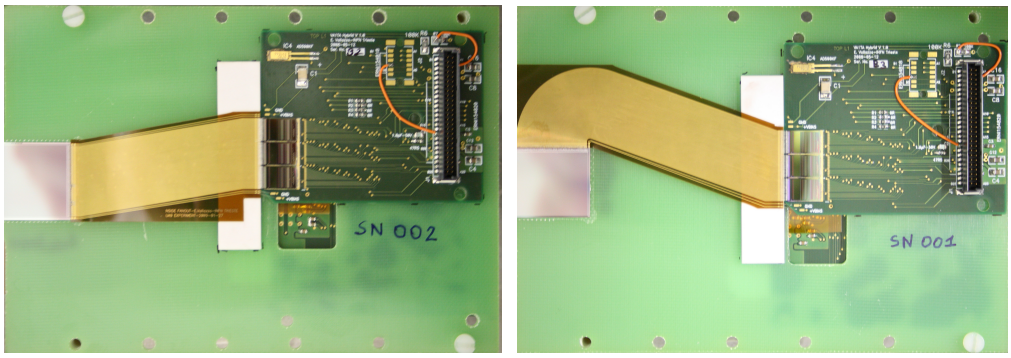

(a) (b)

Figure A.3: The two fanout schemes: a) the “straight” and b) the “bent” one.

A.1.1.1 The VA1TA ASIC

The VA1TA ASIC (Gamma Medica - IDEAS[2]), presented in figure A.4, is a 128 channel ASIC built with the 0.35 μm N-well CMOS technology; its features are summarized in table A.2.
Figure A.5 presents the VA1TA architecture which consists of two parts: the VA and the TA one. The two parts share the same preamplifiers (located in the VA

[2]http://www.gm-ideas.com

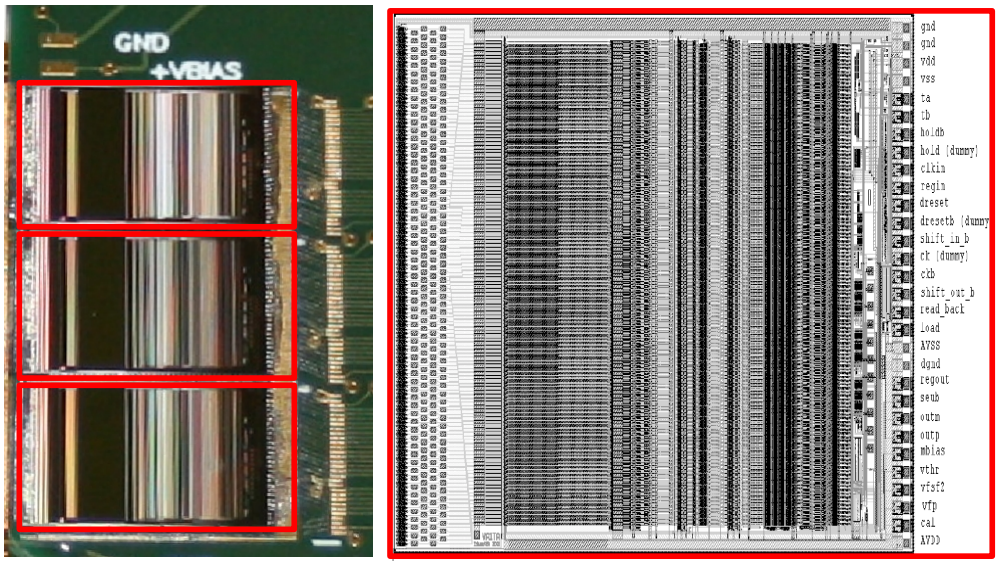

Figure A.4: The three VA1TA ASICs and the layout of one of them.

ENC at 1 μs of peaking time	180 e^- $\pm$7.5 e^-/pF
Power consumption	195 mW/channel
Fast shaper peaking time	75-300 ns
Slow shaper peaking time	300-1000 ns
Dynamic range	$\pm$10 MIPs

Table A.2: Technical features of the VA1TA readout ASIC.

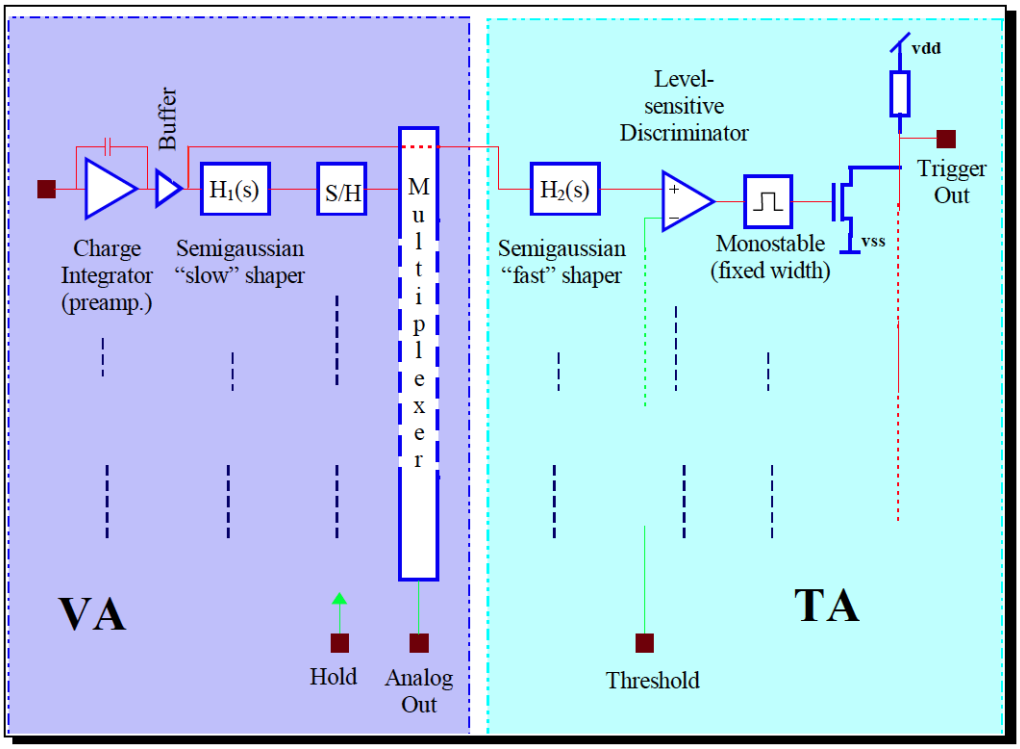

Figure A.5: The VA1TA working principle.

part) and the inputs of the TA part are directly coupled to the corresponding outputs of these preamplifiers. In particular the VA part allows the analog sampling while the TA part the self-trigger generation.
The ASIC channels of the VA part are described in section 3.1.2; each channel of the TA part (figure A.6) includes:

- the charge-sensitive preamplifier shared with the VA part;
- a CR-RC fast shaper with a peaking time that can be set in the range 75-300 ns;
- a level-sensitive discriminator;
- a monostable to generate a fixed width trigger signal. The width of the signal can be set by the user.

The ASIC trigger output is the OR of all the discriminators outputs.

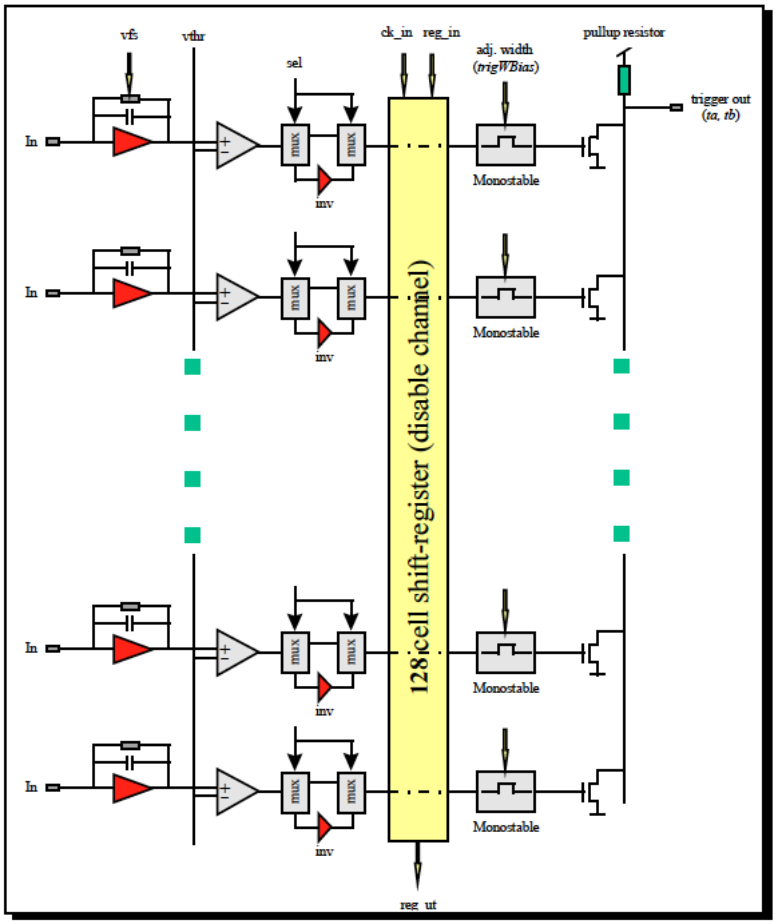

Figure A.6: The TA architecture.

A.1.2 The DAQ system

Figure A.7 presents the DAQ chain used in the tests. The electronics used in this test is the standard one, described in section 3.2.1.2. The trigger signal is generated in two different ways depending on the test:

- by the coincidence signal of the two plastic scintillators for the cosmic ray tests. The PMTs analog signals have been discriminated with a NIM (Nuclear Instrumentation Module) discriminator to be used to produce the coincidence signal for the VME trigger board;

- by the ASIC itself for the ^{90}Sr source tests.

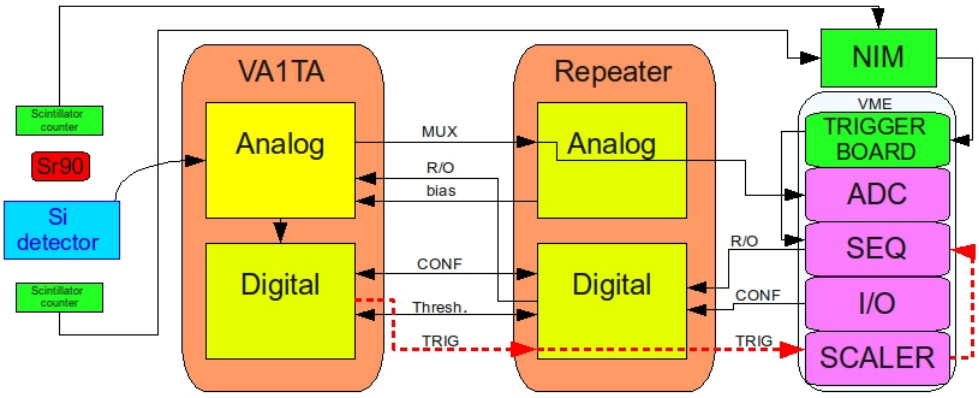

Figure A.7: The DAQ chain used in these tests. The green parts have been used to generate the trigger for the tests performed with the cosmic rays. The red dashed lines indicate that the trigger was generated directly by the VA1TA ASIC for the tests with the ^{90}Sr source.

In both cases the trigger board output is sent to a VME sequencer board to generate the DAQ trigger which is the one starting the readout sequence.

The VA1TA ASIC needs to be configured before being used, therefore a specific mask has to be loaded. Each ASIC is configured through a 680 bits long shift register, presented in figure A.8, which is loaded serially. Thanks to this mask it is possible to set the ASIC main parameters as the peaking time of the fast shaper, the preamplifier gain, the trigger width and the discriminator threshold. The ASIC threshold is set by a global DAC (Digital to Analog Converter) while a fine tuning is possible on a channel by channel basis using dedicated 3-bit trim DACs.

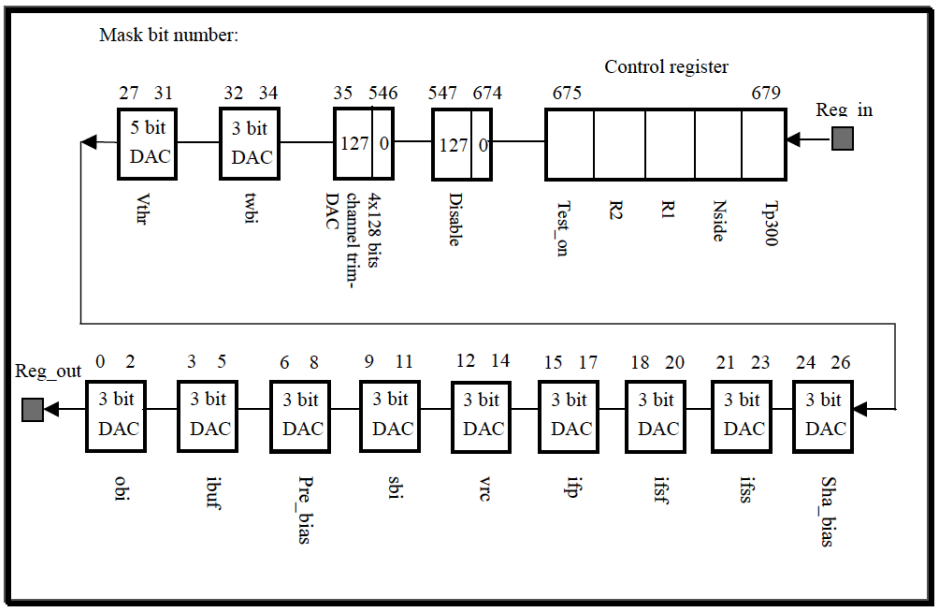

Figure A.8: The sequence of the serial shift register mask; bit 0 is the first bit to be loaded.

A.2 Data analysis and results

The event selection has been performed taking into account only the single track events, that is the events in which only one single particle crosses the microstrip detector. The data analysis procedure is the following:

- acquisition and analysis of the pedestal run (section 3.2.3.1);
- data acquisition and selection of the good events (section 3.2.3.2);
- hold and convert scan with the ^{90}Sr source in order to test the analog performance of the silicon strip detector (section A.2.1);
- tests with cosmic rays with the final configuration for the hold and the convert value (section A.2.2).

A.2.1 The test with the ^{90}Sr source

The first tests on the silicon microstrip detector have been performed with a ^{90}Sr β-source, placed just above the silicon strip detector.
Figure A.9(a) shows the pedestal of one silicon microstrip detector, where the three different regions correspond to the three readout ASICs; figure A.9(b) shows

the noise rms. The black histogram is the global noise rms while the red one the noise rms after the common mode subtraction. This detector in particular has a few noisy strips.

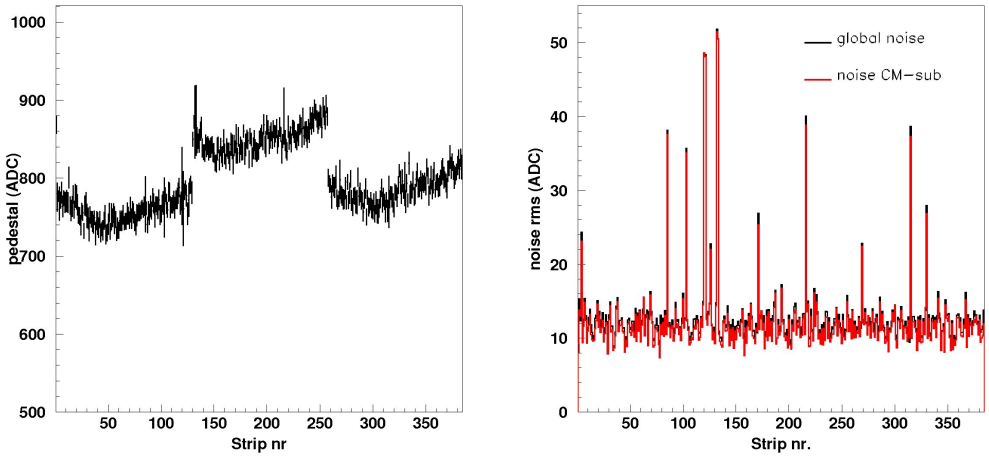

(a) (b)

Figure A.9: a) The pedestal value for each strip of the detector under test; b) the corresponding noise rms (in black) and the noise rms after the common mode subtraction (in red).

The following procedure has been applied to test the electronics:

- a hold scan to evaluate the shape of the analog signal;
- a convert scan to set the delay between the VA1TA clock and the ADC clock;
- the η distribution evaluation to study the charge sharing in the silicon strips.

A.2.1.1 The hold scan

One of the ways to evaluate the analog shape of the signal generated by the VA1TA is the use of the hold scan as already shown in section 3.2.4.1. The hold is defined as the interval between the trigger signal (which is generated by the particle crossing) and the sampling of the signal peak. The concept is explained in figure A.10. The idea is the same of section 3.2.4.1 but in this case the detector is self-triggering and the trigger is generated by the ASIC.
At t=0 the particle crosses the silicon detector and the deposited charge is amplified by the preamplifier. As explained in section A.1.1.1, the VA1TA has two

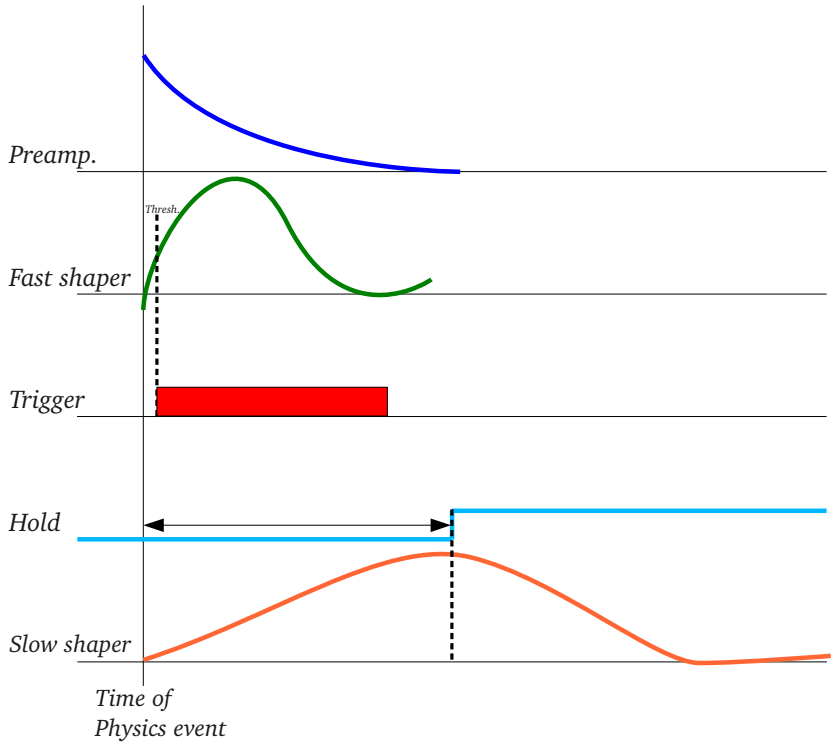

Figure A.10: After the particle passage the signal is amplified by the preamplifier; the trigger is generated when the fast shaper output crosses the discriminator threshold. The hold signal is generated by the data acquisition system to sample the slow shaper output peak.

shapers that have a different peaking time. The fast shaper generates a fast signal with a shaping time in the range 75-300 ns; this is the input of the discriminator. The trigger width has been set to 105 ns; the trigger signal is processed by the VME sequencer which at this point generates the hold delay. The rising edge of the hold signal is the one sampling the slow shaper output. The sampled value is stored to be sent to the ADC during the readout procedure.

Given that the hold value must be set in order to sample the peak of the signal, the shape of the analog signal can be obtained varying the hold interval in the range 0-940 ns, the maximum achievable with this board, and therefore sampling the signal in different places.

To perform the hold scan the procedure described above has been applied to all the silicon detectors under test. The results presented in the following are the ones corresponding to one detector used as an example.
A run has been performed for each of the hold values in the range 100-940 ns (the first two columns of table A.3 show the conversion from the hold values in arbitrary units to the ones in ns). For each hold value the pull of the strip with the maximum signal has been considered and fitted with a Landau function; figure A.11 presents an example of the pull distribution fitted with the Landau function. The three parameters obtained from the fit represent respectively the normalization factor (P1), the FWHM (P2) and the most probable value (P3). The values for the second and third parameter of each fit are summarized in table A.3.

Hold value (A.U.)	Hold value (ns)	par2	par3
0	100	14.93±0.2118	13.92±0.8580E-01
1	144	16.32±0.2234	15.07±0.9218E-01
3	260	17.99±0.2482	16.74±0.1019
5	368	19.67±0.2803	17.58±0.1117
7	484	20.82±0.3022	18.05±0.1183
9	590	21.33±0.3043	17.85±0.1208
11	708	20.74±0.2952	17.34±0.1170
13	820	19.67±0.2865	16.59±0.1120
15	940	18.77 ±0.2719	15.40±0.1085

Table A.3: The first two columns show the conversion from the hold values in arbitrary units to the ones in ns. The FWHM (par2) and the most probable value (par3) of the Landau function obtained for the different hold values are presented.

The most probable values have then been plotted as a function of the hold ones: figure A.12 shows the signal shape reconstruction. The peaking time is located

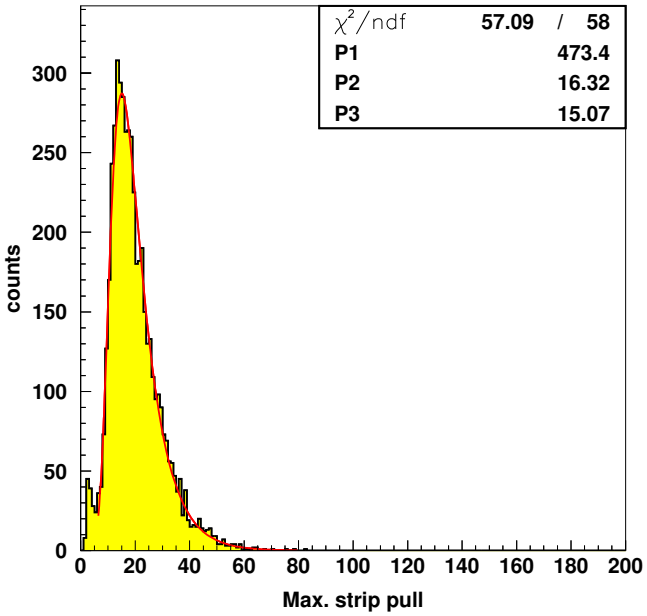

Figure A.11: Pull of the strip with the maximum value fitted with a Landau function.

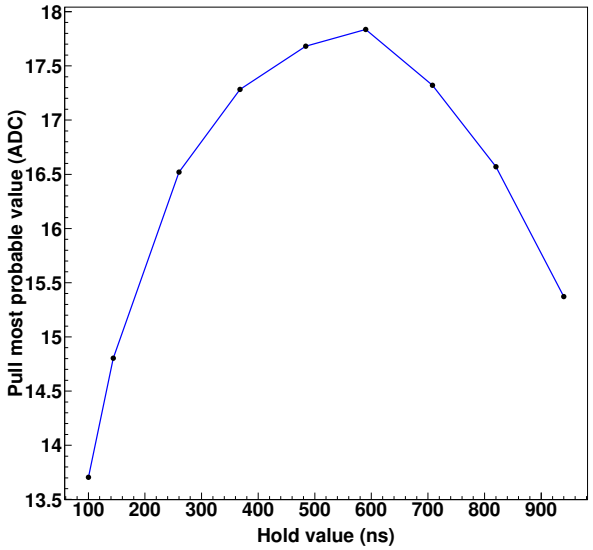

Figure A.12: Hold scan for one of the silicon modules: the shape of the signal has been reconstructed and the peaking time corresponds to a hold value of ∼500 ns.

at ∼500 ns that corresponds to a hold value of 7. Also the other silicon detectors behave in the same way; the final hold value used in the following tests has been set to 7.

A.2.1.2 The convert scan

The analog signal readout is a multiplexed one with a maximum frequency for the clock of 10 MHz; this same clock is also sent to the ADC with an adjustable delay. This latter has to take into account the time that the signal needs to go to the ADC, mainly determined by the cables length; in fact the readout clock has to go from the VME sequencer to the modules and the output back to the VME. This problem has been solved with the new DAQ system (section 3.3.2.1) where the digitization of the data from the ASICs is performed *in situ*.

The convert time allows to choose the exact position in which the signal is sampled when it arrives in the ADC. A pedestal and data run have been performed for each of the convert values in the range 0-140 ns; table A.4 shows the conversion from the convert values in arbitrary units to the ones in ns. To verify the

Convert value (A.U.)	Convert value (ns)
0	0
1	20
2	40
3	60
4	80
5	100
6	120
7	140

Table A.4: Convert values in arbitrary units and the corresponding measured values in ns.

correctness of the sampling the following distributions have been evaluated for each convert value:

- the pull of the strips adjacent to the one with the maximum;
- the η distribution of the cluster.

The pull distributions of the strips surrounding (left and right) the one with the maximum are similar if the signal is sampled in the correct position; otherwise, if the signal is sampled in the uncorrect position it is overestimated or underestimated and thus the two pull distributions are very different. In figure A.13 the pull

distributions of the right strip (in black) and of the left one (in red) are presented: for the convert value equal to 0 (figure A.13(a)) the sampling is correct while for the convert equal to 7 (figure A.13(b)) it is not in the right place.

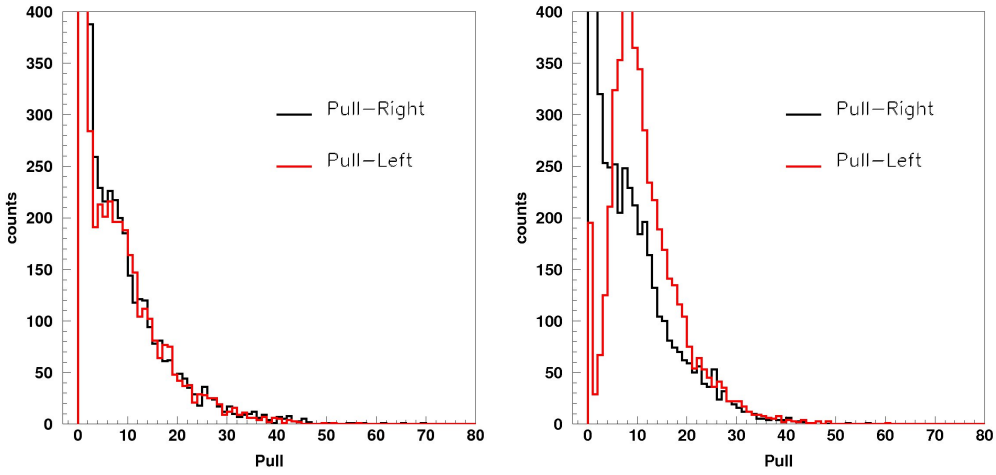

(a) (b)

Figure A.13: Pull distribution for the right (in black) and for the left (in red) strip surrounding the one with the maximum signal. The two distributions are a) similar when the convert value is 0 and b) different when the convert is 7.

Another way to verify the correctness of the chosen convert value is to study the η distribution (section 4.2). Figure A.14(a) presents the η distribution when the convert value is 0:

- in the first case it has been calculated for a cluster with two strips;
- in the second case for a cluster of 3 strips;
- in the third for a cluster of $\geq$2 strips.

As expected, for the cluster with just two strips the distribution is symmetric and it is close to zero due to the capacitive coupling. When the number of strips per cluster increases the η distribution remains symmetric and the peaks get closer and thus become almost indistinguishable.
The non correct sampling of the signal by the ADC makes the distribution asymmetric, as presented in figure A.14(b) in which the convert value is 7. Therefore the chosen convert value (=0) is correct because the η distribution remains symmetric with respect to zero (figure A.14(a)); moreover this choice is in agreement with the previous study of the pull of the strip adjacent to the one with the maximum. Also the other silicon detectors behave in the same way; the final convert value used in the following tests has been set to 0.

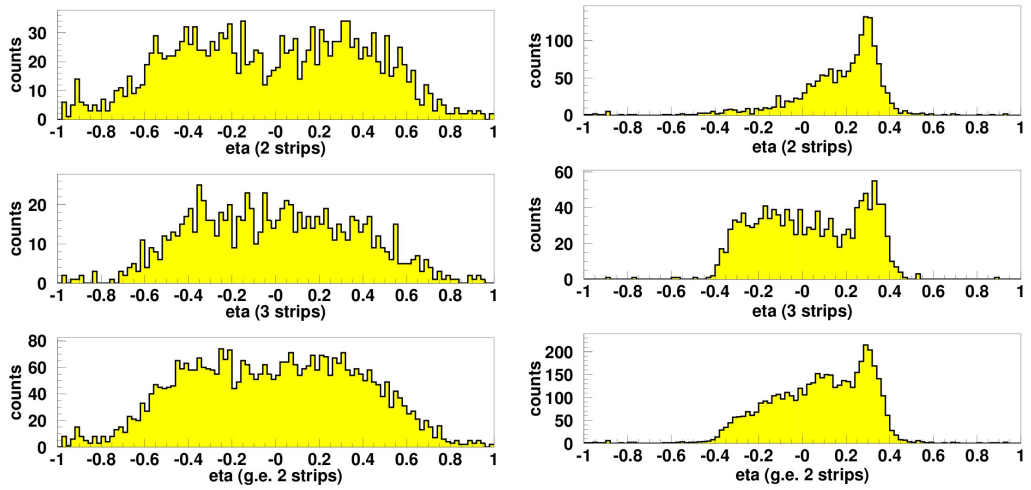

(a) (b)

Figure A.14: Eta distributions: a) for the convert value equal to 0 it is symmetric while b) for the convert equal to 7 it is asymmetric.

A.2.2 Cosmic ray tests

The last tests on the silicon microstrip detectors have been performed with the cosmic rays. As explained in the previous sections two plastic scintillator counters have been placed above and below the detector in order to generate a coincidence signal to start the acquisition.
The acquisition has been performed with the hold and convert values chosen in the previous tests (7 and 0 respectively). Figure A.15 shows an example of the pull distribution obtained for the strip with the maximum signal in the event. The threshold (red line) is set considering the pull and excluding the regions corresponding to the noise (high peak near 0).
The cluster pulse height (figure A.16(a)) and the cluster SNR distributions (figure A.16(b)) have been analyzed: in both cases the shape is a Landau one with the peak respectively at $\sim$260 ADC and $\sim$35.
The number of strips per cluster is presented in figure A.17(a): typically 2 strips have collected the charge generated by a particle in each event. Furthermore the distribution of the number of clusters per event has been considered: almost 30% of them is a single cluster event[3] as presented in figure A.17(b).

The η function has been evaluated in order to understand the charge sharing. Fig-

[3]The percentage of the remaining events is represented by the particles that have crossed the scintillators (generating a coincidence signal) but not the silicon detector.

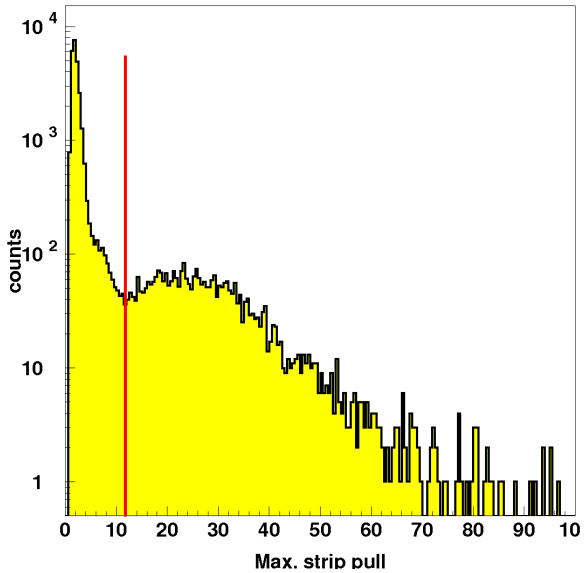

Figure A.15: Pull distribution for the strip with the maximum signal in the event.

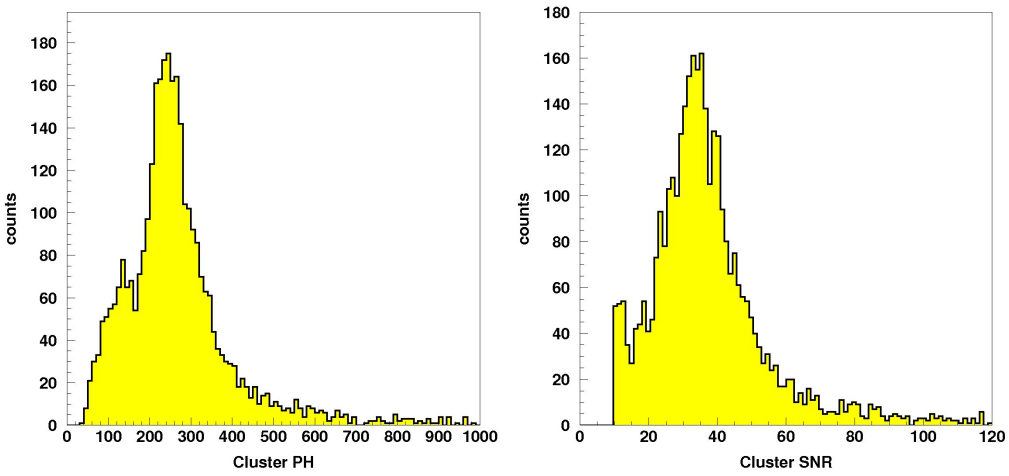

(a) (b)

Figure A.16: The cluster a) pulse height and b) SNR distributions of one silicon detector under test obtained with the cosmic rays.

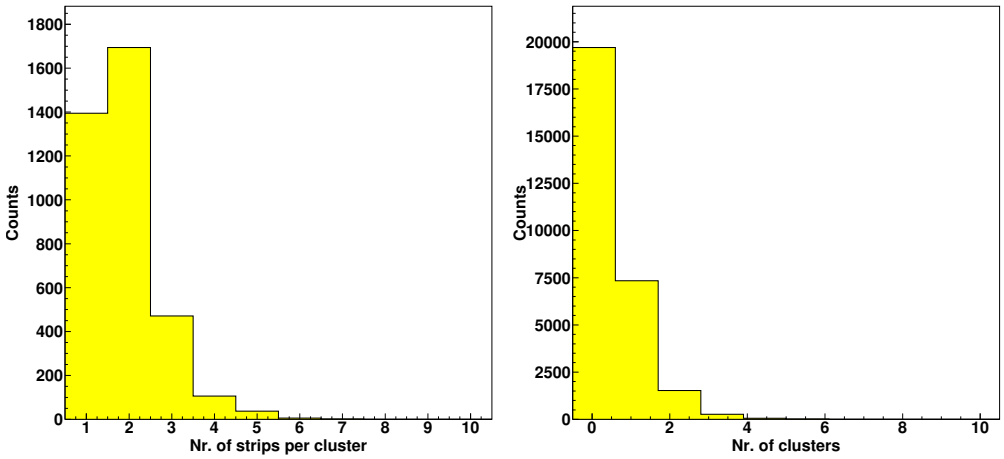

(a) (b)

Figure A.17: The distribution of a) the number of strips per cluster and b) the number of clusters for the cosmic rays tests.

ure A.18 presents the η distribution calculated for a cluster composed of 2, 3 or $\geq$2 strips. In all these cases the distributions are symmetric therefore the charge is equally shared among the strips and the chosen convert value is correct.

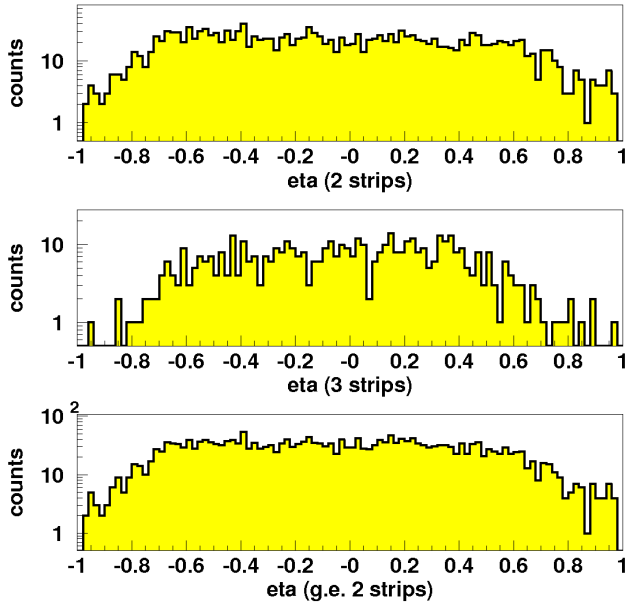

Figure A.18: Eta distribution with the cosmic rays for a cluster composed of 2 (top), 3 (middle) or $\geq$2 strips (bottom).

List of acronyms

AC	Alternating Current
ADC	Analog to Digital Converter
AGILE	Astrorivelatore Gamma a Immagini LEggero
ALEPH	Apparatus for LEP PHysics
ALICE	A Large Ion Collider Experiment
ASIC	Application Specific Integrated Circuit
BNL	Brookhaven National Laboratory
CAEN	Costruzioni Apparecchiature Elettroniche Nucleari
CERN	European Organization for Nuclear Research
CMOS	Complementary Metal Oxide Semiconductor
CMS	Compact Muon Solenoid
CNGS	CERN Neutrinos to Gran Sasso
COG	Center Of Gravity
COMPASS	COmmon Muon and Proton Apparatus for Structure and Spectroscopy
CSEM	Centre Suisse d'Electronique et Microtechnique
DAC	Digital to Analog Converter
DAQ	Data AcQuisition
DC	Direct Current
DELPHI	DEtector with Lepton, Photon and Hadron Identification
DMA	Direct Memory Access
ECAL	Electromagnetic CALorimeter
ENC	Equivalent Noise Charge
FPGA	Field Programmable Gate Array
HEP	High Energy Physics
HLT	High Level Trigger
IHEP	Institute for High Energy Physics
ISR	Intersecting Storage Ring
LEP	Large Electron Positron
LHC	Large Hadron Collider
LHCb	Large Hadron Collider beauty

LSI	Large Scale Integration
LVDS	Low-Voltage Differential Signaling
MCS	Multiple Coulomb Scattering
MIP	Minimum Ionizing Particle
MOS	Metal Oxide Semiconductor
MPV	Most Probable Value
MV	Mean Value
MVD	Micro Vertex Detector
MWPC	Multi-Wire Proportional Chamber
NIM	Nuclear Instrumentation Module
PCB	Printed Circuit Board
PEP	Positron Electron Project
PMT	PhotoMultiplier Tube
PS	Proton Synchrotron
RAM	Random Access Memory
RHIC	Relativistic Heavy Ion Collider
SFM	Split Field Magnet
SLAC	Stanford Linear Accelerator Center
SM	Standard Model
SPS	Super Proton Synchrotron
TPC	Time Projection Chamber
TTL	Transistor-Transistor Logic
VLSI	Very Large Scale Integration
VME	Versa Module Eurocard

List of Figures

List of Tables

Bibliography

[1] F. Close *et al. The Particle Odyssey*. Oxford University Press, 2002. ISBN:0-19-860943-4.

[2] W. E. Burcham and M. Jobes. *Nuclear and particle physics*. Prentice Hall, 1995. ISBN:0-582-45088-8.

[3] C. Grupen and I. Buvat. *Handbook of particle detection and imaging*. Springer, 2012. ISBN:978-3-642-13270-4.

[4] F. Hartmann. *Evolution of silicon sensor technology in particle physics*. Springer, 2009. ISBN:978-3-540-25094-4.

[5] CDF Collaboration. *The CDF detector: an overview*. Nucl. Instr. and Meth. in Phys. Res. A 271: 387–403, 1988.

[6] R. L. Gluckstern. *Uncertainties in track momentum and direction, due to multiple scattering and measurement errors*. Nucl. Instr. and Meth. in Phys. Res. 24: 381–389, 1963.

[7] CMS Collaboration. *Detector Performance and Software*. CMS Physics Technical Design Report, Volume I CERN-LHCC-2006-001, 2006.

[8] E. Segré. *Nuclei and Particles: An Introduction to Nuclear and Subnuclear Physics*. W. A. Benjamin, New York: 65–966, 1964.

[9] P. Renton. *Electroweak Interactions: an Introduction to the Physics of Quarks and Leptons*. Cambridge University Press, 1990. ISBN:0-521-26603-3.

[10] K. Safarik *et al. Particle Tracking*. AIP Conf. Proc. 631: 377–394, 2008.

[11] F. Hartmann. *Silicon tracking detectors in high-energy physics*. Nucl. Instr. and Meth. in Phys. Res. A 666: 25–46, 2012.

[12] A. Michelini. *OPAL detector performance*. Philos. Trans. R. Soc. Lond. A 336: 237–246, 1991.

[13] L. Lyons and D. H. Saxon. *Measurement of short-lived particles in high-energy physics*. Rep. Prog. Phys. 52: 1015–1082, 1989.

[14] G. Branco, L. Lavoura and J. Silva. *CP violation*. Clarendon Press, Oxford, 1999. ISBN:978-0-19-850399-6.

[15] PDG Collaboration. *Particle Data Group*. 2008. URL http://pdg.lbl.gov.

[16] G. J. Barker. *b-Quark Physics with the LEP collider*. Springer, 2010. ISBN:978-3-642-05279-8.

[17] J. J. Thomson. *Cathode rays*. Philosophical Magazine 44: 293–316.

[18] C. D. Anderson. *The positive electron*. Phys. Rev. 43: 491–494, 1933.

[19] I. Tserruya. *The DELPHI Silicon Tracker in the global pattern recognition*. AIP Conf. Proc. 1422: 166–177, 2011.

[20] S. M. Bilenky and J. Hosek. *Glashow Weinberg Salam theory of electroweak interactions and the neutral currents*. Phys. Rep. 90:73–157, 1999.

[21] F. J. Hasert *et al. Observation of neutrino-like interactions without muon or electron in the Gargamelle neutrino experiment*. Phys. Lett. B 46: 138–140, 1973.

[22] R. P. Shutt. *Bubble and Spark Chambers*. Academic Press, 1967.

[23] G. Charpak *et al. The use of multiwire proportional counters to select and localize charged particles*. Nucl. Instr. and Meth. in Phys. Res. 62: 262–268, 1968.

[24] F. Sauli. *Principles of Operation of Multiwire Proportional and Drift Chambers*. CERN-77-09, 1977.

[25] P. Schilly *et al. Construction and performance of large multiwire proportional chambers*. Nucl. Instr. and Meth. in Phys. Res. 91: 221–230, 1971.

[26] T. Bressani *et al. Track localization by means of a drift chamber*. Proc. of the Int. Seminar on Filmless Spark and Streamer Chambers, 1969.

[27] G. Marel *et al. Large planar drift chambers*. Nucl. Instr. and Meth. in Phys. Res. 141: 43–56, 1977.

[28] J. N. Marx and D. R. Nygren. *The time projection chamber*. Phys. Today 31: 46–53.

[29] A. R. Clark *et al. Proposal for a PEP facility based on the time projection chamber*. PEP- PROPOSAL-004, 1976.

[30] H. Wieman *et al. Star TPC at RHIC*. IEEE Transactions on Nuclear Science 44: 671–678, 1997.

[31] ALICE Collaboration. *A Large Ion Collider Experiment, ALICE TPC*. Technical Design Report, CERN/LHCC 2000-001, 2000. ISBN:92-9083-155-3.

[32] M. Perelstein. *Introduction to Collider Physics*. arXiv:1002.0274v2, 2010.

[33] J. Kemmer. *Fabrication of a low-noise silicon radiation detector by the planar process*. Nucl. Instr. and Meth. in Phys. Res. 169: 499–502, 1980.

[34] P. Aarnio *et al. The DELPHI detector at LEP*. Nucl. Instr. and Meth. in Phys. Res. A 303: 233–276, 1991.

[35] The DELPHI Silicon Tracker Group. *The DELPHI Silicon Tracker at LEP2*. Nucl. Instr. and Meth. in Phys. Res. A 412: 304–328, 1998.

[36] The DELPHI Silicon Tracker Group. *Performance of the DELPHI detector*. Nucl. Instr. and Meth. in Phys. Res. A 378: 57–100, 1996.

[37] A. Straessner. *Electroweak Physics at LEP and LHC*. Springer, 2010. ISBN:978-3-642-05168-5.

[38] G. Dissertori. *LHC Detectors and Early Physics*. arXiv:1003.2222, 2010.

[39] CMS Collaboration. *Physics Performance*. CMS Physics Technical Design Report, Volume II CERN/LHCC 2006-021, 2006.

[40] F. Hartmann *et al. Construction of the CMS tracker*. Nucl. Instr. and Meth. in Phys. Res. A 572: 73–76, 2007.

[41] K. G. McKay. *Electron-hole production in germanium by alpha-particles*. Phys. Rev. 84: 829–832, 1951.

[42] R. Bailey *et al. A silicon strip detector telescope for the measurement of production and decay of charmed particles*. Nucl. Instr. and Meth. in Phys. Res. 226: 56–58, 1984.

[43] A. Schwarz. *Construction operation and first results for the ALEPH double sided silicon strip vertex detector*. Proceedings of the 25th International Conference on High Energy Physics: 1345–1347, 1990.

[44] J. L. Agram *et al.* *The silicon sensors for the Compact Muon Solenoid tracker - design and qualification procedure*. Nucl. Instr. and Meth. in Phys. Res. A 517: 77–93, 2004.

[45] S. M. Sze. *Physics of Semiconductor Devices*. John Wiley and Sons, 1985. ISBN:0-471-87424-8.

[46] C. J. S. Damerell. *Vertex detector: the state of the art and future prospects*. Technical Report, RAL-P-95-008, 1995. ISSN:1361-4762.

[47] A. Peisert. *Silicon Microstrip Detector, Instrumentation in High-Energy Physics*. World Scientific, 1992.

[48] L. Pavesi and D. J. Lockwood. *Silicon Photonics*. Springer, 2004. ISBN:3-540-21022-9.

[49] C. Grupen and B. Shwartz. *Particle Detectors*. Cambridge University Press, 2008. ISBN:978-0-521-84006-4.

[50] W. R. Leo. *Techniques for Nuclear and Particle Physics Experiments: A How-To Approach*. Springer-Verlag, 1994. ISBN:0-387-57280-5.

[51] P. Weilhammer. *Overview: silicon vertex detectors and trackers*. Nucl. Instr. and Meth. in Phys. Res. A 453: 60–70, 2000.

[52] H. Dijkstra. *Overview of silicon detectors*. Nucl. Instr. and Meth. in Phys. Res. A 478: 37–45, 2002.

[53] L. Bellucci. *Silicon detector developments for CMS*. Nucl. Instr. and Meth. in Phys. Res. A 462: 243–248, 2001.

[54] C. L. Gomez. *Study of silicon microstrip detector properties for the LHCb silicon tracker*. Master Thesis, Santiago de Compostela University, 2006. CERN-THESIS-2006-017.

[55] H. Bichsel. *Straggling in thin silicon detectors*. Review of Modern Physics 60: 663–699, 1988.

[56] P. Weilhammer. *Double-sided Si strip sensors for LEP vertex detectors*. Nucl. Instr. and Meth. in Phys. Res. A 342: 1–15, 1994.

[57] L. Borrello *et al.* *Sensor design for the CMS silicon strip tracker*. CMS-NOTE-2003-020, 2003.

[58] R. Turchetta. *Spatial resolution of silicon microstrip detectors*. Nucl. Instr. and Meth. in Phys. Res. A 335: 44–58, 1993.

[59] P. Collins. *Silicon detectors lectures*. http://lhcb-doc.web.cern.ch/lhcb-doc/presentations/lectures/CollinsItacuruca03-2nd.pdf.

[60] G. Landi. *Properties of the centre of gravity as an algorithm for position measurements: two-dimensional geometry*. Nucl. Instr. and Meth. in Phys. Res. A 497: 511–534, 2003.

[61] U. Kötz *et al.* *Silicon strip detectors with capacitive charge division*. Nucl. Instr. and Meth. in Phys. Res. A 235: 481–487, 1985.

[62] M. Prest *et al.* *The AGILE silicon tracker: an innovative γ-ray instrument for space*. Nucl. Instr. and Meth. in Phys. Res. A 342: 1–15, 1994.

[63] C. Bozzi. *Signal-to-noise evaluations for the CMS silicon microstrip detectors*. CMS NOTE 1997/026, 1997.

[64] Z. Y. Chang and W. M. C. Sansen. *Low-noise wide-band amplifiers in bipolar and CMOS technologies*. Kluwer Academic Publishers, London, 1990.

[65] J. T. Walker *et al.* *Development of high density readout for silicon strip detectors*. Nucl. Instr. and Meth. in Phys. Res. 226: 200–203, 1984.

[66] S. Hasan. *Experimental techniques for deflection and radiation studies with bent crystals* . PhD Thesis, Università dell'Insubria, 2011. http://insulab.dfm.uninsubria.it/images/download_files/thesis_hasan_PhD.pdf.

[67] D. Bolognini. *Study of channeling phenomena in bent crystals: the new frontier*. Master Thesis, Università dell'Insubria, 2008. http://insulab.dfm.uninsubria.it/images/download_files/thesis_bolognini_master.pdf.

[68] S. Hasan. *Bent silicon crystals for the LHC collimation: studies with an ultrarelativistic proton beam*. Master Thesis, Università dell'Insubria, 2007. http://insulab.dfm.uninsubria.it/images/download_files/thesis_hasan_master.pdf.

[69] J. Stark. *Phys. Zs.* 13: 973–977, 1912.

[70] J. Lindhard. *Motion of swift charged particles, as influenced by strings of atoms in crystals*. Phys. Lett. 12: 126–128, 1964.

[71] E. Tsyganov. *Some aspects of the mechanism of a charge particle penetration through a monocrystal*. Fermilab preprint TM-682, 1976.

[72] A. F. Elishev *et al. Steering of charged particle trajectories by a bent crystal*. Phys. Lett. B 88: 387–391, 1979.

[73] A. M. Taratin and S. A. Vorobiev. *Deflection of high-energy charged particles in quasi-channeling states in bent crystals*. Nucl. Instr. and Meth. in Phys. Res. B 26: 512–521, 1987.

[74] V. M. Biryukov *et al.* Crystal channeling and its application at high-energy accelerators. Springer, 1997.

[75] D. Bolognini *et al. The high performance microstrip silicon detector tracking system for an innovative crystal based collimation experiment*. Nucl. Instr. and Meth. in Phys. Res. A 617: 439–443, 2010.

[76] L. Celano *et al. A high resolution beam telescope built with double sided silicon strip detectors*. Nucl. Instr. and Meth. in Phys. Res. A 381: 49–56, 1996.

[77] *The VA2 Specifications*. http://ideas.no.

[78] D. Bolognini. *The MICE Electron Muon Ranger: a fundamental step towards a neutrino factory*. PhD Thesis, Università dell'Insubria, 2012. http://insulab.dfm.uninsubria.it/images/download_files/bolognini_thesis_phd.pdf.

[79] MICE Collaboration. *An International Muon Ionization Cooling Experiment (MICE)*. Proposal to the Rutherford Appleton Laboratory, 2003. http://mice.iit.edu/mnp/MICE0021.pdf.

[80] M. Bari *et al. Results from the BaBar Silicon Vertex Tracker test beam*. BaBar Note 278, 1996.

[81] *The VA1TA Datasheet version 0.9*. http://ideas.no.

[82] M. Prest. *Silicon Specifications for the detector of the FRONTRAD experiment*. Internal communication, 2001.